BRNO UNIVERSITY OF TECHNOLOGY
VYSOKÉ UČENÍ TECHNICKÉ V BRNĚ

FACULTY OF CHEMISTRY
FAKULTA CHEMICKÁ

INSTITUTE OF CHEMISTRY AND TECHNOLOGY OF ENVIRONMENTAL PROTECTION
ÚSTAV CHEMIE A TECHNOLOGIE OCHRANY ŽIVOTNÍHO PROSTŘEDÍ

SYNTHESIS AND STUDY OF NANO-STRUCTURED PEROVSKITES FOR APPLICATIONS IN ORGANIC ELECTRONICS
SYNTÉZA A STUDIUM NANO-STRUKTUROVANÝCH PEROVSKITŮ PRO APLIKACE V ORGANICKÉ ELEKTRONICE

DOCTORAL THESIS
DIZERTAČNÍ PRÁCE

AUTHOR Ing. Anna Jančík Procházková
AUTOR PRÁCE

SUPERVISOR doc. Ing. Jozef Krajčovič, Ph.D.
ŠKOLITEL

BRNO 2020

This page is intentionally left blank.

Specification Doctoral Thesis

Department:	Institute of Chemistry and Technology of Environmental Protection	Academic year:	2019/20
Student:	**Ing. Anna Jančík Procházková**		
Study programme:	Chemistry, Technology and Properties of Materials		
Study branch:	Chemistry, Technology and Properties of Materials		
Head of thesis:	**doc. Ing. Jozef Krajčovič, Ph.D.**		

Title of Doctoral Thesis:

Synthesis and Study of Nano–Structured Perovskites for Applications in Organic Electronics

Doctoral Thesis:

1)Synthesis of lead halide perovskite nanoparticles and its optimization. The basic optical properties of the resulting colloidal solutions and thin films are to be studied.

2)Modify the surface of perovskite nanoparticles by proteinogenic amino acids possessing primary amine or guanidyl group in their side chains.

3)According to the results, find nature–inspired capping agents suitable for the preparation of perovskite nanoparticles, for example peptides. The aim is to preserve the functionality of the nature–inspired molecules, such as sensing and self–assembly abilities, alongside the unique optoelectrical properties of perovskite materials.

Deadline for Doctoral Thesis delivery: 31.7.2020:

Ing. Anna Jančík Procházková Student	doc. Ing. Jozef Krajčovič, Ph.D. Head of thesis	doc. Ing. Jiří Kučerík, Ph.D. Head of department

prof. Ing. Martin Weiter, Ph.D.
Dean

In Brno dated 1.9.2019

This page is intentionally left blank.

Abstract

Diversity and unique properties, such as exceptionally high photoluminescence quantum yields (PLQYs), predetermine metal halide perovskite nanoparticles (PNP) to be applied in optoelectronic and photonic devices. In this work, nature-inspired capping agents were employed not only for the PNP stabilization but also for modifying their surface to broaden the functionality of the resulting material. In the very beginning, a ligand-assisted precipitation technique was optimized for the preparation of the PNP. Here, adamantane-1-amine (AdNH$_2$) alongside hexanoic acid (HeA) were chosen as capping agents for nanoparticles stabilization and passivation. It was demonstrated that the choice of the solvent system and the precipitation temperature have a crucial effect on the resulting optical properties of the colloidal solutions. Simultaneously, the influence of concentration of precursor chemicals on the resulting morphology and optical properties was investigated. Also, different carboxylic acids were tested as capping agents among AdNH$_2$ and the colloidal stability of the resulting colloidal solutions was evaluated.

To demonstrate the diversity of the ligand-assisted precipitation technique of PNP preparation, L-lysine and L-arginine were employed initially for the surface passivation. As a result, colloidal solutions with emission within a narrow bandwidth of the visible spectrum and remarkable photoluminescence quantum yield (PLQY) close to 100% were obtained. Blocking α-amino group of L-lysine by *tert*-butoxycarbonyl group suggested preferential binding of the side chain of L-lysine to the perovskite core. Furthermore, defined amounts of water were added into the precursor solutions which caused shifts of emission spectra due to quantum confinement effects. Water molecules were assumed to form highly mobile species leading to the enhancement of controlling the perovskite lattice growth.

Merging perovskite nanomaterials with peptides are expected to pave a way to the new class of materials possessing exceptional optoelectronic properties alongside self-assembly and sensing abilities. As a proof-of-concept, a cyclic(RGDFK) pentapeptide was used for PNP stabilization. However, peptides are known for their sensitivity to their environment. Therefore, peptide nucleic acid (PNA) was used for PNP stabilization as a robust artificial analogue for deoxyribonucleic acid (DNA). Here, optical properties of thymine-based PNA monomer and trimer stabilized PNP were studied. Additionally, the sensing ability of the PNA ligand for adenine moiety was demonstrated by photoluminescence quenching via charge transfer. We envision that combining the unique tailored structure of PNA and the prospective optical features of PNP could expand the applications especially in the field of optical sensing devices.

Abstrakt

Nanočástice perovskitů halogenidů kovů vykazují unikátní vlastnosti, především výjimečně vysoké hodnoty kvantových výtěžků fluorescence, které předurčují tyto materiály pro aplikace v optoelektronických a fotonických zařízeních. Tato práce popisuje přípravu nanočástic perovskitů halogenidů kovů pomocí stabilizačních činidel inspirovaných přírodou. Stabilizační činidla zde slouží nejen ke stabilizaci, ale i k modifikaci povrchu nanočástic za účelem zvýšení funkčnosti výsledných nanostruktur. Úvod práce popisuje optimalizaci přípravy nanočástic precipitační technikou za použití stabilizačních činidel; jako stabilizační činidlo byl zvolen adamantan-1-amin spolu s hexanovou kyselinou. Bylo prokázáno, že klíčový vliv na optické vlastnosti výsledných koloidních roztoků má volba rozpouštědel a teploty při precipitaci. Mimo jiné byl zkoumán vliv koncentrace prekurzorů na výslednou morfologii a optické vlastnosti nanočástic a jejich koloidních roztoků. V neposlední řadě byly nanočástice stabilizovány adamantan-1-aminem spolu s různými karboxylovými kyselinami a byly studovány optické vlastnosti a koloidní stabilita výsledných koloidních roztoků.

V dalším kroku byly nanočástice perovskitů stabilizovány pomocí proetogenních aminokyselin L-lysinu and L-argininu. Takto stabilizované nanočástice vykazovaly úzká emisní spektra ve viditelné oblasti a kvantové výtěžky fluorescence dosahující hodnot téměř 100 %. Stabilizace nanočástic prostřednictvím postranních skupin aminokyselin byla prokázána navázáním chránící *terc*-butoxykarbonylové skupiny na α-amino skupinu. Nanočástice stabilizované modifikovaným lysinem v průběhu jejich přípravy vykazovaly závislost optických vlastností na přítomnosti vody. Předpokládá se, že molekuly vody jsou schopné kontrolovat růst krystalové mřížky po navázání na prekurzory perovskitů a ovlivňovat tak výslednou velikost nanočástic, což vede k projevení kvantových jevů.

Spojení nanočástic perovskitů s peptidy představuje nový typ materiálů kombinujících výjimečné optické vlastnosti se samoorganizačními a senzorickými vlastnostmi. Tento koncept byl představen přípravou nanočástic perovskitů stabilizovaných cyklo(RGDFK) pentapeptidem. Vzhledem k citlivosti peptidů na jejich byly nanočástice stabilizovány peptidovými nukleovými kyselinami, robustními analogy nukleových kyselin. Ke stabilizaci nanočástic byl připraven monomer a trimer peptidové nukleové kyseliny obsahující thymin jako dusíkatou bázi. Thymin byl na povrchu nanočástic dostupný k interakci s adeninem přes vodíkové můstky umožňující přenos náboje. Kombinace peptidových nukleových kyselin a perovskitů s unikátními optickými vlastnostmi otevírá aplikační možnosti zejména v oblasti optických senzorů.

Key words

Metal halide perovskite, perovskite nanocrystals, nanoparticles, semiconductors, ligands, capping agents, biomolecules, amino acids, peptides, peptide nucleic acid, optoelectrical properties, optoelectronics.

Klíčová slova

Perovskity, nanokrystaly perovskitů, nanočástice, polovodiče, ligandy, stabilizační činidla, biomolekuly, aminokyseliny, peptidy, peptidové nukleové kyseliny, optoelektrické vlastnosti, optoelektronika.

Prohlášení

Prohlašuji, že jsem dizertační práci vypracovala samostatně a že všechny použité literární zdroje jsem citovala správně a úplně. Dizertační práce je z hlediska obsahu majetkem Fakulty chemické VUT v Brně a může být využita ke komerčním účelům jen se souhlasem vedoucího dizertační práce a děkana FCH VUT.

……………………………..
podpis studenta

8

Acknowledgement

First of all, I would like to thank to my supervisor doc. Ing. Jozef Krajčovič, Ph.D. for giving me the opportunity to be a part of his team and for his support during my PhD studies. I would also like to acknowledge Prof. Ing. Martin Weiter, Ph.D. and the whole team of the Laboratory of Organic Electronics and Photonics in the Faculty of Chemistry, Brno University of Technology for their help and a nice working environment.

Furthermore, I would like to sincerely thank Dr. Alexander Kovalenko. Thank you for your supportive guidance, your optimism, and for your encouragement, which led me through each stage of my studies. A big thanks go to my dear friend Dr. Yolanda Salinas, for all the fruitful discussions during the coffee breaks and for sharing her scientific and non-scientific experience. Here, I would also love to thank Dr. Cigdem Yumusak for all the supportive discussions. Without these great people, my studies would be almost impossible.

A very warm acknowledgement goes to Univ. Prof. Dr. Niyazi Serdar Sariciftci. Thank you for giving me the opportunity to spend an amazing and unforgettable period of my Ph.D. studies in Linz Institute for Organic Solar cells (LIOS) in Johannes Kepler University Linz. Thank you for inspiring me and for fully supporting me both in scientific and non-scientific ways. Big thanks go to Assoc. Prof. DI Dr. Markus Clark Scharber for his help with optical spectroscopy techniques. Thank you for all the help, fruitful discussions, and patience with my samples. Here, I would also like to acknowledge every LIOS member. Thank you for your incredible team spirit, motivation, and especially for a nice working environment.

My extended thanks go to Univ. Prof. Dr. Oliver Brüggemann. Thank you for supporting my stay and kindly providing me access to your laboratories. I would like to thank the whole team of the Institute of Polymer Chemistry in Johannes Kepler University Linz for their support and all the nice time we spent together.

I would like to thank all the internal and external collaboration partners for sharing their precious experience with me. I am extremely grateful for your support and expertise which helped me to shape this thesis.

Finally, I would like to thank my family: my dear parents Ivana and Rostislav, my darling siblings Majka, Honzík and Bety and my beloved husband Janík. Thank you for believing in me and for supporting every decision I made. I'm grateful to have such great people standing always beside me.

Content

1 Aim of the dissertation thesis

The aim of the doctoral dissertation is the synthesis and characterization of lead halide perovskite nanoparticles for a large variety of electrical and optical applications. The first goal is to find a suitable synthetic pathway for the perovskite nanoparticles preparation and to evaluate all parameters influencing the resulting morphology and optical properties of the hybrid materials.

In the next steps, nanoparticles stabilized by amino acids possessing primary amine or guanidyl group alongside the α-amino and carboxylic groups are to be prepared. The primary amine or guanidyl group of the amino acid is intended to passivate the surface of the nanoparticles, whereas, the α-amino and carboxylic acid groups are supposed to decorate the surface and to be available for further interactions. Simultaneously, optical and electrical characterization is planned to be performed. Evaluation of the optical and electrical band gap, luminescence quantum yields absorption and emission spectra will help to reveal the potential applications.

Finally, the possibility of employing more complex nature-inspired capping agents for the nanoparticles' formation will be tested to control the growth of the nanoparticles. For example, peptides seem to be very attractive because of their sensing abilities, self-assembly properties and affinity to certain surfaces. The main goal is to merge perovskite materials with nature-inspired molecules to preserve the unique properties of both materials which would broaden the applicability of the resulting hybrid materials.

2 Introduction

The clear vision of introducing nanomaterials into the real life was presented by the physicist Richard Feynman during his famous talk *"There´s Plenty of Room at the Bottom"* in 1959 [1]. He predicted the future of nanotechnology and suggested physical principles and approaches which could help for example with miniaturization of electronics even to an atomic level. Years later, Feynman´s ideas were followed by D. M. Eigler and E. K. Schweizer [2] from IBM´s Almaden Research Center, who succeeded in organizing single xenon atoms into the logo of the IBM company by the use of scanning tunnelling microscope (STM) in 1989. Since then, a real boom of nanotechnology has started.

Nanomaterials can be defined as materials with reduced, at least one dimension, to the nano-scale (usually in the range 1–100 nm). The use of nano-scaled materials leads primarily to the miniaturization in technology and industry, e.g. miniaturization of batteries, quantum dot light emitting diodes (QDLED) screens and smartphones. Higher surface-to-volume ratio of nanomaterials increases also the efficiency in environmental protection applications (i.e. water purification and nanocapsules for pesticide delivery), catalysis in catalytic CO_2 reduction and in harvesting energy from renewable sources (solar cells fabrication). Nanotechnology has already been employed in food and cosmetics and of course in medicine. The latter actually represents one of the largest fields of nanotechnology where nanomaterials are applied in diagnostics, imaging and detection of diseases (as nanobiosensors, drug delivery systems, scaffolds for tissue regeneration, among others) [3] and [4].

Metal halide hybrid and inorganic perovskites are materials related to calcium titanium oxide mineral with the chemical formula $CaTiO_3$. It was firstly described by Gustav Rose in 1893 and it is named after Russian mineralogist Lev Perovski. Nowadays, perovskite materials are usually discussed with regards to photovoltaic applications because of the high efficiency of perovskite-based solar cells, up to 25.2 % [5]. Nevertheless, perovskites can be also used for the fabrication of light emitting diodes (LED), lasers, photodetectors, etc. [6].

Perovskites are known for their ability to crystallize at a large variety of different surfaces/interfaces, including few-centimeters large single crystals, without a nucleation or also to form colloidal nanocrystals at room temperature. Prominently, benign structural defects are highly abundant in these perovskite compounds, which play an important role with respect to optical and electronic properties. Therefore, perovskites have proven to have a bright future in a form of semiconducting nanoparticles, where the physical properties can be tuned not only

by the chemical stoichiometry of the compounds but also by controlling the size of the particles at the dimensional scale where quantum confinement effects take place. Perovskite nanoparticles (PNP) have already shown their applicability in optoelectronic devices such as organic light emitting diodes (OLEDs) [7]–[8], photodetectors [9] and lasers [10].

In general, traditional bottom-up synthesis of colloidal nanoparticles usually involves stabilization by ligands and capping agents. In this regard, ligand-engineering is an important factor to fine tune the nanoparticles processing techniques. One of the most efficient ways of the ligand engineering is the use of the multifunctional ligands which do not only interrupt crystallization processes forming the nanoparticles, but also provide functional surface groups.

One of the most promising materials that combine the ability to interrupt the crystallization of perovskite nanoparticles and bringing an additional functionality could be amino acids and their derivatives, such as oligo- and polypeptides, nucleic acids or their artificial analogues peptide nucleic acids. Amino acids are compounds of biological origin, relatively cheap and abundant. Moreover, amino acids can serve as a building block for oligo- and polypeptides while the functionality of the material is widespread due to uncountable combinations [11]–[13]. Hence, by combining the unique properties of perovskite nanoparticles, such as high absorption coefficient, high luminescent yields and charge carrier transport, together with the properties of amino acids/peptides/peptide nucleic acids such as affinity to the desired surfaces, self-assembly and sensing abilities (molecular switches), the resulting materials can be extremely attractive from the application point of view.

3 Nanostructured materials as semiconductors for organic electronics

Considering electrical conductivity, materials can be classified into three main groups – metals, semiconductors and insulators. The main differences between these materials can be derived from their electronic structure. The electronic structure typically consists of valence band (VB) and conduction band (CB), the energy difference between the valence and the conduction band is noted as band gap energy (E_g). The valence band is formed of the overlap of the occupied energetic levels of the individual structural units, similarly, the conduction band is formed of the overlap of the unoccupied energetic levels, both the valence and the conduction bands are usually continuous, schematically see in Figure 1. The latest occupied level is noted as Fermi level (E_F), statistically, it is an energetic level which is occupied with 50% probability. In case the valence band is not fully occupied by electrons or in case the valence band is overlapping with the conduction band, electrons can move freely in a form of delocalized electrons which form electron clouds and therefore, these materials exhibit excellent conductivity. Such materials are called metals. If the valence band is fully occupied, electrons can be promoted to the conduction band when energy equal or higher than band gap energy is provided (for example by light excitation). The promotion of the electron (e^-) to the conduction band causes a creation of a hole (h^+) in the valence band. If the band gap energy is too big for promoting the electron (typically > 3 eV) without causing any damage to the structure, then the material is considered as an insulator [14]–[16].
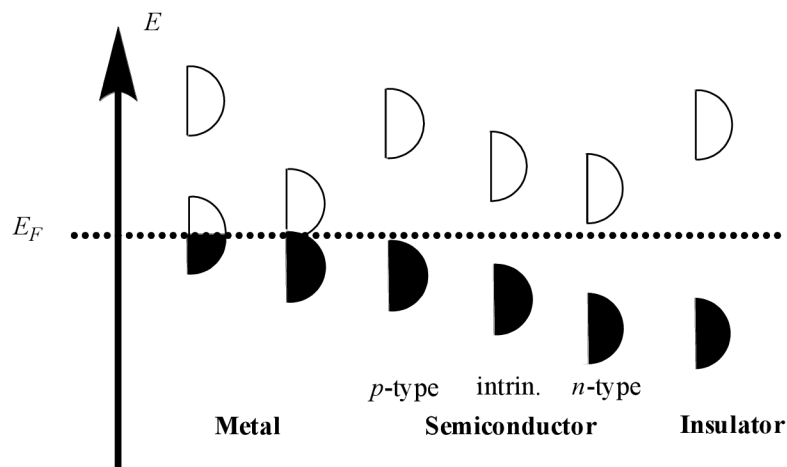

Figure 1: Electronic structure of metals, semiconductors and insulators, the upper are conduction bands and the lower are valence bands, modified from [14]–[16]

In intrinsic semiconductors (for example in silicon or germanium) the band gap energy can be exceeded even by thermal energy. The conductivity of semiconductors can be increased even a few orders of magnitude by doping, which means incorporating different species into the semiconductor crystal lattice. Electron-rich dopants (for example arsenic in silicon) act as electron donors. The energy level of the donors is close to the conductive band of the semiconductors, thus the electron can be promoted from the donor to the conduction band and act as a charge carrier; these types of semiconductors are called as n-type.

On the other hand, electron-poor dopants (for example boron incorporated in silicon), whose energy level is close to the valence band, accept electrons from the valence band of the semiconductor where a hole is formed. Here, the holes act as charge carriers and this type of semiconductor is called p-type [14].

It has been mentioned above that by the promotion of an electron from the valence band to the conduction band, two quasi-particles formation is supposed to occur. Both the electron and the hole can be described by the charge (e^-) and (h^+), by spin ($s = 1/2$ in both cases) and by effective mass m_e* and m_h*, respectively. The effective mass helps to predict the mobility of charge carriers, if the effective mass is larger than the free electron mass, then the interaction with the crystal lattice causes decreased mobility and vice versa.

The electron-hole pair forms an exciton. It should be noted, that the formation of the exciton requires a minimum amount of energy E given by the following equation:

$$E = E_g + E_{e,kin} + E_{h,kin},$$ (1)

where $E_{e,kin}$ and $E_{h,kin}$ represent kinetic energies of electron and hole, respectively. The required energy E is higher than the band gap energy because the Coulomb potential caused by oppositely charged species must be exceeded.

For the characterization of exciton, Bohr radius a_0 is considered, it describes the probable distance between the electron and hole. The Bohr radius a_0 can be calculated as

$$a_0 = \frac{\hbar^2 \varepsilon}{e^2} \left(\frac{1}{m_e^*} + \frac{1}{m_h^*} \right),$$ (2)

where e is the electron charge, ε is the dielectric constant of the semiconductor and $\hbar$ is reduced Planck constant. The Bohr radius is a material constant and its value lies approximately in the range 2–50 nm. The Bohr radius correlates also with the band gap energy; in general, wider band gaps in semiconductors exhibit smaller a_0 [17].

Alongside the demands for reducing the size of electronics, lowering dimensionality of semiconductor materials up to nano-scale is necessary. The general feature of nanomaterials is their high surface-to-volume ratio in comparison with bulk materials. The properties of resulting nanomaterials are then strongly surface dependent. Lowering the size of nanocrystal up to nano-scale, the electronic properties of the semiconductor exhibit different behaviour than in bulk infinite crystals because of the employment of quantum confinement effects. To evaluate the extent of the quantum confinement, the individual nanocrystal is described as a spherical potential box (quantum dot). According to the nanocrystal radius r, the degree of quantum confinement can be estimated.

A strong confinement regime occurs when $a_0 \gg r$. In this case, the Coulomb interaction becomes much larger than in bulk crystals because of confining the electron and the hole in a small volume. However, the Coulomb interaction can be neglected because the contribution of kinetic energies of the charge carriers are still much larger. Therefore, electrons and holes can be treated independently, because they are not assumed to form an exciton. Discrete energy levels appear in the electronic structure according to the following equation for the resulting band gap of quantum dot E_g^{tot} which can be calculated as a sum of fundamental bulk band bap E_g^0 and the confinement energy E^{conf} of both electrons and holes:

$$E_g^{tot}(D) = E_g^0 + E_{n,l}^{conf}(D) = E_g^0 + \frac{2\hbar^2 \chi_{nl}^2}{m_e^* D^2} + \frac{2\hbar^2 \chi_{nl}^2}{m_h^* D^2}, \tag{3}$$

where D is a spherical potential well diameter D and χ_{nl} are roots of the Bessel function, which are absolute values describing quantum numbers.

If $a_0 < r$, then weak confinement regime occurs, excitons can be formed, and the discrete energy levels are calculated according to the exciton effective mass. Thus, the shift of the energy levels here is much smaller when compared to the strong confinement regime. In case that $r > 2$–3 times a_0, the quantum confinement effect is no longer observable.

Regarding eq. 3, the band gap of semiconductor nanocrystals is size dependent, with decreasing size of the nanocrystal the band gap becomes larger. Furthermore, with increasing quantum confinement, discrete energy levels at the edges of the band gaps begin to appear, see in Figure 2 [17].

18
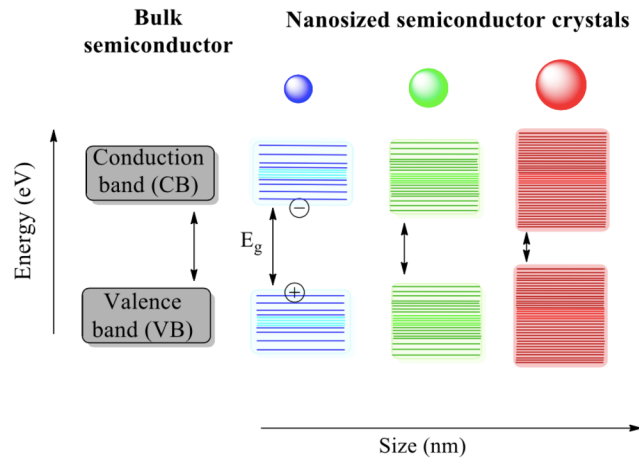
Figure 2: Electronic properties of bulk semiconductor compared to nano-sized semiconductor crystals with different sizes, modified from [17] and [18]

Here, we have reached the most significant advantages of low-dimension materials which is the possibility of varying the electronic structure and thus directly the possibility of changing electronic and optical properties according to the size and shape of nanoparticles [17]–[19] and [21]. According to the dimensionality, materials can be generally classified as following, for illustration, see also Figure 3.

- 3D materials, termed also as bulk materials, all dimensions are longer than 100 nm.
- 2D and 1D materials termed as low-dimension materials, one or two dimensions is shorter than 100 nm, respectively, 2D materials are usually in a form of film, platelets and networks, 1D materials are usually in a form of nanofibers, wires and rods.
- 0D materials with all three dimensions smaller than 100 nm, usually in a form of spheres and clusters special case are quantum dots [18] and [19].

Preparation of nanomaterials can be generally conducted with two approaches either top-down or bottom-up. The latter is the most common, it consists in the material growth control by establishing specific interactions, usually with the ionic precursors acting as ligands and capping agents. Also, the growth of the material can be confined to the matrix which predetermines the size and shape of the resulting nanomaterial [18]–[20]. In general, light-responsive semiconductive/conductive nanomaterials can be classified according to their composition.

a) Inorganic nanoparticles comprising elements from the II–VI (SdSe, CdTe, CdS, ZnSe), III–V (InP, InAs), and IV–VI (PbSe) groups.

b) Halide perovskite nanoparticles with general structure ABX_3, where A stands for monovalent cation (usually cesium cation (Cs^+), methylammonium (MA^+) or formamidinium (FA^+)), B stands for divalent cation and X represents a halide anion.

c) Metal nanoparticles, for example gold, silver or copper nanoparticles.

d) Up-conversion nanoparticles, a typical example is lanthanide ions doped matrix as $NaYF_4$ (Yb^{3+}, Er^{3+}).

e) Carbon based nanomaterials, as graphene, carbon nanotubes, carbon nanodots or fullerene.

f) Organic materials, for example hydrogen-bonded organic pigment nanoparticles [18] and [22].

Bulk 3D material

Bulk low-dimension material

Nanoparticles

3D	2D	1D	0D
x,y,z >100nm	x,y >100nm	x >100nm	x,y,z <100nm
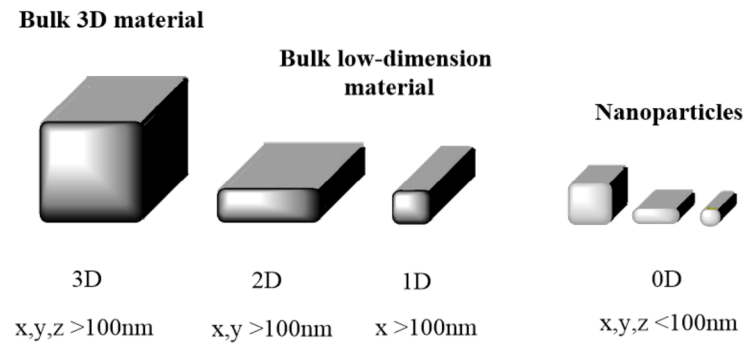
Figure 3: Classification of materials according to their dimensionality and shape, modified from [18]

Due to broad range of material variability and many possibilities how to optimize electrical, optical and mechanical properties, semiconductor materials can be used as advanced materials in many fields. They can be used for example for energy conversion, optical and optoelectronic and photovoltaics devices, optical imaging and biomedical sensing, detection and therapy [23].

20

4 Combining metal and semiconductor nanomaterials with bio-inspired molecules

As discussed previously, the bottom-up synthetic pathways of nanomaterials preparation typically consist in template or non-template control of the growth of the material. Considering the non-template control growth, surfactants are employed to passivate the surface of the resulting nanomaterial. The surface passivation helps to control the growth of the material and its stabilization [24]. Surfactants, also noted as detergents, ligands, molecular linkers, surface modifiers or capping agents, can be of various nature. Typically, they can be classified as cationic, anionic, zwitterionic and neutral according to the presence of charge among the molecule. The most common cationic surfactants are alkyl-based surfactants derived from ammonium and alkylammonium halides, such as oleyl ammonium halides or cetyltrimethylammonium bromide (CTAB). Regarding to the most common anionic surfactants, salts of long-chain carboxylic acids (i.e. sodium oleate) and long-chain sulfonic acids (i.e. sodium dodecyl sulfate, usually abbreviated as SDS) are typically employed for the surface passivation. As an example, alkyl betaine and lecithin can be mentioned as zwitterionic surfactants. And finally, polyethylene glycol can be considered as a typical neutral surfactant [24]–[26]. All above mentioned surfactants are commonly used, nevertheless, their use limits the applicability in functional devices in organic electronics because of the inert character of the organic molecules which modify the surface. Removal of the surfactants in post-synthetic modifications is possible by several approaches, nevertheless, quantitative ligand removal is time consuming, and moreover, the bare nanoparticles tend to aggregate [27].

Apart from above mentioned traditional ligands, alkane thiols, peptides, nucleic acids – deoxyribonucleic acid (DNA) and ribonucleic acid (RNA), tailor-made synthetic molecules and polymers among the others, can modify the interfacial behaviour and act as surfactants. Here, it is worth noting that the use of above mentioned molecules, does not only help to control the nanoparticles growth, but they also provide the resulting material with an additional functionality [24]. For example, bio-inspired molecules, such as peptides and DNA provide affinity to desired surfaces, sensing abilities or self-assembly properties. On the other hand, tailor-made conductive molecules or polymers can enable charge transfer among the nanoparticles and their environment [28]–[29].

K. E. Sapsford *et. al.* [30] summarized three possibilities of binding the ligands to the surface of nanoparticles for a model of ZnS nanoparticle (Figure 4). The ligands can be attached to the

surface of nanoparticles via a covalent coupling, direct attachment or noncovalent attachment [30]–[31]. Regarding the covalent coupling, the nanomaterial possesses functional groups available to form a covalent bond with ligands. For example, amines can be modified with N-hydroxysuccinimide (NHS) esters to form amide bonds. Thiols can be modified with maleimide derivatives or thiol exchange can take place on the nanoparticles surface. Last but not least, carboxylic acid functional groups can form amides with amino-functionalized biomolecules upon activation with 1-ethyl-3-(3-dimethylaminopropyl)carbodiimide (EDC). On the other hand, coordination of atoms comprising the nanomaterial enables a direct attachment of the ligands. For example, Zn atoms are known to coordinate with polyhistidine moieties in peptides. Simultaneously, S atoms can bind to cysteine side chains among the peptide backbone. Finally, there are a lot of noncovalent interactions that can take place in nanomaterial stabilization. For example, hydrophobic, electrostatic or highly specific interactions can help to bind the ligands. It is worth emphasizing here, that the surface modification by a desired biomolecule can occur straightforwardly as suggested in Figure 4 or by attaching a linker molecule possessing a specific bonding site for the desired biomolecule. A very traditional linker molecule is biotin which binds specifically to streptavidin. [30]–[31].

The further part of this work is restricted to bio-inspired surfactants and their ability to control the nanoparticles´ growth and provide them with additional functionality. From this point of view, commonly used nature inspired capping agents are often derived from peptides and nucleic acids. Both mentioned biomolecules are known for their abilities to form supramolecular self-assemblies and act as functional nanomaterials on their own. Considering their green nature, the possibility of tailoring their resulting morphology by tuning their primary structure, their easy doping and low price, both peptides and nucleic acids are considered as alternative semiconductors [28]–[29].

Conjugation of metal or semiconductor nanostructured materials with biomolecules can broaden their applicability because of increased functionality as mentioned previously. Bio-molecules decorating the surface of nanoparticles undoubtedly provide the resulting materials with unique properties and predetermine them to by employed in sensing and diagnostics in medical applications (optical, magnetic or electrochemical sensors), structured materials, energy and catalysis and in cleaning and purification procedures [28]–[29].
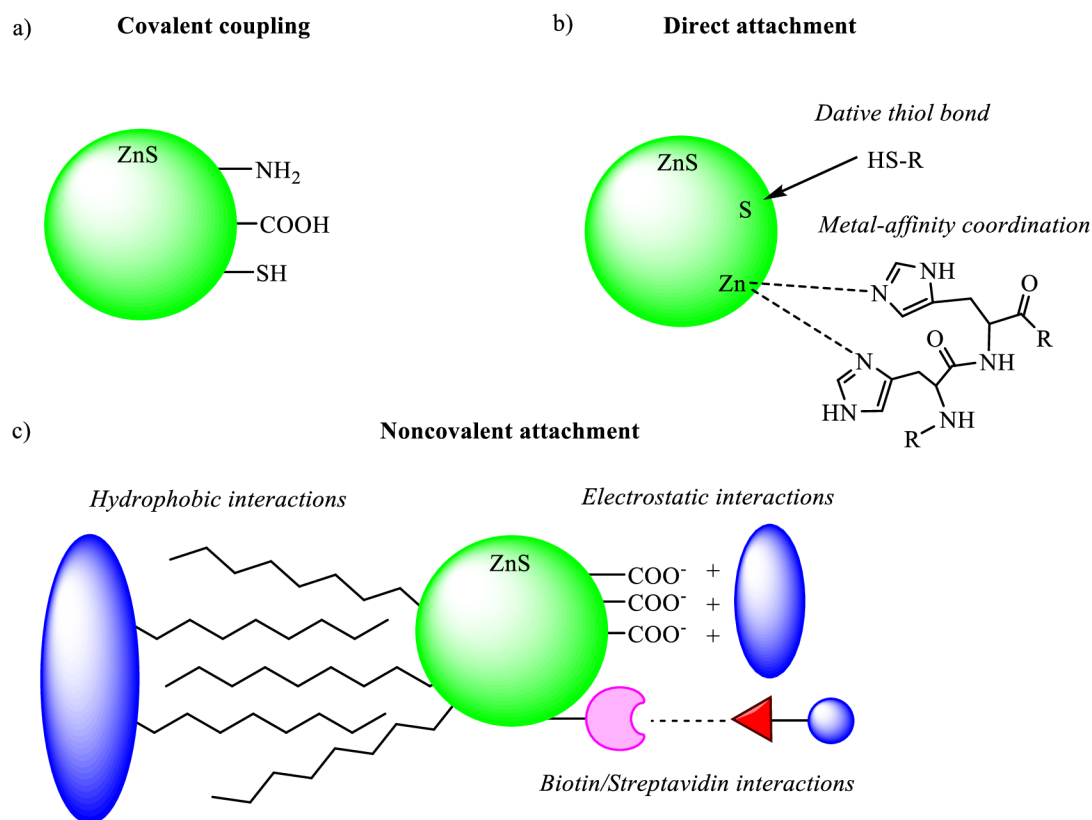
Figure 4: Three possible routes for surface modification of nanoparticles. Here, surface of ZnS nanoparticle is modified via a) covalent coupling, b) direct attachment of ligands and c) noncovalent attachment of ligands, modified from [30]–[31]

However, nanostructured materials can assist assembling and immobilization of biomolecules acting here as an inert matrix. This approach is typically used for enzymes immobilization for catalytic or oxidoreductive conversion applications. For instance, H. Seelarjoen *et al.* [32] recently immobilized enzymes of dehydrogenase on graphene to convert CO_2 to methanol. On the contrary, quantum dots are frequently used to organize biomolecules on their surface and visualize them [33]–[34]. This is typically needed for imaging techniques where the biomolecules need to be detected by optical, electrical, magnetical or even nuclear signals. This approach is already commonly used in medical applications [35].

4.1 Amino acids and peptides for the surface decoration

In general, proteinogenic amino acids possess carboxylic acid and amino groups and their side chains are additionally decorated with various functional groups, such as carboxylic acid, amino, thiol or hydroxyl groups, moreover, aromatic moieties can be found in the side chains. Hence, freestanding amino acids or side chains of amino acids among the peptide chain can

interact via hydrogen bonding, electrostatic interactions and π-π stacking with each other or with different molecules providing a broad variability of the supramolecular structures. The presence of different functional groups enables also their effective binding to surfaces of different solid phases, such as metals, metal oxides and compounds, magnetic materials, semiconductors, polymers, and minerals [28]–[29] and [36].

Amino acids or peptides are introduced into nanomaterials usually during the synthesis to enable a complex formation between heavy metal ions of the precursor and the corresponding functional group of the surfactant. The complex formation helps to coordinate the nanoparticle precursors and thus, the growth of nanoparticles is controlled effectively. Finally, the resulting surface is modified with desired functional groups providing the resulting nanomaterial desired properties, such as improved dispersibility in aqueous environment, biocompatibility or affinity to desired molecules [28]–[29].

However, amino acids and peptides can also be introduced to the nanomaterial during the post treatment modifications to replace more traditional surfactants which are efficient for the crystallization control [37]. Q. Ma *et al.* [38] utilized the ligand exchange for amino acids containing thiol groups (cysteine and homocysteine) sensing. They synthesized β-cyclodextrin modified gold nanoparticles with encapsulated rhodamine 6G to quench the luminescence via energy transfer. At isoelectric point of the corresponding amino acid, β-cyclodextrin bound via O-Au with binding energy of ~2 kcal·mol^{-1} was replaced by amino acid containing thiol group (cysteine or homocysteine) by forming S-Au bond with binding energy of ~40 kcal·mol^{-1}. Release of rhodamine simultaneously led to the recovery of the luminescence, proving sensing abilities of this system.

Already mentioned cysteine is an amino acid which is typically employed for the preparation and stabilization of the nanoparticles because of a thiol group in its side chain. Thiol groups are generally known to bind to sulphur and metal atoms, such as gold, zinc and cadmium on the nanoparticles surface [31] and [39]. For example, CdTe nanoparticles stabilized by cysteine were able to selectively bind lysine moiety in bovine serum albumin (BSA) via glutaric dialdehyde linker. As formed, bioconjugates exhibited resonance energy transfer from the protein unit to the nanoparticle presenting the so-called antenna effect [39].

Simultaneously, peptides and proteins can act as templates for the synthesis of nanoparticles. Designing the primary structure, i.e. the sequence of amino acids, among the peptide or protein chain can predetermine the resulting supramolecular structure – peptide rings, tubes or cages

24

can be obtained. The presence of a specific sequence of amino acids can initiate the growth of the nanomaterial [29]. For example, gold atoms can be coordinated with histidine side chains. Therefore, a histidine-rich peptide can serve as a matrix for gold nanoparticles assembled on peptides [40]. Considering this approach, cavities of different size and shape can be designed to obtain different metal nanostructures [41].

4.2 Nucleotides and nucleic acids for the surface decoration

Nucleotides and nucleic acids (DNA and RNA) have also been employed to control the nanoparticles growth and simultaneous surface decoration. Double-stranded DNA usually serves as a template for nanoparticles growth, for example, gold, silver and palladium nanowires were grown in the presence of DNA. On the other hand, a single-stranded DNA is preferably used for the non-template methods because of an availability of the purine and pyrimidine bases. The sequence of nucleobases and the length of the resulting chain is crucial for the determination of the resulting size and shape of nanoparticles [29]. For instance, a DNA oligomer consisting of 30 nucleotides units with only adenine and only cytosine assisted with the preparation of flower-like gold nanoparticles. Whereas, the oligomer consisting of only 30 thymine-based nucleotides enabled preparation of spherical nanoparticles suggesting that the functionality of the purine or pyrimidine base is crucial for the nanoparticle formation [42].

The influence of different functional groups of nucleotide triphosphates was studied by S. Hinds *et al.* [43] during PbS nanoparticles synthesis. They proposed that guanosine triphosphate (GTP) was efficient for the nanoparticles to control growth and additional stabilization compared to adenosine-, cytosine- and uracil-based nucleotides. The authors suggested that the triphosphate unit is responsible for the growth control whereas the amino group on the guanidine moiety is responsible for surface passivation. On the other hand, cytosine-based nucleotides exhibited the strongest affinity to silver clusters [44]. Hence, the nucleotides and polynucleotides need to be designed to specifically bind to desired materials. Q.-L. Wen and co-workers [45] have recently optimized a cytosine-rich DNA sequence to stabilize fluorescent silver nanoclusters for small molecules (such as ascorbic acid, dopamine and cysteine) detection, via photoluminescence quenching.

Finally, it is worth emphasizing that nucleotides and nucleic acids as well as amino acids and peptides are sensitive to their environment. Their ability to control the growth and stabilization of the resulting nanomaterial can be strongly affected by pH. For example, pH

changes lead to the production of different sizes of CdS nanoparticles stabilized by mononucleotide [46]. Simultaneously, both nucleic acids and proteins can undergo denaturation processes in a presence of strong acids, salts or organic solvents. Also, high temperature cannot be applied during the synthesis to avoid peptide denaturation [29] and [47]. All these parameters might act as a limitation for the traditional methods of synthesis for the preparation of nanoparticles.

5   Halide perovskite materials

The perovskite structure was described before the 20th century in calcium titanium oxide mineral of the chemical formula $CaTiO_3$. Considering here halide perovskite materials, the general structure is represented by formula ABX_3, where A and B stand for different cations and X stands for a halide anion (Cl^-, Br^-, I^-); the structure is introduced in Figure 5. Cation B is a divalent cation which stands in the centre of the unit cell and coordinates six halide anions $[BX_6]^{4-}$ [48]–[49]. This work focuses on lead halide perovskites (further noted as perovskites), though, tin, antimony or bismuth can represent the cation B as well [50]. Monovalent cation A balances a charge among the structure; it can be both of inorganic nature, such as cesium cation (Cs^+), or of organic nature, for example, methylammonium (MA^+) and formamidinium (FA^+) cations.

The mostly preferred structure of lead halide perovskites is cubic which is observed at higher temperatures. Cation B coordinates six halide anions forming an octahedra and cations A are arranged in a 12-fold cuboctahedral coordination, as indicated in Figure 5. With decreasing temperature, the octahedra are changing into tetragonal, orthorhombic, monoclinic or rhobohedral structures according to the perovskite structure composition. Characteristically, the cubic structure of perovskites exhibits the smallest band gap and the highest conductivity [48].
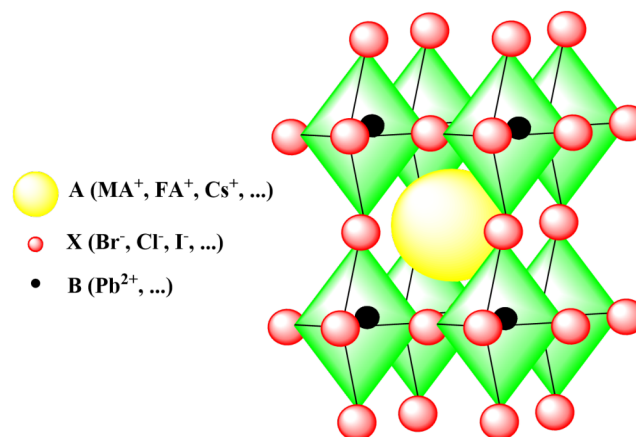

Figure 5: Metal halide perovskite general structure ABX₃, modified from [48]

The generation of a perovskite-like structure can be predicted by calculation a tolerance factor (*t*) by following equation:

$$t = \frac{R_A + R_B}{\sqrt{2} \cdot (R_X + R_B)},$$

(4)

where R_A, R_B and R_X stand for ionic radii of the corresponding ions. In optimal case, t value is in the range 0.9–1, then ions A and B have an ideal size and the structure is cubic. When A is large and B is small, then tolerance factor is higher than 1 and the structure is hexagonal or tetragonal. On the contrary, i.e. A is small or B is large, then the tolerance factor is in a range of 0.71–0.9 and the structure is orthorhombic/rhombohedral [48], [49] and [51].

Electronic properties of perovskite materials were firstly studied in the 1990s by Mitzi′s group for tin halide perovskites [52]. Organometal halide perovskites were firstly supposed to be used for solar cell fabrication by T. Miyasaka et al. [53] in 2009. A real breakthrough came in 2012 when Henry J. Snaith and co-workers [54] prepared the first efficient organometal halide perovskite-based solar cell. Since that time, a power conversion efficiency (PCE) has increased from 3.8 % to 25.2 %, even to 29.1 % when perovskite/Si tandem devices are taken into an account [5]. This determines halide perovskites as the most promising materials in the photovoltaic field. According to theoretical calculations, the electricity conversion limit of a methylammonium lead iodide ($MAPbI_3$)-based solar cell is about 31% [55].

Halide perovskite materials are not suitable only for solar cells fabrication, but also many other functional devices as LEDs [56], lasers [57], ultraviolet-to-infrared photodetectors [58], X-ray [59] and γ-ray [60] detectors have been reported. This broad range of applications is possible due to unique properties of perovskites, such as suitable bandgap engineering [61], high absorption coefficient and tunable optical properties [62], low exciton binding energy [63], long and balanced electron–hole diffusion lengths [64], high carrier mobility [65] and high defect tolerance [66].

Nowadays, a considerable number of publications focuses on mixing of individual cations or anions [67]. The substituted ions act as dopants and their incorporation is possible directly during the synthetic procedure or it can be partially performed by post-treatment modifications. The doping can help to precisely tune band gap, charge carrier lifetime and trap density for fabrication of high-performance and long-term stable optoelectronic and photovoltaic devices [67]–[68]. For example, L. Chen *et al.* [69] focused on combining mixed lead halide perovskite. A single crystal with a new composition $(FAPbI_3)_{0.9}(MAPbBr_3)_{0.05}(CsPbBr_3)_{0.05}$ was prepared. This composition provided the material with appropriate band gap, long carrier lifetime and higher stability under water, oxygen, light and thermal exposure.

Additionally, the central atom can be partially or fully substituted in the perovskite structure. Actually, considering lead as a toxic material causing damage to the nervous system and can

cause brain disorder and even death [70]. Therefore, a replacement of lead by an alternative cation B is currently the greatest challenge [71]. The most promising candidates to replace lead are predominantly metals from IIA and IVA groups, such as Sr^{2+}, Sn^{2+}, Ge^{2+}. However, other transition metals (like Cu^{2+}) incorporated in the perovskite structure exhibit a potential to be applicable or solar cells fabrication. Trivalent metal ions are able to form a perovskite structure as well; the general formula of the resulting material is then $A_3B_2X_9$. The VA group metals, for example Bi^{3+} and Sb^{3+}, were considered to be the candidates for lead replacement. Finally, also tetravalent ions, mainly Sn^{4+} were examined to form a general perovskite-like structure with general formula A_2MX_6. Nevertheless, it has not been prepared any lead-free perovskite structure yet which would exhibit comparable or even better electrical properties alongside better stability against moisture and ambient conditions [50] and [72].

5.1 Dimensionality of lead halide perovskites

Even though the perovskite structure is highly defect-tolerant, there are still demands to obtain homogeneous composition with as few crystal boundaries as possible [48] and [73]. One approach to control crystal boundaries is a single crystal growth. Bulk lead halide perovskites are quite easy to grow up to a few mm sized single crystals by inverse temperature crystallization [74]–[75]. Our group has recently described a microwave assisted inverse temperature crystallization providing single crystals of high quality [76]. Nevertheless, the crystallization is much more time consuming when compared to polycrystalline thin film formation. The polycrystalline film formation is low-cost and is easy to be up-scaled; the preparation usually lies in spin-coating of precursor solution and subsequent temperature treatment [73] and [77]–[78]. The performance of the functional devices can be further improved by employing additives into the precursor solutions [79] or by various post-treatment processes [80].

On the other hand, preparation of nano-structured perovskite materials reduces both the time demands and the problems with ground boundaries. Moreover, nano-scaled perovskite materials possess unique physical properties, such as high PLQYs and wide optical band gaps, besides, optical properties can be precisely tuned because of quantum confinement effects [81].

There are several approaches for the nano-structured perovskite materials synthesis. In general, bottom-up approached synthesis consists in the preparation of precursor solution, the subsequent crystallization is controlled either by surfactants or by a porous template [48] and [73]. The mechanism of surfactant-guided nanocrystal formation resides in placing a primary ammonium salt instead of the cation A in order to stop the crystallization in one or more dimensions. For further stabilization long-chain carboxylic acids (such as for example oleic acid) are applied as capping agents, schematically presented in Figure 6 [7]. Regarding the choice and molar ratios of surfactants and the reaction conditions, various size and shape of nanoparticles can be obtained – from quantum dots and nanocubes, nanorods or nanowires to nanoplatelets, schematically shown in Figure 7 [82]. Considering the nanoparticles prepared by the surfactant-assisted approach, colloidal solutions are obtained directly after the preparation and they can be processed further by various deposition techniques (spin-coating, drop casting or ink-jet printing) [48].
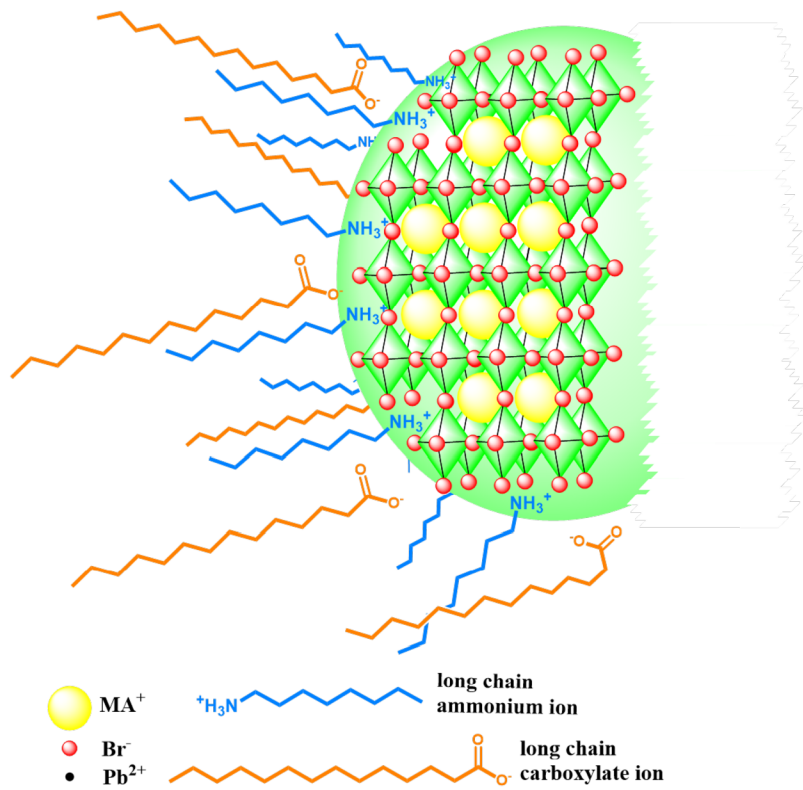
Figure 6: Low dimensional MAPbBr₃ perovskites structure passivated with capping agents, modified from [7]
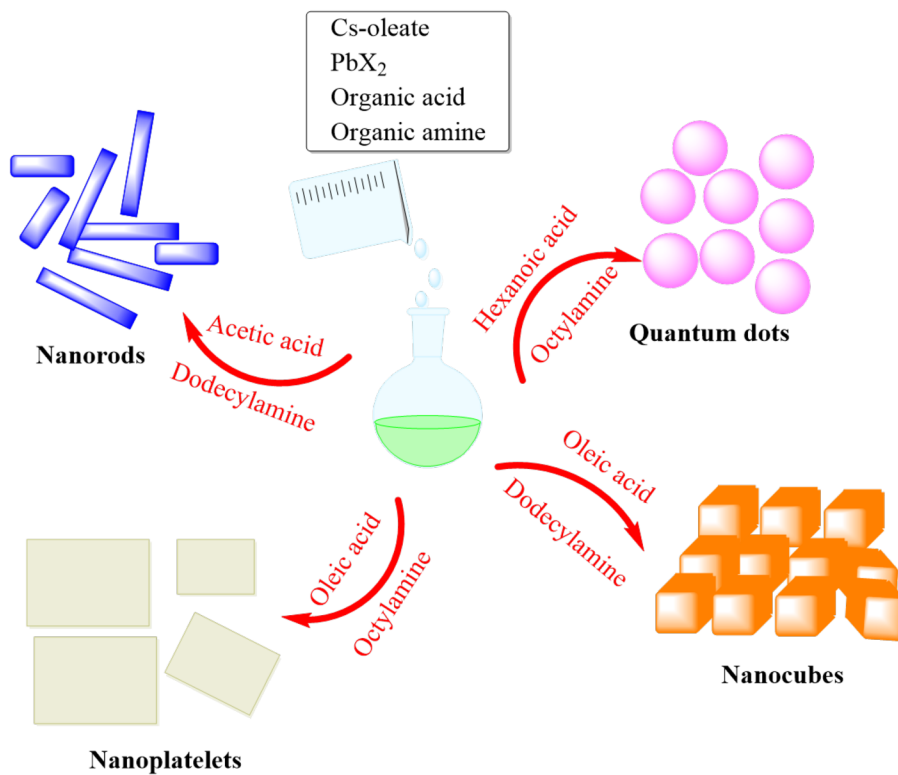

Figure 7: Variability of nanocrystals shape according to capping agents variations, modified from [82]

On the contrary, the porous template does not embed any surfactants into the perovskite structure, it only sterically constrains the crystal to grow into defined size and shape. Different matrices for the controlled growth of nanocrystals have been reported, for example ordered mesoporous silica, titania, alumina [83] and organic polymers [7].

Several reports introduced a top-down approach for perovskite nanoparticles preparation. For example, nanosheets were prepared by exfoliating bulk perovskite crystals in the presence of capping agents [84]. Also, nanostructured perovskite material can be prepared from thin films by laser ablation techniques [85].

Formed low dimensional halide perovskites can have defined structure divided according to the dimensionality:

a) 0D nanostructured halide perovskites as nanocrystals or even quantum dots,
b) 1D nanostructured halide perovskites as nanorods or nanowires,
c) 2D nanostructured halide perovskites with lateral structure [48], [73] and [86].

5.1.1   0D nanostructured lead halide perovskites

The very first preparation of 0D nanostructured lead halide perovskites was described by L.C. Schmidt *et al.* in 2014 [87]. MAPbBr$_3$ nanocrystals stabilized by a long-chain ammonium salt (octylammonium bromide or octadecylammonium bromide) alongside oleic acid were prepared by a hot injection method. Briefly, MABr and PbBr$_2$ were dissolved in *N,N*-dimethylformamide (DMF) in advance and their solution was mixed with a solution of capping agents in octadecene acting here as non-coordinating solvent at 80 °C. As prepared warm precursor solution was precipitated by an addition of acetone which resulted into a formation of nanoparticles. The nanoparticles were easily dispersible in toluene after a purification procedure. Octylammonium-stabilized perovskite nanocrystals were 6.2 ± 1.1 nm in size with an emission maximum of 527 nm and a PLQY of 17% in toluene colloidal solution. The colloidal solutions were successfully spin-coated onto quartz substrates and the films exhibited emission maximum of 533 nm and PLQY of 23%.

Even more facile and easily up-scalable is a ligand-assisted precipitation (LARP) technique for the preparation of perovskite nanoparticles. The ligand-assisted precipitation technique for MAPbBr$_3$ quantum dots synthesis was firstly introduced by F. Zhang *et al.* [7] in 2015. Typically, a precursor solution was prepared in advance, it contained PbBr$_2$, MABr alongside

the capping agents (*n*-octylamine and oleic acid) in DMF which acted as a good coordinating polar solvent. The precursor solution was then precipitated in a poor nonpolar solvent (typically toluene) and a strong colour change indicating the formation of nanoparticles was immediately observed. After a purification procedure, toluene colloidal solutions were studied, an emission maximum was of 515 nm and a PLQY was in the range of 50–70 %. The presence of nanoparticles with an average size of 3.3 ± 0.7 nm was confirmed by transmission electron microscopy (TEM).

It must be emphasized, that the precipitation techniques are versatile, they can be easily modified to obtain perovskite nanoparticles of desired composition and properties. For example, MAPbX$_3$ perovskites nanoparticles exhibit light emission in a range 438–660 nm according to a loading of halide anions, see images of different colloidal solutions in Figure 8. Bromide based perovskite nanoparticles exhibit green light emission, presence of chloride or iodide anions causes blue and red shift, respectively [8]. As described tuning of the optical properties is applicable also for FA- and Cs-based perovskite structures [88]–[89].
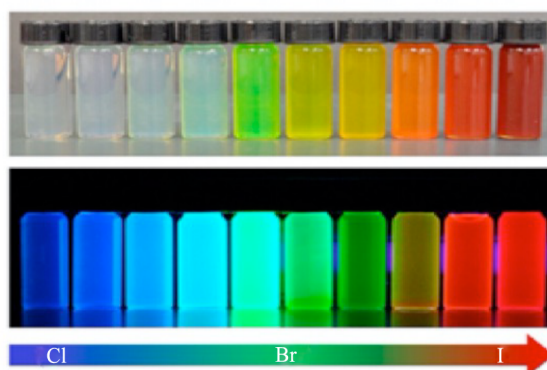
Figure 8: MAPbX₃ colloidal solutions stabilized by octylamine in toluene with different X anion loading, the upper image under ambient light and the bottom image under UV lamp, adapted with permission from [8]. Copyright © (2016) American Chemical Society.

Modifying the nanoparticles composition, the solvent system needs to be primarily optimized. In general, DMF, dimethyl sulfoxide (DMSO) and γ-butyrolactone (GBL) are typically used as strongly coordinating aprotic and highly polar solvents for the preparation of precursor solutions. While DMF and DMSO are typically applied for MAPbX$_3$ perovskites preparation, GBL is typically used for FAPbX$_3$ perovskites preparation [88]. It is worth noting, that strongly coordinating polar solvents are difficult to be completely removed during the precipitation or further purification. The possible residua of the polar solvents occupying the crystal surface cause a fast degradation of the perovskite structure (especially in MAPbI$_3$

nanocrystals) [90]. The strength of a coordination can be for example weakened by additions of different solvents into the precursor solution [91]. Considering the precipitation media, toluene, hexane or octadecene are typically chosen as noncoordinating nonpolar solvents inducing the crystallization [90].

Last but not least, different capping agents for nanoparticles stabilization can be chosen. As mentioned previously, long-chain ammonium salts (for instance *n*-octylamine) alongside long-chain carboxylic acids (for example oleic acid) are employed [7] and [87]. However, various capping agents with ammonium and carboxylic acid groups can be chosen. The choice of the capping agents does not only limit the size and shape of the prepared nanoparticles, but it may also functionalize the surface of nanoparticles by introducing various functional groups.

Considering the suitability of the capping agents, the nature of binding of the ligands to the perovskite core must be evaluated. Capping agents are generally bound electrostatically to the perovskite structure (see also Figure 6). J. De Roo *et al.* [92] proposed that several Brønsted acid-base equilibria can occur on the nanoparticles surface because of the strong dynamic character of the binding of ligands (Figure 9). Firstly, primary amine can undergo an interaction with hydrogen bromide to form primary ammonium salt which passivates the surface of nanoparticles. Secondly, unprotonated primary amines can coordinate directly the surface cations via its free electron pair. And finally, primary amine can be involved in acid-base equilibrium with carboxylic acid. The resulting ion pair can passivate the surface of nanoparticles.
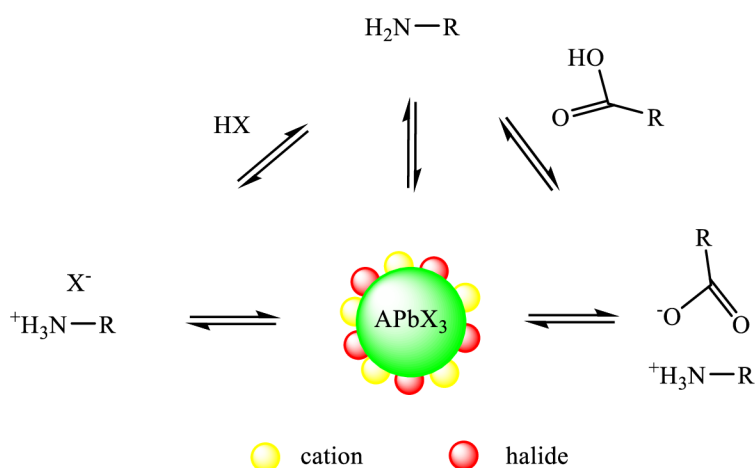
Figure 9: Equilibria between amino- and carboxylic acid-based capping agents employed for perovskite nanoparticles stabilization, modified from [92]

34

Due to the equilibrium states, the ionic interaction can be easily weakened, especially upon isolation and purification of the nanoparticles. Elimination of capping agents leads to the aggregation of the nanoparticles and bulk polycrystalline material formation. F. Krieg *et al.* [93] reported that the incorporation of zwitterionic capping ligands enhances the nanocrystals stabilization. They suggested structures of long-chain sulfobetaines, phosphocholine and γ-amino acids to be the most suitable as capping agents for nanoparticles formation and stabilization. Recently, $CsPbBr_3$ nanoparticles were embedded into poly(*n*-butyl methacrylate-co-2(methacryloyloxy)ethyl-sulfobetaine) copolymer possessing zwitterionic side chains among the copolymer backbone available for the nanoparticles stabilization [94]. The nanocomposite was further processed into films and possessed improved stability and resistance to water.

On the other hand, the ionic interaction of ligands with the perovskite core enables a post-synthetic exchange of ligands. Capping agents which are the most efficient for nanoparticles stabilization can be easily replaced by different ones which enhance coupling between nanoparticles and improve charge transport. This approach was recently described by L. M. Wheeler *et al.* [95] for $CsPbI_3$ quantum dots. Firstly, $CsPbI_3$ quantum dots stabilized by oleylamine and oleic acid were prepared by classical hot-injection method. Then, quantum dots were spin-coated onto TiO_2 substrate and the ligand exchange followed by dipping the films into relevant saturated solutions – oleic acid was replaced with acetate anions and oleylamine was substituted with formamidinium cations.

As suggested above, long-chain capping agents are not a good choice for stabilization because they are not charge transport-compatible. For many applications (for instance thermoelectric devices or solar cells), complete removal of capping agents is necessary. The quantitative removal of capping agents usually demands high temperature and pressure which can be harmful for the perovskite core [96]–[97]. Therefore, targeting the choice of the capping agents at the desired application is necessary. The preferred capping agents can be employed directly during the nanoparticles preparation [98] or they can be incorporated during the ligand exchange post-treatment [90].

Very effective approach of perovskite nanoparticles stabilization was introduced by S. González-Carrero and co-workers [98] who used 2-adamantylammonium bromide as the only capping agent which was embedded into the perovskite structure via the ligand-assisted precipitation technique. The incorporation of adamantane moieties for enhancing thermal and optical properties as well as self-organization of functional materials was already described

previously [99]–[100]. In S. González-Carrero *et al.* work [101], different carboxylic acids were tested for better perovskite nano-structure stabilization. The best combination was 2-adamantylamine alongside a short-chain carboxylic acid, namely propanoic acid. As stabilized perovskite nanoparticles exhibited extremely high PLQY up to 98 % with emission maximum at 516 nm. In addition, homogeneous densely packed thin films were prepared by centrifugal casting where adamantane moieties passivated the grain boundaries and supported the charge transport.

Adamantane-based ligands exhibited improved optical properties even when incorporated by post-synthetic ligand exchange by Y. Hassan *et al.* [90]. They replaced original capping agents, namely oleic acid and oleylamine, with 1-adamantanecarboxylic acid and 3-aminopropylphosphonic acid on the surface of $MAPbI_3$ nanoparticles. Integration of adamantane moiety improved the PLQY which increased from 40–60 % to 60–85 % in toluene solutions.

Surface decoration with more complex ligands which can enhance self-organization was presented by S. Wang *et al.* [102] who modified the surface of PNP with protonated melamine by the ligand-assisted precipitation technique. Ammonium functional group of melamine passivated the surface traps by ionic interaction with $[PbBr_3]^-$ complex while nitrogen heteroatoms passivated the under-coordinated Pb atoms by their free electron pairs. Furthermore, free amino groups formed hydrogen bonds among the others which led to the efficient passivation of the perovskite core.

One of the last trends in ligand engineering finds an inspiration in nature. Natural amino acids are capable of controlling perovskite structure growth due to a presence of both primary amino and carboxylic acid groups. Preliminary results came from B. Luo *et al.* [103] who incorporated non-proteinogenic amino acids into the perovskite structure. They used bifunctional 12-aminododecanoic acid as the only capping agent which stabilized the perovskite structure. According to the ligand loading, nanoparticles of an average size of 3.9–8.6 nm were prepared.

Recently, S. Wang *et al.* [104] used cysteine as a trifunctional ligand for $MAPbBr_3$ perovskite nanoparticles synthesis. Synergistic effect among amino, carboxylic and thiol groups passivated the nanoparticles´ surface effectively because of their self-assembly tendency. Additionally, glycine was studied for perovskite nanoparticles stabilization as well [103]. Also,

36

tryptophan, histidine, leucine and phenylalanine were used for nano-structured perovskites synthesis, see below [105].

Apart from the hot-injection and the ligand-assisted precipitation methods of perovskite nanoparticles preparation, a broad variety of matrix assisted crystallization techniques have been reported. The matrices can be both of inorganic and organic nature and their morphology predetermines the size and shape of the resulting nanoparticles. Regarding the inorganic-based matrices, for example, nanoporous silica and alumina were tested for the nanocrystals growth control [83]. Here, the templating was confined to the thin films. On the contrary, mesoporous silica nano- and microparticles were used for controlling the growth of perovskite nanocrystals within the pores [106]. The resulting composite material was dispersible in toluene and further processing (i.e. spin-coating) was possible.

Also, organic matrices were employed to control the perovskite crystallization. For example, organic polymers such as polystyrene (PS), polycarbonate (PC), acrylonitrile butadiene styrene (ABS), cellulose acetate (CA), polyvinyl chloride (PVC), and poly(methyl methacrylate) (PMMA) were tested [107]. In this approach, swelling of the polymer films in polar solvents (i.e. DMF) was used for perovskite precursor solutions soaking into the polymer matrix. Further annealing removed the solvent and crystallization occurred. Nanoparticles embedded in the polymer films exhibited improved stability in the water environment. Especially nanoparticles embedded in the ABS matrix in which the PLQY dropped from 48 to 45% while being immersed in water over the period of 60 days. Even better control of the perovskite nanocrystal growth was observed in the micelle-template approach [108]. Here, diblock copolymer (poly(styrene-*b*-2-vinyl-pyridine)) formed micelles of defined size and shape in toluene. The micelles acted as nanoreactors for the formation of perovskite nanoparticles.

5.1.2 1D nanostructured lead halide perovskites

1D nanostructured halide perovskites, such as nanorods and nanowires, have one common feature – always two dimensions are in the nanoscale and the third is macroscopic. Comparing them to 0D materials, still, quantum confinement effect can take place, optical properties tuning is possible via modifications in the composition and surface-to-volume ratio is large. On the other hand, 1D nanostructured perovskites enable a charge transport over a long distance without excessive hopping and also, flexible conductive percolation network can be formed [73] and [109]. There are several methods for 1D nanostructured lead halide perovskites

preparation. Whether various solution-phase growth or vapor-phase growth techniques can be applied for the preparation of the nanocrystals, which were detailly listed by K. Hong *et al.* [73] in a review.

Focusing on surfactant-directed solution-phase growth, very similar methods as for 0D nanostructured lead halide perovskites are applied. Therefore, a suitable solvent system is needed to be found and different capping agents can be applied for the 1D perovskite shape and size tuning. There is also observed an influence of the concentration of precursor chemicals, a ratio of capping agents, reaction temperature and reaction time on the resulting morphology of the 1D nanocrystals [48] and [110]–[111].

The very first synthesis of $CsPbX_3$ (where X was Br or I) nanowires was described by D. Zhang and co-workers [111] who studied mainly the influence of the reaction temperature and time. As capping agents, oleic acid and oleylamine were used and the reaction was proceeded in octadecene at 150–250 °C. When the reaction time was 10 min, nanocubes were dominantly formed, when reaction time was prolonged, nanowires started to be formed, the preferential formation of nanowires was observed after 90 min. When the reaction proceeded for a longer time, bulk crystals were formed.

The influence of capping agents choice was described by M. Imran *et al.* [112] who prepared various $CsPbBr_3$ nanowires with width ranging from 3.4 to 20 nm by changing the ratio of different capping agents (oleylamine/octylamine and hexanoic acid/octanoic acid) as well as by the reaction temperature and time. The addition of the short chain carboxylic acid caused the formation of nanowires with the width below 10 nm. On the other hand, addition of oleic acid together with octanoic acid led to the formation of nanoplatelets[113]. The nanowires colloidal solutions exhibit bright photoluminescence as well as 0D perovskite nanocrystals; the highest reached value of PLQY was 77 % for cesium lead halide nanowires of 5.1 nm width in solution [112].

$CsPbX_3$ nanowires with different halide composition can be also prepared through post-synthetic anion exchange reactions of $CsPbBr_3$ with I^- or Cl^- precursors (oleylammonium halide or PbX_2). Here, optical properties were tuned across the visible spectral region (409–680 nm) [114]. Optical properties can be tuned also by a method described by D. Amgar *et al.* [115] who introduced hydrohalic acids (HCl, HBr and HI) into the reaction mixture during the nanowires´ synthesis. First of all, incorporation of different ratios of halide anion led to the tuning of optical properties, emission spectra were shifting in the range of approx. 420–550 nm.

38

Furthermore, it was found out that with increasing loading of hydrohalic acid the length of nanowires was shortening. The authors assumed that hydrohalic acids help to protonated primary amine ligands and thus cause better perovskite structure passivation.

Surfactant-directed solution-phase growth of MAPbBr$_3$ perovskite nanowires is very similar to the previously described synthesis of CsPbX$_3$ 1D nanostructured crystals. For example, octylamine and oleic acid can be used as capping agents to control the crystallization of perovskite structure into nanowires. Very similarly, the reaction time and temperature in octadecene have a crucial effect on the resulting optical properties of colloidal solutions [109]. F. Zhu et al. [116] studied the influence of composition, solvent system and reaction time on the resulting morphology of MAPbX$_3$ nanocrystals. Here, the authors prepared MAPbI$_3$ nanowires, nanorods and dots as well as MAPbBr$_3$ nanowires and nanoplatelets.

S. Aharon and L. Etgar [117] succeeded in the synthesis of MAPbI$_3$ and MAPbBr$_3$ nanorods stabilized by octylammonium and oleic acid. It is worth noting, that the halide composition did not have any significant effect on the resulting morphology, it only led to the changes in optical properties.

5.1.3 2D nanostructured lead halide perovskites

Various 2D nanostructured lead halide perovskites such as nanoplatelets and nanosheets can be prepared by very similar surfactant-directed solution-phase growth procedures as 1D nanocrystals. Nevertheless, various different methods were reported, for example chemical vapor deposition techniques [118] or top-down processes consisting in exfoliating bulk perovskite crystal in the presence of capping agents [84].

Thanks to a broad variability of perovskite crystal composition and a possibility of the use of different combinations of capping agents during the surfactant-directed solution-phase growth procedure, the size and the shape of individual nanocrystals can be tuned precisely. As mentioned previously, it is very important to control the reaction conditions during the synthesis of nanomaterials, especially, reaction temperature and time, precursors ratio and the ratio of capping agents and the solvent system [82], [113], [116] and [119].

Long-chain-based ligands do not have to serve as the only capping agents. G. H. Ahmed and co-workers [120] proved that the pyridine alongside oleic acid and oleylamine passivated efficiently the surface of the perovskite MAPbBr$_3$ 2D nanocrystals during the ligand-assisted

precipitation technique. According to calculations, a free electron pair of nitrogen from the pyridine coordinated the lead atoms on the surface of nanoparticles which enhanced the stabilization of nanostructured perovskite. Furthermore, it was observed that the precipitation temperature affected the resulting thickness of nanosheets causing quantum confinement effects. Similarly, J. Zhao *et al.* [121] stabilized $CsPbBr_3$ nanoplatelets by tryptophan with oleic acid and oleylamine alongside. The presence of tryptophan caused preferential formation of $CsPbBr_3$ nanoplatelets instead of nanocubes. Furthermore, different histidine loading causes optical properties tuning by varying the thickness of the nanoplatelets due to quantum confinement effects. Other amino acids (cysteine, histidine, leucine and phenylalanine) did not have such effects on the morphology and optical properties of the resulting nanomaterials.

Special case of quasi-2D nanostructured lead halide perovskites are 2D/3D structures which are called as Ruddlesden-Poppper or Dion-Jacobson perovskites [122]–[123]. Their preparation usually consists in a preparation of precursor solution containing perovskite precursors with primary ammonium halide salt, the precursor solution is spin-coated onto the substrate where the crystallization occurs. Because of the presence of bulk ammonium salts which are passivating the perovskite surface, only a few layers of perovskite structure can be formed. The concentration of the ligands controls precisely the number of perovskite layers *n*. According to a valency of ammonium salts, Ruddleden-Popper (monovalent cations) and Dion-Jacobson (divalent cations) perovskite structures can be formed as suggested in Figure 10.

Phenylethylammonium iodide/$MAPbI_3$-based perovskite solar cell was firstly prepared by I. C. Smith et al. [124] in 2014, the power conversion efficiency was 4.7 % what is quite low value when compared to a common $MAPbI_3$ solar cell structure where the power conversion efficiency was 15 %. On the other hand, the group described lower moisture sensitivity of the solar cell.

Then a lot of research groups focused on the ammonium ligands choice and for example butylammonium halide [125]–[126] or anilinium halide [127] were used for the layer growth control. It was always described that optical properties are strongly dependent on the film thickness because of quantum confinement size effect. The ammonium ligands don't have to serve only as capping agents for the crystallization to be stopped, their incorporation into the structure can also bring some advanced functionality. For example, already mentioned anilinium halide 2D/3D perovskites exhibited enhanced electrical properties because of the presence of conjugated anilinium structure [127].
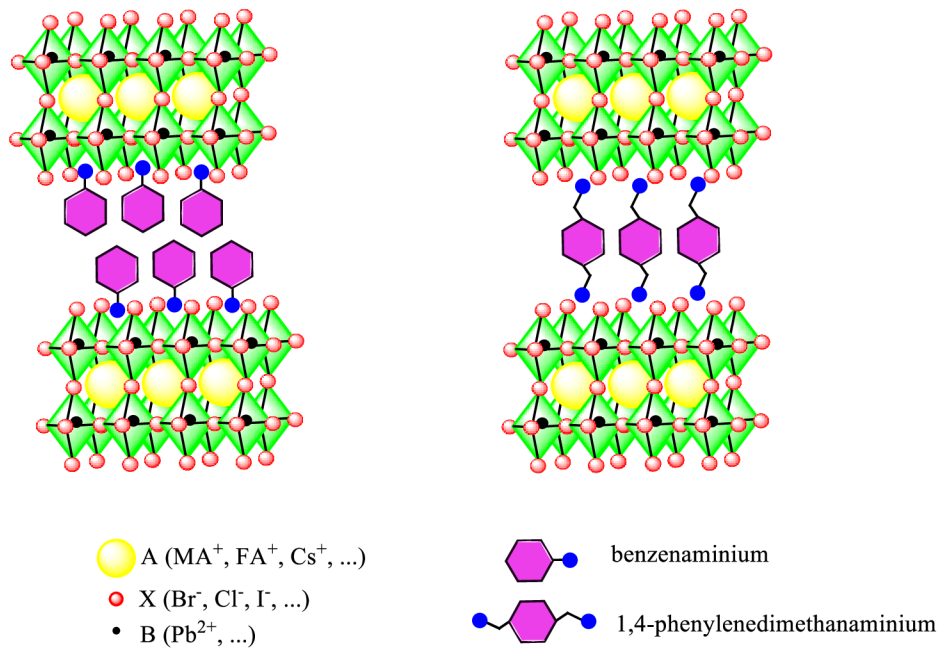
Figure 10: Structure of quasi-2D nanostructured lead halide perovskites, an example of Ruddlesden-Poppper and Dion-Jacobson types of 2D/3Dperovskite structures (from left to right), where n = 2. Modified from [123]

T. Zhang *et al.* [128] introduced bifunctional 5-aminovaleric acid into the MAPbBr$_3$ structure in order to crosslink perovskite layers. The crosslinking is possible because protonated ammonium groups act as cation A in the perovskite structure and thus stop the crystallization, on the other side, deprotonated carboxylate groups coordinate the surface Pb of the neighbouring layer.

5.2 Applications

5.2.1 Solar cells

While bulk perovskite crystalline structures are applicable into photovoltaic devices where they exhibit excellent properties, nano-structured perovskite materials are not suitable for solar cells fabrication because of the presence of capping agents with insulating properties. One approach to avoid decreasing mobility is the ligand removal by post-synthetic treatment. For example, E.M. Sanehira *et al.* [97] introduced removal of capping agents from $CsPbI_3$ quantum dots surface and replacing them by FAI, solar cell fabricated from modified perovskite nanoparticles exhibited PCE 13.4 %. The post-synthetic treatment led to improved mobility, whereas $CsPbI_3$ quantum dots thin film mobility was 0.23 $cm^3V^{-1}s^{-1}$, mobility of $CsPbI_3$ quantum dots film treated with FAI was 0.50 $cm^3V^{-1}s^{-1}$. For comparison, the common $MAPbI_3$ thin film mobility is 2.3 $cm^3V^{-1}s^{-1}$.

On the other hand, 2D/3D nano-structured perovskites seem to be highly applicable for solar cell fabrication. Various capping agents like for example butylammonium, phenylethylammonium [122], [124] and [129] or multifunctional aminovaleric acid [130] or ethylendiamine [131] as crosslinking agents were added. The 2D/3D structure helps to reduce the presence of grain boundaries and furthermore, the incorporation of organic capping agents not only helps to control the crystallization process but it also increases long term stability because of lower moisture sensitivity of the resulting film [130].

5.2.2 Light emitting diodes

The very first LED was described by T. Hattori and co-workers [132] in 1996. The active layer was formed from 2D phenylethylammonium iodide/$MAPbI_3$ perovskite. Nevertheless, the working temperature was 110 K and thus, it did not gain much attention. A real breakthrough came when L. C. Schmidt *et al.* [87] described the preparation of highly luminescent colloidal solutions of perovskite nanoparticles. The colloidal solutions can be easily processed into films, for example by spin-coating, centrifugal casting or ink-jet printing [133]. Nevertheless, there are different approaches for the active layer preparation, for example, they can be embedded into matrices. $MAPbBr_3$ nanocrystals stabilized by n-octylamine were used for LED fabrication [7] and [134], in both cases were the nanoparticles, quantum dots and nanoplatelets, respectively, embedded into a polymer matrix (poly(methyl methacrylate) and poly(9-vinylcarbazole):2-(4-biphenylyl)5-phenyl-1,3,4-oxadiazole, respectively) in order to enable spin-coating of the functional layer. For nanoparticles stabilization can be also porous matrices

used, for example S. Demchyshyn *et al.* [83] grew the perovskite nanoparticles in nanoporous silica and alumina thin films and as prepared active layer was used for LEDs fabrication.

All-inorganic perovskite nanocrystals are studied for the LED fabrication as well, they even exhibit higher stability and thus also the higher stability of the devices is achieved compared to hybrid structures [135]. The first all-inorganic perovskite LED was described by J. Song and co-workers [136], here n-octylamine and oleic acid were used as capping agents as well. In this case, nanoparticles colloidal solutions were only spin-coated onto the desired substrate without any polymeric matrix use.

There are several approaches to enhance the LED efficiency can be enhanced. First of all, the homogeneity can be increased by cross-linking agent addition, for example G. Li *et al.* [137] applied trimethylaluminum as the cross-linking agent after the all-inorganic nanoparticles film deposition. Furthermore, the efficiency can be increased by properly washing nanoparticles, nevertheless, the ionic interaction between capping agents and the perovskite structure is not strong enough to keep the surfactants bonded while nanoparticles being purified. If capping agents are washed out, the colloidal stability decreases and the nanoparticles aggregate quickly. Various research groups tried to find a solvent system for efficient but gentle washing of unreacted material from the crude colloidal solutions to keep the surface ligand density [138] and [139].

5.2.3 Lasers

High PLQYs predetermine perovskite nanoparticles to be applicable also in optical lasing devices. Another advantage of perovskite structure is also the possibility of varying the optical properties by composition and thus tuning the emission wavelength. Hybride lead halide perovskite nanowires were used for laser fabrication by H. Zhu *et al.* [140] as well as by J. Xing *et al.* [141]. Q. Zhang *et al.* [143] studied fully inorganic perovskite nanoplatelets for lasing abilities.

5.2.4 Photodetectors and other applications

Finally, there should be also mentioned possibilities for fabrication photodetectors from perovskite nano-structured materials [9].

Perovskite material can be employed in hydrogen halide gas sensing; exposure of the perovskite material to halic acid leads to reversible ion exchange which can be detected by colour change [142]. And furthermore, recently, Y.-F. Xu and co-workers [144] used a $CsPbBr_3$ perovskite quantum dot/graphene oxide composite for photocatalytic CO_2 reduction.

6 Experimental part

This section describes used materials, samples preparation and characterization methods.

6.1 Materials

All chemicals were used as received without any further purification.

Perovskite precursors

Lead (II) bromide (PbBr$_2$ 99.999%) was purchased from Sigma Aldrich. Methylammonium bromide (MABr, 98%) was purchased either from Sigma Aldrich (sections 7.1, 7.2, 7.4 and 7.5) or from GreatCell (section 7.3).

Amino-based capping agents:

Adamantyl-1-amine (AdNH$_2$) was obtained from Provisco CS. L-Arginine (98%) and L-Lysine (97%) were purchased from Fluorochem. N$_\alpha$-Boc-L-arginine (98%) and N$_\alpha$-Boc-L-lysine (97%) were purchased from Alfa Aesar. Cyclic (RGDFK) pentapeptide (cyclo(RGDFK)) was purchased from MedChem Express. Monomer and trimer of peptide nucleic acid (PNA-M and PNA-T) were synthesized by Sabrina Gaidies, MSc. in collaboration with Institute of Polymer Chemistry, Johannes Kepler University Linz, Austria.

Carboxylic acid-based capping agents:

Glacial acetic acid (AcA, 99–100%) was purchased from J. T. Baker. Trifluoroacetic acid (TriflacA, 99.5+%) was purchased from Alfa Aesar. Propionic acid (PropA, > 99.5%) was provided by Sigma Aldrich. Hexanoic acid (98%) and n-Octanoic acid (OctA, > 98%) were purchased from TCI. Oleic acid (min. 70%) was purchased from Lachner. Adamantanecarboxylic acid (99.6%) was obtained from Provisco.

Solvents:

N,N-dimethylformamide (DMF), dimethyl sulfoxide (DMSO), xylene (a mixture of isomers), acetone, diethylether, cyclohexane, chlorobenzene, chloroform and toluene were of reagent grade, n-hexane and acetonitrile were of HPLC grade, all provided from VWR. 1-Octadecene (90%) and γ-butyrolactone (GBL, reagent plus >99%) were provided by Sigma Aldrich. Anhydrous DMF was purchased from Sigma Aldrich.

6.2 Synthesis of nanoparticles and their processing

Prior to a preparation of perovskite nanoparticles (PNP), a precursor solution was prepared by mixing $PbBr_2$, MABr, amino-capping and carboxylic capping agents in molar ratios of 1:1.1:0.8:9.5 at ambient conditions according to the literature [101]. The precursor chemicals were dissolved in DMF which acts as a coordinating solvent if not stated otherwise. The concentrations of precursor chemicals were adjusted to 0.027, 0.030, 0.258 and 0.22 $mol \cdot dm^{-3}$ for $PbBr_2$, MABr, amino-based and carboxylic acid-based capping agents, respectively. The as prepared precursor solution was left to be stirred overnight at ambient conditions in order to let all the chemicals to be dissolved and the complex formation to occur.

The PNP colloidal solutions were prepared by the ligand-assisted precipitation technique as firstly introduced by F. Zhang *et al.* [7] with a slight modification. The precursor solution was precipitated in toluene (or in a different precipitation medium) at 3–4 °C in volume ratio 0.002 at ambient conditions. The formation of colloidal solution was immediately detected by changing colour from colourless to bright green and strong photoluminescence was observed under UV irradiation. The colloidal solutions were used for further experiments as prepared if not stated otherwise. If needed, purification steps were performed by centrifuging (5000 rpm/10 min) the crude colloidal solutions. The solid material was consecutively redispersed in the defined amount of the corresponding solvent.

Samples with controlled amount of water in the precursor solutions (section 7.3) were prepared according to the same procedure with a slight modification. The precursor solutions were prepared and in a glove box using anhydrous chemicals ($PbBr_2$ and MABr opened and handled only in the glove box and anhydrous DMF) to avoid any moisture contamination. Also, the precursor solutions were stored in the glove box for one week to let the complex formation occur. The precipitation was performed at ambient conditions.

Films were prepared by centrifugal casting onto desired substrates. Desired substrates (glass slides) were cut to 1×1 cm size and washed in a sonication bath successively (in a cleaning bath Hellmanex ® III), using distilled water for two times, in acetone and finally in isopropanol. The substrates were dried with compressed air and kept for the use. Centrifugal casting was performed according to the literature [101]. The colloidal solution was prepared in a centrifugation tube by precipitating the corresponding precursor solution in toluene in volume ratio 0.002. The desired glass substrate was placed on the bottom of the tube followed by centrifugation (5000 rpm/10 min). The supernatant was carefully discharged, and as formed

film was washed by addition of toluene (approx. 3 ml). The liquid was then discharged and the substrate with the film was dried either at ambient conditions or in a toluene atmosphere. Films were stored in a Petri dish in order to avoid any dust contamination at ambient conditions.

Solid samples for powder XRD were prepared by collecting the material after centrifugation of the colloidal solution (5000 rpm/10 min) and consecutive drying of the solid material at ambient conditions.

6.3 Characterization methods

6.3.1 UV-Vis spectroscopy

UV-Vis spectroscopy was carried out with a Lambda 1050 UV/Vis/NIR spectrometer (PerkinElmer). Absorption spectra of colloidal solutions were measured in quartz cuvettes (1×1 cm) and of thin films were measured on (1×1 cm) glass substrates in the range of 300 to 700 nm.

Band gaps were evaluated by calculating a Tauc plot from the absorption spectra according to the following equation:

$$(\alpha h v)^{1/n} = A\big(h v - E_g\big),\tag{5}$$

where α is the absorption coefficient, h is Plank´s constant, v is the photon frequency, E_g is the bandgap and A is the constant of proportionality. The exponent $1/n$ denotes the nature of the transition, direct allowed transition is considered for perovskite materials, hence, $n = 1/2$ [18] and [145].

6.3.2 Photoluminescence spectroscopy

Photoluminescent (PL) spectra were measured on a QuantaMaster 40 from Photon Technology International. Emission spectra of colloidal solutions were measured in 3 ml quartz cuvettes (1×1 cm) at excitation wavelength of 405 nm. The films on (1×1 cm) glass substrates were also exposed to the 405 nm excitation wavelength at 50° angle.

The PLQY of colloidal PNP suspensions and centrifugal casted films (discussed in sections 7.1, 7.3 and 7.5) were measured using Hamamatsu C9920-03, absolute quantum yield spectrometer equipped with Shamrock SR-303i monochromator and Andor iDus SiCCD detector. For all PLQY measurements, an excitation wavelength of 405 nm was chosen.

PLQY measurements of colloidal solutions of PNP stabilized by amino acids and cyclopeptide discussed in chapter 7.2 and 7.4, respectively, were performed via "direct

excitation" method also used by S. Wang *et al.* [104]. The absolute PLQY (η) was determined as ratio between the number of emitted photons and the number of absorbed ones according to the equation

$$\eta = \frac{E_B}{S_A - S_B},\tag{6}$$

where E_B is the area under the curve in the emission part of the spectra and S_A and S_B are excitation areas of the sample and pure solvent, respectively. The measurement was performed in the integrating sphere in a fluorometer (QuantaMaster 40 from Photon Technology International) with an excitation wavelength of 405 nm in a 3 ml quartz cuvette.

In both cases, signals of pure toluene and empty integrating spheres were detected as a blank measurement for the determination of PLQY of colloidal solutions and thin films, respectively.

For the temperature dependent optical measurements, PNP thin films were placed in QuantumDesign DynaCool PPMS, COHERENT OBIS 405 excitation laser beam was supplied with fiber optics. The laser power was set accordingly. The setup was equipped with a Shamrock SR-303i monochromator and Andor iStar DH320T-18U-73 charge coupled device camera.

6.3.3   Fourier-transform infrared spectroscopy

Fourier-transform infrared (FTIR) spectroscopy was used to evaluate the composition of nanoparticles and to determine the ligands presence. It was also employed to study the complex formation in the precursor solutions [90], [104] and [128].

Here, FTIR spectra of precursor solutions and PNP were recorded on a Perkin-Elmer Spectrum 100. The precursor solutions were measured by using an attenuated total reflectance (ATR) technique at ambient conditions [90]. For the PNP spectra measurement, the PNP were collected by centrifuging the colloidal solutions (5000 rpm/10 min) and as obtained solid material was put onto the ATR crystal.

6.3.4   TEM

Transmission electron microscopy (TEM) images were obtained with a Jeol JEM-2200 microscope using Holey Carbon film 300 Mesh copper grids. The grids were treated by UV irradiation for 30 minutes before the sample deposition. Colloidal solution was dropped onto the grid and it was dried overnight. All sample grids were treated for 5 min in a Jeol EC-52000IC Ion cleaner before the TEM measurement. Fast Fourier Transform (FFT) images were processed by Image J software.

High resolution transmission electron microscopy (HRTEM) images and Energy Dispersive X-ray spectroscopy (EDS) elemental mapping were obtained with the Titan microscope (from FEI) using Holey Carbon film 300 Mesh copper grids. This measurement was performed in cooperation with the Regional Centre of Advanced Technologies and Materials (RCPTM) in Olomouc, Czech Republic.

6.3.5 Atomic force microscopy

To characterize the surface morphology of the films, atomic force microscopy (AFM) pictures were taken by the Bruker Dimension Icon ambient microscope in tapping mode. The NCS15/ALBS tip was purchased from MikroMasch.

6.3.6 Profilometer

The thickness of the layers was determined by performing measurements on a Dektak XT mechanical profilometer (Bruker).

6.3.7 Powder X-ray diffraction

Powder X-ray diffraction (XRD) measurements were performed on an Empyrean (PANalytical) diffractometer using Cu Kα (1.540598 Å) radiation. The tube current was of 30 mA and voltage was of 40 kV. The spectra were taken with a step size $0.013°2\theta$ with time per step of 96 s.

6.3.8 X-ray photoelectron spectroscopy

X-ray photoelectron spectroscopy (XPS) sputter depth profiles were performed using a Thetaprobe XPS system (Thermo Scientific, UK), which was controlled and operated by the Avantage software package from the system manufacturer. The device was equipped with a monochromated Al K_α X-Ray source (hv = 1486.6 eV) and a dual flood gun for neutralizing the surface charges. The X-ray spot on the sample surface exhibited a diameter of 400 μm. The sputtering was performed by using an Ar^+ ion gun. The survey spectra were recorded with 200 eV of pass energy and with binding energy step of 1 eV, while for high resolution spectra the pass energy of 20 eV and step of 0.05 eV were taken. The films for XPS were prepared by centrifugal casting of the colloidal solutions onto glass substrates (1×1 cm), as described above in 6.2. The prepared films were dried and stored in a glove box before the measurement to avoid any contamination.

7   Results and discussion

Here, the results of the experiments are presented. The results are presented in following sections, results from each section were published:

1. A. Jancik Prochazkova *et al.* Scientific Reports, under revision [147]: Preparation of PNP by the ligand-assisted precipitation method and its optimization. Here, PNP were stabilized by $AdNH_2$. Parameters influencing resulting optical properties of the colloidal solutions such as precipitation medium, precipitation temperature, precursor chemicals ratio and the choice of carboxylic acid capping agents were evaluated. In addition, colloidal stability and the stability of precursor solutions was tested.

2. A. Jancik Prochazkova *et al.* ACS Applied Nano Materials, 2019 [148]: Stabilization of PNP by bio-originated capping agents (L-Lysine, L-Arginine). As a proof of concept, basic amino acids (lysine and arginine) were tested for PNP stabilization by their side chains providing α-amino and carboxylic acid groups available for further modifications.

3. A. Jancik Prochazkova *et al.* ACS Applied Nano Materials, 2020 [149]: Study of the influence of water on PNP formation. It was found out that water molecules have a crucial effect on optical properties of PNP when a hygroscopic capping agent (i.e. boc-Lysine) is participating in the nanoparticles' formation.

4. A. Jancik Prochazkova *et al.* Scientific Reports, 2019 [150]: Stabilization of PNP by cyclopeptide. Here, a cyclic pentapeptide (RGDFK) possessing lysine and arginine moieties in the structure was employed for PNP stabilization.

5. A. Jancik Prochazkova *et al.* Materials Today Chemistry, 2020 [151]: Stabilization of PNP by peptide nucleic acids (PNA). Taking into account that biomolecules, such as peptides and DNA, are sensitive to their environment (pH, temperature) and they are badly soluble in nonpolar solvents, a possibility of stabilizing PNP by peptide nucleic acids was tested.

7.1 Optimization of the ligand-assisted precipitation technique to prepare PNPs

Methylammonium lead bromide perovskite nanoparticles (PNP) are easy to be prepared by the ligand-assisted precipitation technique which was firstly described by F. Zhang *et al.* [7]. This versatile and low-cost synthetic approach is performed at room temperature and does not require any special apparatus. Moreover, as prepared colloidal solutions can be further directly processed into films, for example by spin-coating [135], centrifugal casting [101] or inkjet printing [133]. There are several parameters that need to be controlled during the preparation in order to obtain PNP of desired optical properties with a high reproducibility. The parameters influencing the resulting properties are the choice of the capping agents [101], chosen precipitation media [87], temperature during the precipitation [146] and the ratios of the precursor chemicals [152] among others.

Here, adamantyl-1-amine (AdNH$_2$) was chosen as the amino-based capping agent for MAPbBr$_3$ nanoparticles preparation. AdNH$_2$ was previously reported as a good capping agent providing high reproducibility and good optical properties of the resulting colloidal solutions and films [101]. All above mentioned parameters influencing the morphology and optical properties of PNP were controlled during the synthesis providing a comprehensive optimization study of the ligand-assisted precipitation technique for PNP preparation. The results from this section are a part of the publication by A. Jancik Prochazkova *et al.* [147].

7.1.1 Influence of the solvent for the precursor solution preparation

Perovskite materials can be dissolved in polar solvents containing carbonyl groups which are able to coordinate with lead halides. Nevertheless, the strength of the coordination of the solvent to the Pb^{2+} centrum of the lead halide precursor must be evaluated together with the solubility of the perovskite precursors according to the desired processing of the precursor solution. For example, iodide-based perovskite precursor solution for single crystal preparation via inverse temperature crystallization (ITC) is usually prepared in γ-butyrolactone (GBL). On the other hand, *N,N*-dimethylformamide (DMF) or dimethyl sulfoxide (DMSO) are more suitable for thin film processing because of stalling the crystallization which leads to the formation of smoother films [76] and [153].

Here, precursor solutions containing 0.027, 0.030, 0.022 and 0.26 mol·dm^{-3} of PbBr$_2$, MABr, AdNH$_2$ and HeA (keeping the molar ratio 1:1.1:0.8:9.5), respectively, were prepared in DMSO, DMF and GBL. Additionally, acetonitrile (ACN) and water were tested. Acetonitrile was already reported as an additive into iodide- and cation-anion-mixed perovskite precursor

solutions to promote the formation of Lewis acid-base pairs of PbI_2-ACN, and thus, to improve the crystallization [154]. Similarly, addition of water into the precursor solution has a positive effect on the growth of perovskite crystals [155].

As expected, only samples prepared in DMSO and DMF formed clear solutions pointing out to a good solubility of all precursor chemicals. On the other hand, acetonitrile, water and GBL did not fully dissolve the precursor chemicals. Nevertheless, they might be considered to be used as additives into precursor solutions to alternatively improve the complex formation and enhance subsequent crystal growth as mentioned above. For example, a certain amount of water in the precursor solution was found out to tune optical properties of PNPs when used with certain capping agents (see further in section 7.3).

Colloidal solutions were prepared by precipitating DMSO- and DMF-based precursor solutions in toluene at 3–4 °C. The volume ratio of the precursor solution to toluene was adjusted to 0.002. In both cases, green colloidal solutions with strong photoluminescence under UV irradiation was observed (Figure 11a). UV-Vis and PL spectroscopy techniques were applied in order to study the optical properties of the colloidal solutions. As summarized in Table 1 and shown in Figure 11b, the emission maxima of the colloidal solutions prepared from DMF- and DMSO-based precursor solutions were 522 and 530 nm, respectively. Interestingly, when the colloidal solution was prepared from the DMSO-based precursor solution, PLQY was significantly lower; it was only of 2%. Whereas the colloidal solution prepared from the DMF-based precursor solution possessed PLQY of 43%. The red shift of the emission maximum and the decrease in PLQY of the colloidal solutions prepared from the DMSO-based precursor solution was attributed to the retarded crystallization process during the precipitation. DMSO is considered to have a strong binding to the lead precursor [156] and thus, the capping agents cannot efficiently replace the solvent to control the crystal growth by passivating the nanoparticles surface.

Table 1: Optical properties of colloidal solutions prepared from DMF- and DMSO-based precursor solutions.

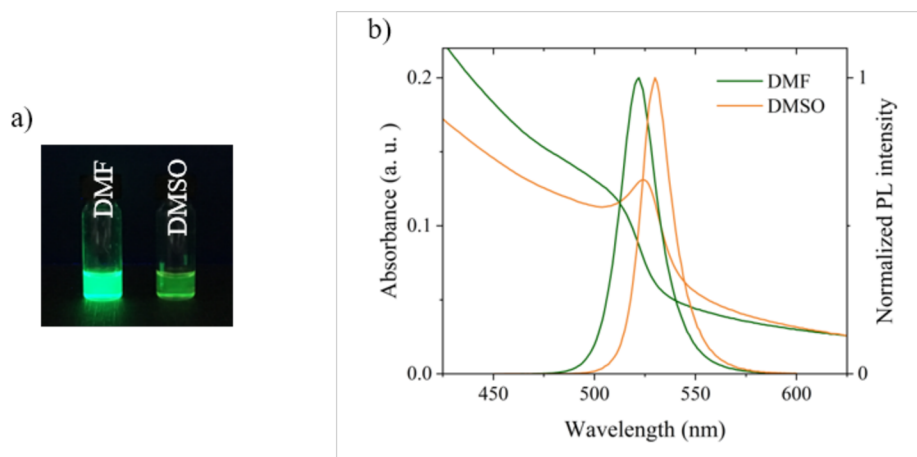| Coordinating solvent	Emission maximum (nm)	FWHM (nm)	PLQY (%)	Band gap (eV)
DMF	522	22	43	2.33
DMSO	530	18	2	2.30

Figure 11: Colloidal solutions prepared from DMF- and DMSO-based precursor solutions, a) a photo of the colloidal solutions under UV irradiation (366 nm) and b) optical properties of the corresponding colloidal solutions.

As a result, DMF-based precursor solutions for $MAPbBr_3$ PNP preparation were prepared for further experiments. Simultaneously, the reproducibility of the PNP synthesis procedure was tested by preparing different DMF-based precursor solutions independently. Colloidal solutions were obtained with an emission maximum of 521 ± 2 nm, a PLQY of $48\pm8\%$ and a band gap in the range 2.32–2.34 eV. With these results a good reproducibility of the PNP synthesis procedure can be claimed.

7.1.2 Perovskite-like structure determination by powder X-ray diffraction

In order to confirm the perovskite-like structure of the material prepared above, powder X-ray diffraction (XRD) was performed. PNP were collected by centrifugation of the colloidal solutions and as obtained material was dried at ambient conditions. The perovskite crystalline structure was confirmed by comparing diffractogram of PNP with diffraction patterns of $MAPbBr_3$ single crystal [76], see in Figure 12. Peaks positioned at 14.90°, 21.14°, 26.02°, 30.07°, 33.72°, 37.08°, 43.05°, 45.83° and 48.42°2θ corresponded to the reflections from the planes (001), (011), (111), (002), (021), (211), (220), (300) and (310), respectively, confirming the cubic unit cell structure [76]. The broadening of the diffraction peaks observed in the PNP spectrum resulted from the small crystal volume of the individual nanoparticles [157].
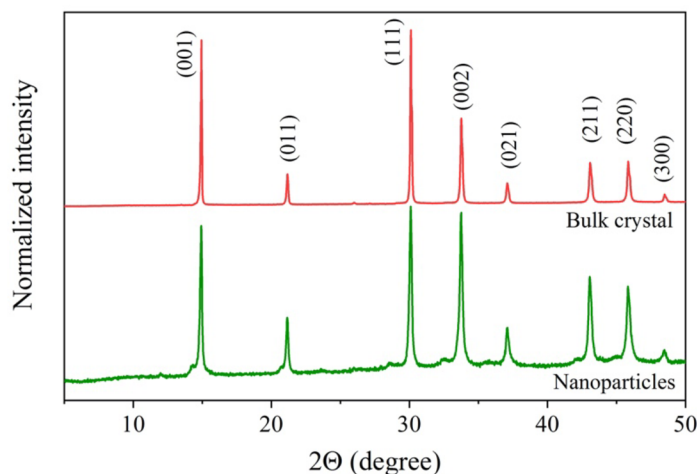
52

Figure 12: Powder XRD spectrum of PNP with comparison to the bulk MAPbBr₃ perovskite crystal

7.1.3 Purification steps

The purification consists in centrifuging the crude colloidal solution and subsequent redispersing the solid material in toluene or another suitable solvent. In general, the aim of the purification is the elimination of unreacted precursor chemicals in the colloidal solutions. Simultaneously, the size distribution of nanoparticles can be narrowed with removal of too large or too small nanoparticles according to the approach of the purification [158]. Here, the purification steps were applied to primarily remove the unreacted chemicals from the colloidal solutions. An influence of the purification on optical properties of the colloidal solutions and on individual nanoparticles morphology was studied. Hence, a colloidal solution was prepared, and consecutively washed three times. Its optical properties were determined after every step, see Table 2.

Table 2: Optical properties of crude and washed colloidal solutions

Washing step	Emission maximum (nm)	FWHM (nm)	PLQY (%)
Crude	522	23	54
Washed 1x	522	23	43
Washed 2x	523	23	35
Washed 3x	523	23	30

As expected, PLQY was decreasing with every washing procedure, it dropped from an initial 54% to 30% after the third washing step. This could be attributed to the removal of the ligands which were electrostatically bound to the surface of PNP. Because of leakage of the capping agents from the organic shell, non-radiative recombination can occur, and therefore, PLQY decreases [158]. Simultaneously, thinning the organic shell might support agglomeration or additional crystal growth [159]. This assumption was supported by a slight red shift of emission spectra from 522 nm to 523 nm in the crude and three times washed colloidal solution, respectively. To provide reliability data, this experiment was performed several times. A strong drop of PLQY to 40–60% of the original value was always observed after three washing steps. Though, no significant changes in emission maxima were detected.

In order to prove further the latter statement, the morphology of PNP from the crude and three times washed colloidal solutions was studied. In some cases, dynamic-light scattering (DLS) technique can be applied to evaluate the size of particles in colloidal solutions [160]. Nevertheless, the individual nanoparticles have to be considered spherical and they should not aggregate, because only aggregates would be detected in that case. Therefore, transmission electron microscopy (TEM) was employed to evaluate the size and the shape of individual nanoparticles and aggregates directly. It is worth noting that nanoparticles degradation under electron beam exposure was described in some cases [86] and [161]. J. Sichert and co-workers. [162] proposed that a degradation process of perovskite nano-structure material can take place and a mixture of $PbBr_2$, pure Pb and potentially other phases can be created. Indeed, a degradation of the sample was observed at the spots which were exposed to the electron beam for a longer period.

The samples were prepared by dropping the corresponding colloidal solution onto a copper grid, the sample was consecutively dried at ambient conditions. It was observed that PNP tended to form agglomerates in both crude (Figure 13a) and in three times washed colloidal solutions (Figure 13b). The individual PNP were very easy to follow in case of the sample prepared from the crude colloidal solution. On the other hand, PNP were overlapping in the three times washed colloidal solutions. In both cases, an amorphous phase surrounding the nanoparticles was present, suggesting that not all free capping agents might have been removed from the colloidal solution after the washing procedure [92].

As expected, the morphology of the nanoparticles did not change during the washing procedure, as seen by comparing an individual nanoparticle from the crude colloidal solution (Figure 13c) and from the three times washed colloidal solution (Figure 13d). Individual PNP

were spherical and crystalline with an average size around 10 nm in both samples. However, after a thorough calculation of an average size of the nanoparticles, the typical diameter increased from initial 8.5±1.8 nm to 9.3±2.0 nm after the third washing step. This can support the aforementioned assumptions about the thinning of the organic shell during the washing procedure.
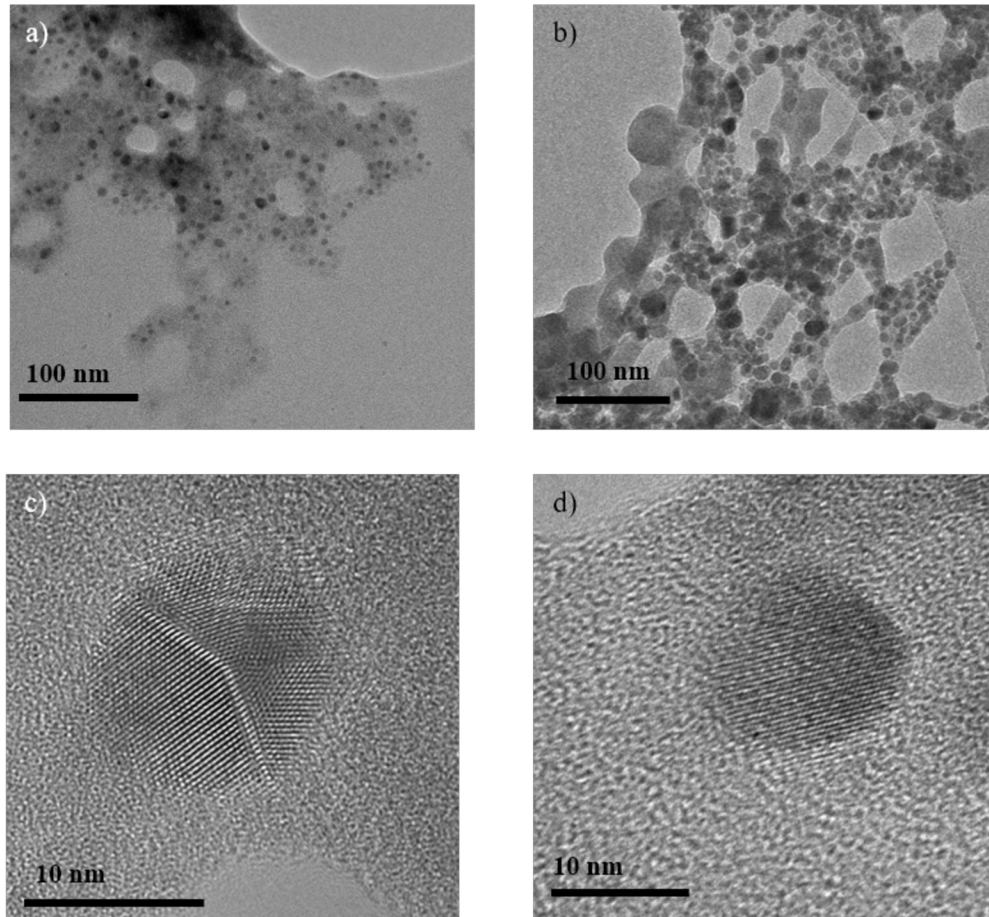

Figure 13: TEM images of PNP, a) aggregates formed in the crude sample and b) in three times washed sample, c) individual nanoparticle from the crude sample and d) from three times washed sample

It is worth to point out that the degradation of PNP during their purification is a common feature [158]. J. De Roo *et al.* [92] suggested that oleylamine as an amino-based capping agent possesses a highly dynamic nature of binding to the surface of nanoparticles (as demonstrated in Figure 9). To increase the PLQY after the purification procedure, they added more oleylamine to the dispersion. An increase in PLQY from 40 to 83% was observed. Another possibility of avoiding the removal of the capping agents is an engagement of stronger capping agents. For example, already described zwitterionic-based capping agents [93] or octyl phosphonic acid-type capping agents [159] can bind tighter to the surface of nanoparticles providing them with improved optical and colloidal stability.

7.1.4 Concentration dependency

The concentration of the analyte needs to be tuned for the optical spectroscopy techniques in order to obtain a sample with an appropriate optical density [163]. Thus, the precursor solution was precipitated in toluene in different volume ratios and the as prepared samples were characterized by optical spectroscopy techniques. Five samples were prepared by precipitating the precursor solution in toluene in volume ratios 0.001, 0.002, 0.003, 0.005 and 0.01 and their appearance under UV irradiation is shown in Figure 14c. Absorption spectra (Figure 14a), PL spectra (Figure 14b) and the PLQYs were determined (see summarized in Table 3).
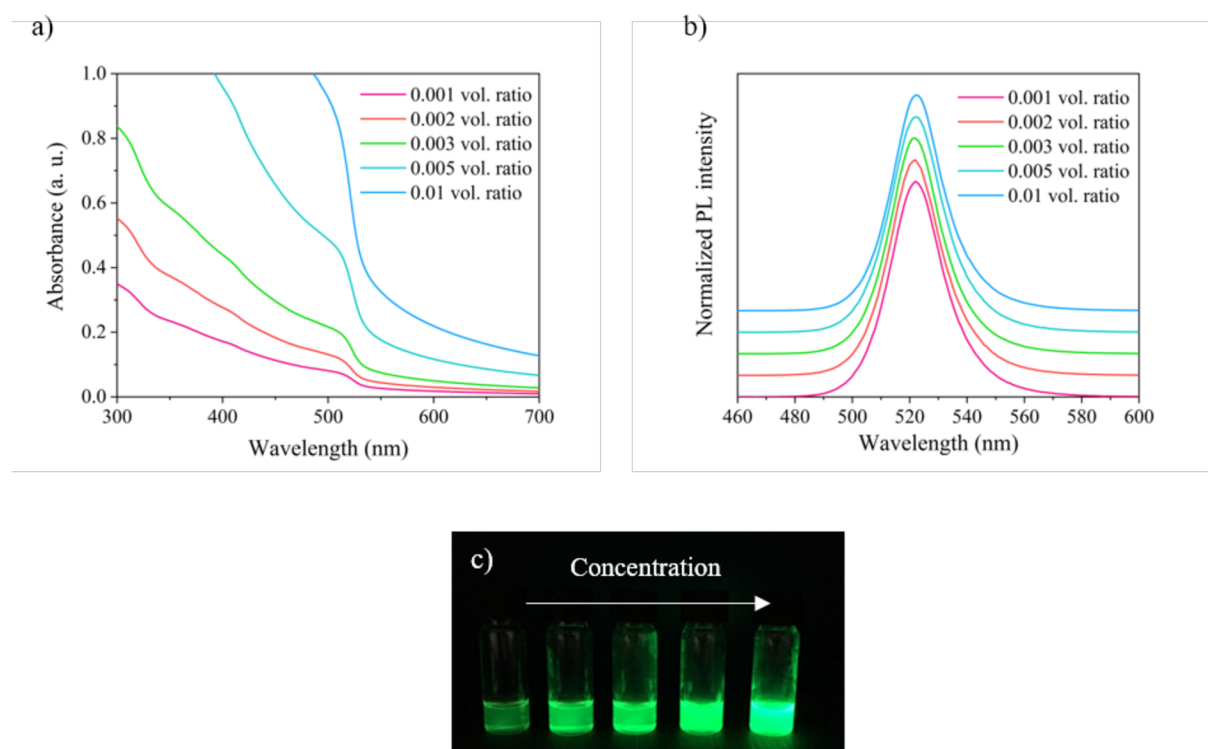

Figure 14: Optical properties of colloidal solutions prepared by precipitating precursor solution in toluene in different volume ratios, a) absorption spectra, b) emission spectra and c) image of corresponding samples under UV irradiation (366 nm)

The data summarized in Table 3 show that the emission maxima and the corresponding band gaps did not change with different volume ratios between the precursor solution and toluene. This could point out that PNP of the same size and shape are formed in all samples. Nevertheless, PLQYs differ with changing the volume ratio between the precursor solution and toluene during the preparation. After the correlation of the PLQYs with the absorption spectra (Figure 14a), it could be assumed that the optical density of the colloidal solutions prepared by precipitating the precursor solution in toluene in volume ratios above 0.005 is too high at excitation wavelength of 405 nm. Therefore, the determination of PLQYs might be inaccurate

mainly because of auto-absorption effects [163]. In order to have comparable data with already presented samples, the volume ratio of precursor solution to toluene was kept at 0.002 in the next experiments.

Table 3: Comparison of optical properties of colloidal solutions prepared by precipitating precursor solution in toluene in different volume ratios.

Volume ratio of precursor solution in toluene	Emission maximum (nm)	FWHM (nm)	PLQY (%)	Band gap (eV)
0.001	521	22	41	2.33
0.002	520	22	43	2.34
0.003	520	21	41	2.34
0.005	520	22	45	2.33
0.01	521	21	62	2.33

7.1.5 Temperature dependency

It was already proposed by H. Huang *et al.* [146] that precipitation temperature has a significant effect on the resulting optical properties of PNP colloidal solutions. Hence, precipitation temperature was varied from −5 to 80 °C and the resulting optical properties of the colloidal solutions were evaluated. Considering PLQY, the best precipitation temperature for the PNP preparation was 3 °C, the PLQY was 51% corresponding to an emission maximum of 521 nm. In general, the PLQY dropped significantly (Figure 15b) and emission maxima (Figure 15a) shifted to higher wavelengths with increasing temperature. For example, applying a temperature of 80 °C during the precipitation caused a drop of PLQY to 4% and a shift of emission maximum to 528 nm. The summary of the optical properties is listed in Table 4.

It can be assumed that the perovskite lattice grows too fast at temperatures higher than 60 °C and the surface passivation by the capping agents is not efficient enough to control the nanoparticles growth [75]. The insufficient surface passivation is expected to cause the red shift in emission maxima and a significant lowering of the PLQY, which were both observed. On the other hand, when the precipitation is performed at too low temperature (−5 °C), the solubility of the precursors is supposed to get worse and the surface passivation is not sufficient enough which again leads to the drop of PLQY as observed.
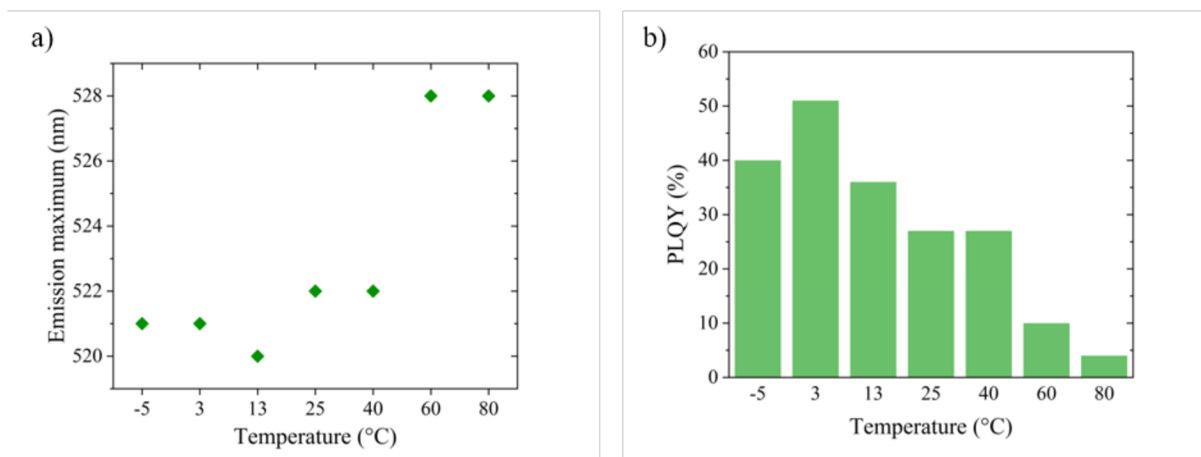
Figure 15: Varying temperature during the ligand-assisted precipitation, a) typical changes in emission maxima and b) in PLQY according to temperature

Table 4: Comparison of optical properties of colloidal solutions prepared at different temperatures

Temperature (°C)	Emission maximum (nm)	FWHM (nm)	PLQY (%)	Band gap (eV)
−5	521 ± 2	22 ± 1	36 ± 6	2.32 ± 1
3	521 ± 2	22 ± 1	48 ± 7	2.33 ± 1
13	520 ± 2	22 ± 1	34 ± 6	2.35 ± 1
25	523 ± 2	23 ± 1	20 ± 5	2.34 ± 1
40	523 ± 2	22 ± 1	20 ± 5	2.33 ± 1
60	528 ± 2	19 ± 1	7 ± 2	2.30 ± 1
80	528 ± 2	21 ± 1	3 ± 2	2.29 ± 1

7.1.6 Precipitation media

Different precipitation media were tested in further steps in order to prove the versatility of the ligand-assisted precipitation method. The possibility of using different solvent systems is necessary from the application point of view. Hence, chlorobenzene, n-hexane, cyclohexane, 1-octadecene, acetonitrile, tetrahydrofuran, diethylether, chloroform, xylene, acetone and toluene were tested as precipitation media for PNP preparation during the ligand-assisted precipitation technique. Remarkably, chlorobenzene, chloroform, diethylether, toluene and xylene supported the formation of PNP, which was detected by colour change during the precipitation (Figure 16). Chlorobenzene, chloroform, toluene and xylene are generally non-polar solvents which can act as antisolvents for perovskite precursors [7]. On the other hand, diethylether is an aprotic polar solvent, nevertheless, it is also known to act as an antisolvent

for perovskite materials [164]. Strong non-polar solvents such as n-hexane, cyclohexane and 1-octadecene were not supporting the PNP formation, neither did highly polar solvents such as acetonitrile, acetone and tetrahydrofuran. It is worth noting that polar solvents such as acetonitrile and acetone are usually employed as additives to control the perovskite structure crystallization [154] and [165].

Regarding the optical properties, prepared colloidal solutions exhibited green emission under UV irradiation, as shown in Figure 16. Determined optical properties are collected in Table 5 and typical UV-Vis spectra alongside PL spectra are presented in Figure 17a–e.
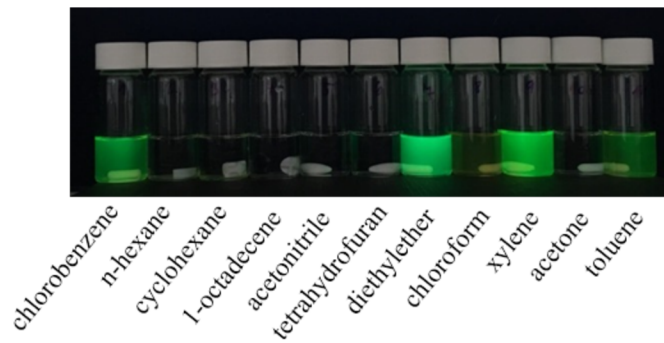

Figure 16: A photo of colloidal solutions prepared in different precipitation media, under UV irradiation (366 nm)

Table 5: Optical properties of colloidal solutions prepared in different precipitation media

Solvent	Emission maximum (nm)	FWHM (nm)	PLQY (%)	Band gap (eV)
Diethylether	518 ± 3	23 ± 1	33 ± 6	2.37 ± 1
Chlorobenzene	519 ± 2	20 ± 1	34 ± 5	2.36 ± 1
Chloroform	509 ± 2	23 ± 1	>1	2.37 ± 1
Xylene	520 ± 2	20 ± 1	34 ± 5	2.33 ± 1
Toluene	521 ± 2	22 ± 1	48 ± 7	2.33 ± 1

Interestingly, the most blue-shifted emission maximum of 509 nm was observed in the colloidal solution prepared in chloroform. Here, it could be assumed that chloroform induces a formation of smaller nanoparticles which could point out to the blue shift in emission spectra due to quantum confinement (see further experiments in section 7.2.1). The corresponding PLQY of this solution was significantly reduced when compared to a typical colloidal solution

prepared in toluene, which dropped from ca 48% to less than 1%. The latter observation was attributed to the quenching properties of chloroform, in agreement with literature [166]–[167].
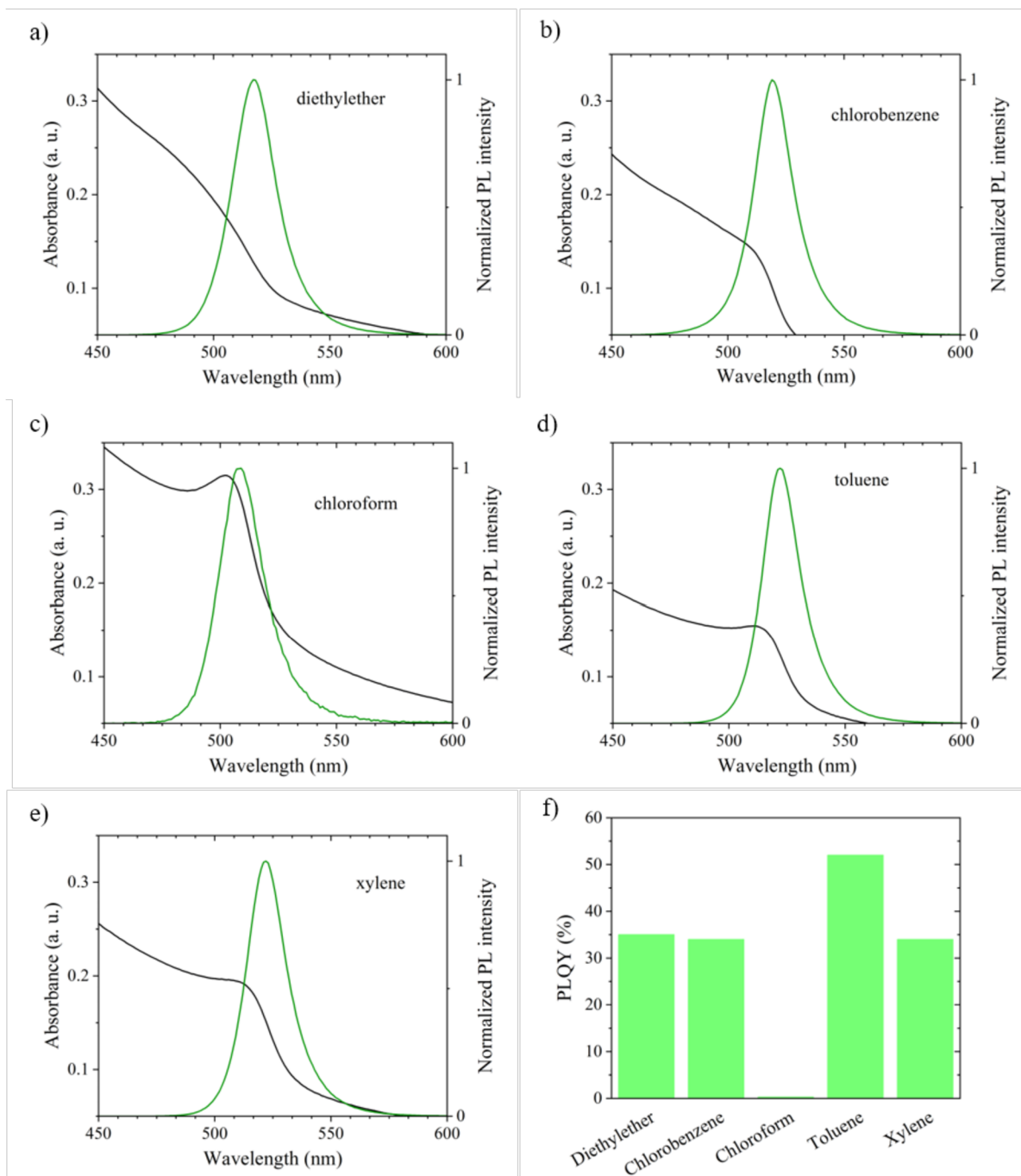
Figure 17: Optical properties of colloidal solutions prepared in different precipitation media – a) diethylether, b) chlorobenzene, c) chloroform, d) toluene and e) xylene and f) their PLQY

With respect to PLQY, toluene gave PLQY of ca 48%, which seems to be the most efficient precipitation medium (as seen in Figure 15). Nevertheless, the possibility of the use of chloroform and chlorobenzene may enhance the applicability of these materials into functional devices. The wide choice of the solvents is crucial for layered systems preparation in order to

avoid damaging already deposited films. Moreover, PNP were also prepared by precipitating precursor solutions directly in polymer solutions [168]. Hence, the precipitation media can be tailored to be able not only to dissolve the desired polymers but also to support the formation of PNP.

7.1.7 Varying the ratios of precursor chemicals

Optical properties were already described to be dependent on the ratio of the precursor chemicals [98]. Thus, the concentration of precursor chemicals in the precursor solutions was varied while keeping the $PbBr_2$ concentration constant (0.027 mol·dm^{-3}), the variations in molar equivalents are comprehensively listed in Table 6.

Initially, $AdNH_2$ ratio was varied from 0.4 to 2.5 mol. eq. with respect to $PbBr_2$ (Figure 18a, b and e). Remarkably, the emission maxima of the corresponding colloidal solutions shifted to lower wavelengths with increasing $AdNH_2$ amount. Simultaneously, the PLQY increased from 8 to 70% with $AdNH_2$ amount up to 1.6 mol. eq. with respect to $PbBr_2$. When 2.5 mol. eq. of $AdNH_2$ with respect to $PbBr_2$ were added into the precursor solution, a significant drop of PLQY to 57% occurred (Table 6), suggesting a possible limit of $AdNH_2$ concentration for the PLQY optimization.

Increasing the concentration of capping agents is known to help control the nanoparticles' growth [92]. An excess of the capping agents helps to efficiently stabilize the PNP and thus, the nanoparticles grow smaller, which could be in agreement with the already discussed blue-shift of emission spectra. The Bohr radius of $MAPbBr_3$ perovskite material was theoretically calculated to be 4.7 nm [169]. Hence, possible quantum confinement effects could explain the optical behaviour of the colloidal solutions. Simultaneously, increasing $AdNH_2$ concentration enhanced the PLQY, as discussed previously. Here, more efficient PNP stabilization can possibly reduce the formation of the defects which results in preferential non-radiative recombinations, as reported in [92] and [98].

Table 6: Optical properties of colloidal solutions where the PNP were prepared with different precursors ratios

AdNH₂ ratio	Emission maximum (nm)	FWHM (nm)	PLQY (%)	Band gap (eV)
2.5	509	32	57	2.46
1.6	508	29	70	2.45
1.2	511	27	67	2.44
1.0	513	26	66	2.44
0.8*	519	26	44	2.33
0.4	522	24	8	2.32

MABr ratio	Emission maximum (nm)	FWHM (nm)	PLQY (%)	Band gap (eV)
1.9	529	20	18	2.27
1.1*	522	21	40	2.33
0.9	519	23	36	2.33

HeA ratio	Emission maximum (nm)	FWHM (nm)	PLQY (%)	Band gap (eV)
19	521	22	53	2.35
9.5*	522	21	40	2.33
4.8	522	21	29	2.33
2.4	523	21	36	2.34

*Standard ratios for the PNP preparation which are described in the experimental section.
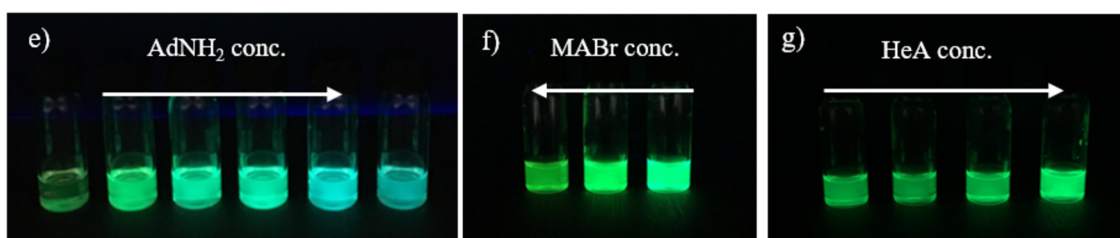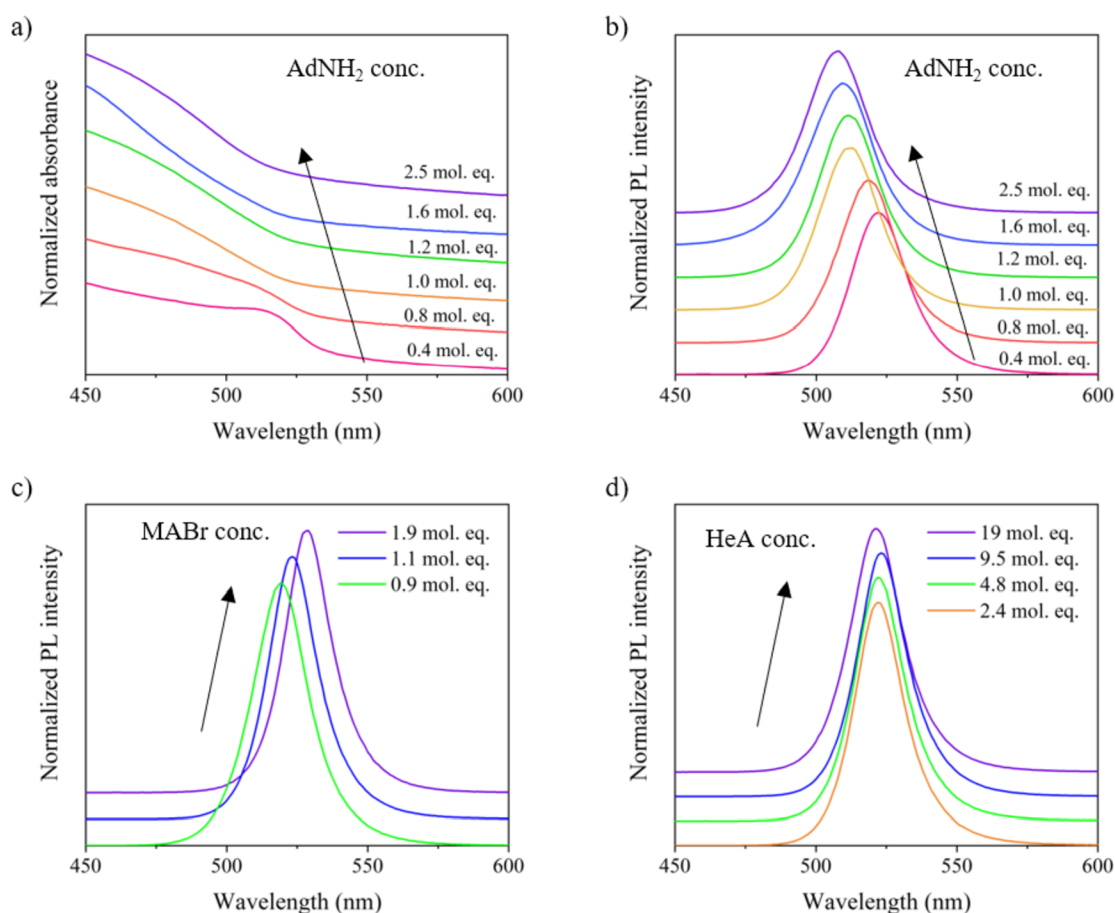
Figure 18: Varying precursor chemicals ratio in precursor solution and the influence on optical properties. a) UV-Vis spectra and b) PL spectra of colloidal solutions prepared from precursor solutions with 0.8, 1.0 and 1.6 molar equivalents of AdNH$_2$ with respect to PbBr$_2$, c) PL spectra when varying MABr and d) HeA concentration in the precursor solutions and e), f), g) photos of the colloidal solutions with different AdNH$_2$, MABr and HeA ratios, respectively (under UV irradiation).

To evaluate the influence of the concentration of the capping agents on the size of the resulting nanoparticles, the samples prepared from precursor solutions with 0.8, 1.0 and 1.6 mol. eq. of AdNH$_2$ with respect to PbBr$_2$ were analysed by TEM (Figure 19). In general, no difference in the PNP morphology was observed with the concentration changes, where all samples contained spherical and highly crystalline nanoparticles. To follow the crystalline structure better, corresponding reciprocal diffraction patterns of the TEM images were obtained by applying Fast Fourier Transformation (FFT). Average sizes of the PNP were 8.5±1.8 nm,

6.2±0.4 nm and 4.5±0.6 nm, respectively. Obviously, the amino-capping agents directly controlled the nanoparticles growth during the ligand-assisted precipitation method of preparation.
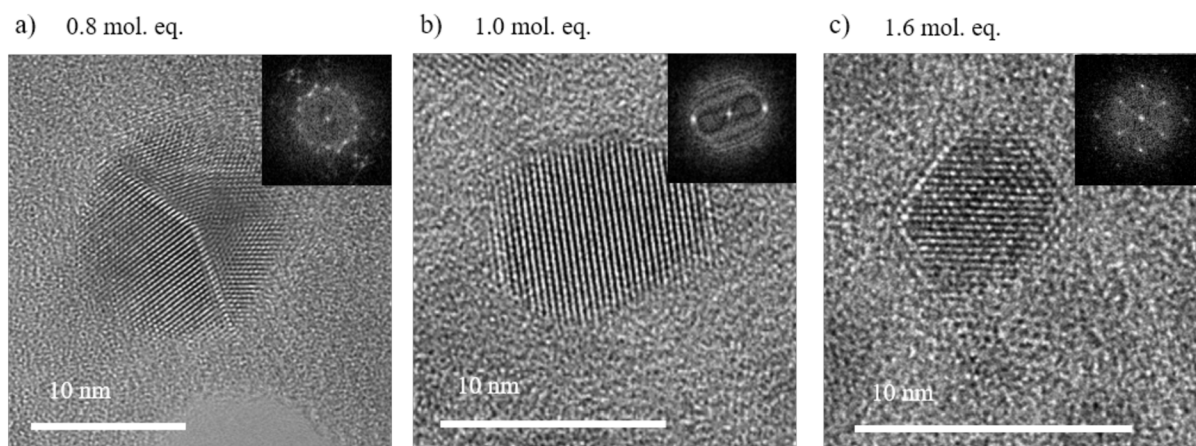

Figure 19: TEM images of PNP containing a) 0.8, b) 1.0 and c) 1.6 mol eq. of AdNH₂ and corresponding FFT images.

As anticipated, the concentration of MABr in the precursor solution had a significant impact on optical properties. It was observed that increasing the MABr amount from 0.9 to 1.9 mol. eq. with respect to $PbBr_2$ yielded to the formation of colloidal solutions with red-shifted emission maxima from the initial 519 nm to 529 nm. This was attributed to an excess of MABr which might have replaced the capping agents preventing the nanoparticles from the additional growth. Therefore, the nanoparticles can grow bigger, as related to their red shift observed in emission maxima. Interestingly, the highest PLQY of 40% was detected when 1.1 mol. eq. of MABr with respect to $PbBr_2$ were added to the precursor solution. Moreover, increasing the MABr concentration up to 1.9 mol. eq. with respect to $PbBr_2$ caused a drop of PLQY to 18% which could also point out to the replacement of the capping agents which prefer the radiative recombination processes.

Finally, the concentration of HeA in the precursor solutions did not exhibit any significant effects on the emission spectra of the resulting colloidal solutions. The emission spectra were only negligibly shifted from 523 to 521 nm while increasing the HeA concentration from 2.4 to 19 mol. eq. with respect to $PbBr_2$. However, the HeA concentration had a considerable effect on PLQY which increased up to 53% when 19 mol. eq. were added with respect to $PbBr_2$ into the precursor solutions. Obviously, increasing amounts of the carboxylic acid-based capping agents helps to stabilize the PNP in the colloidal solutions and to reduce the non-radiative recombinations. On the other hand, additions of such as excesses of the starting material could

64

cause accumulation of the unreacted material causing contamination of the colloidal solutions. The contamination could impede further processing of the colloidal solutions.

In conclusion, it was demonstrated that the concentration of precursor chemicals in the precursor solution has a significant impact on the resulting optical properties, particularly on the PLQYs. Here, the deviation of the PLQY of AdNH$_2$ stabilized PNP (section 7.1.1) presenting almost 15% of the average value can be explained. Considering even tiny deviations in ratios of precursor chemicals in the precursor solution can cause significant changes in the resulting PLQY. Hence, the results presented in Table 6 are collected from a typical experiment without including reliability data. Therefore, it is worth noting that the above-mentioned trends in optical properties were observed among all performed experiments.

7.1.8   Comprehensive characterization of PNP

To fully characterize the prepared PNP and to better understand the ligands binding to the nanoparticles surface, X-ray photoelectron spectroscopy (XPS) and Fourier-transform infrared (FTIR) spectroscopy were employed. The samples for this characterization were prepared by the optimized procedure; the precursor solution was prepared in DMF with the molar ratio of the precursors 1:1.1:0.8:9.5 for PbBr$_2$, MABr, AdNH$_2$ and HeA. The precursor solution was precipitated in toluene in volume ratio 0.002 at 3 °C. For XPS, PNP were centrifugal casted onto a glass substrate and as casted film was carefully washed with toluene and it was consecutively dried at ambient conditions [101]. For the FTIR characterization, the colloidal solution was centrifuged (5000 rpm/10 min) and the solid material settled on the bottom of the centrifugation tube was carefully rinsed with toluene. The solid material was finally collected after being dried at ambient conditions.

XPS provides information about the binding energy of a core-level electron atom present in the sample. The detected binding energy gives details not only about the composition of the sample but also about the environment of individual atoms [170]. Hence, it can be employed to study the PNP composition and to elucidate the binding of capping agents to the perovskite core.

The survey spectrum (Figure 20a) detected all expected elements in the sample of PNP – namely, carbon, nitrogen, lead and bromine pointing out to the perovskite material, and carbon, nitrogen and oxygen signals confirming the presence of capping agents.
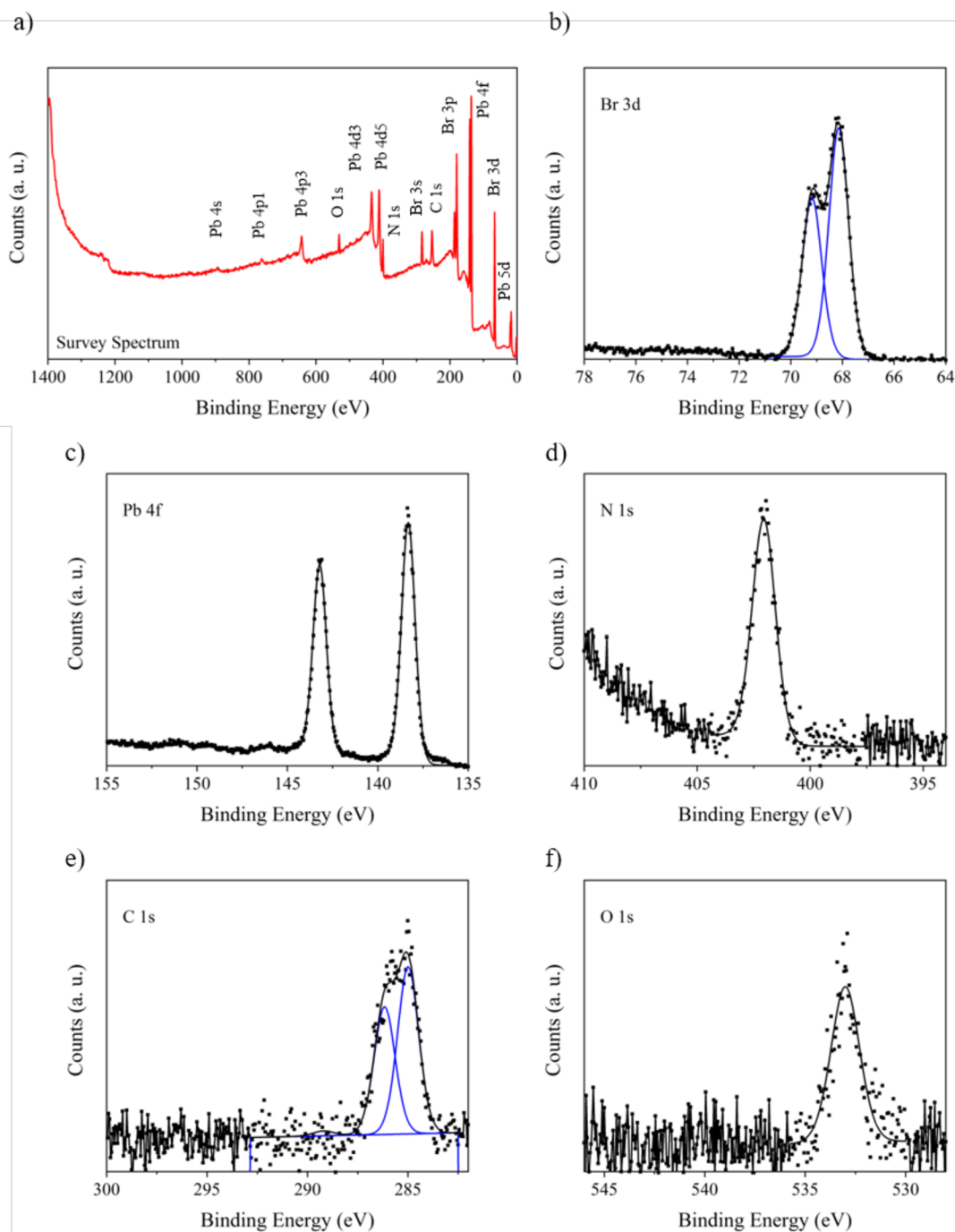
Figure 20: XPS of PNP stabilized by AdNH2 and HeA in amounts of 0.8 and 9.5 mol. eq. with respect to PbBr2

High resolution Pb 4f XPS spectrum showed two characteristic symmetric peaks positioned at 138.3 eV and 143.2 eV, attributed to Pb $4f_{7/2}$ and Pb $4f_{5/2}$, respectively (Figure 20c) [101]. The calculated spin–orbit splitting is 4.9 eV, which is in agreement with previously reported results [152] and [171]. Two peaks were also observed in the Br 3d XPS spectrum, specifically at 68.2 eV and 69.2 eV, pointing out to Br $3d_{5/2}$ and Br $3d_{3/2}$, respectively [172]. The N 1s XPS spectrum revealed one peak with the centrum at 401.8 eV. This peak can be associated to the

methylammonium salt and also to the ammonium salt of AdNH$_2$ [152]. Additionally, the presence of the only peak at 401.8 eV suggests the charged character of the primary ammonium group in AdNH$_2$ molecules. This might point out to the absence of a free primary amine which acts as an impurity because of not being involved in PNP surface stabilization [92]. The C 1s XPS spectrum was deconvoluted into three peaks, the peak at 285.0 eV can be attributed to C–C and C–H bonds of adamantyl-moiety and of the side chain of HeA, next peak at 286.2 eV can be assigned to the C–N bond of the amino groups [152]. Finally, the peak at 289.2 eV can be related to the C–O bond of the carboxylic acid group [173]. Because of the ionic form of the carboxylic acids, only the C–O bond was proven in the spectra due to the delocalization of the negative charge among the carboxylic group [174]. The O 1s XPS spectrum exhibited one peak at 533.0 eV pointing out to the C–O bond of the carboxylic acid, what supports the aforementioned statement about the presence of carboxylate anion of HeA. The quantification of the perovskite components by XPS showed ratios of 2.7 and 1.2 for Br/Pb and N/Pb, respectively, which is in correspondence with previously reported results [101].

FTIR spectroscopy was employed to detect the presence of the capping ligands decorating the surface of the PNP and to compare the spectrum of PNP with the spectrum of the precursor solution (see in Figure 21) [90]. Three main characteristic peaks of MABr were found at 3300–2700 cm^{-1} (broad signal) assigned to the Br-H, at 1000 and 912 cm^{-1} (narrow and medium signals, respectively) assigned to C-H rocking bonds as described in previous reported literature [175] and [176]. The characteristic signals of MABr were detected in both precursor solution and PNP with a slight shift – signals at 3300–2990 and 912 cm^{-1} could correspond to the vibrations of the methylammonium ions in the surrounding of PbBr$_3^{-}$. Simultaneously, interaction between PbBr$_2$ and MABr in the precursor caused a shift of the dominant C=O signal from DMF from 1670 cm^{-1} to a lower wavenumber 1650 cm^{-1} [177].

Bands at 2900 and 2845 cm^{-1} related to –CH$_2$ groups from AdNH$_2$ appear at higher wavenumber in the spectrum of PNP (namely at 2916 and 2857 cm^{-1}, respectively) which can be an indication of nanoparticles surface passivation. Furthermore, the signal at 1595 cm^{-1} from the amine of AdNH$_2$ was shifted to a lower wavenumber 1579 cm^{-1} attributed to the possible coordination with the PbBr$_3^{-}$ from the amino groups [148]. In the precursor, the signals at 2930 and 2855 cm^{-1} were attributed to the alkyl groups and the signal detected at 1705 cm^{-1} was assigned to C=O stretching band from carboxylic acid group of HeA [178].
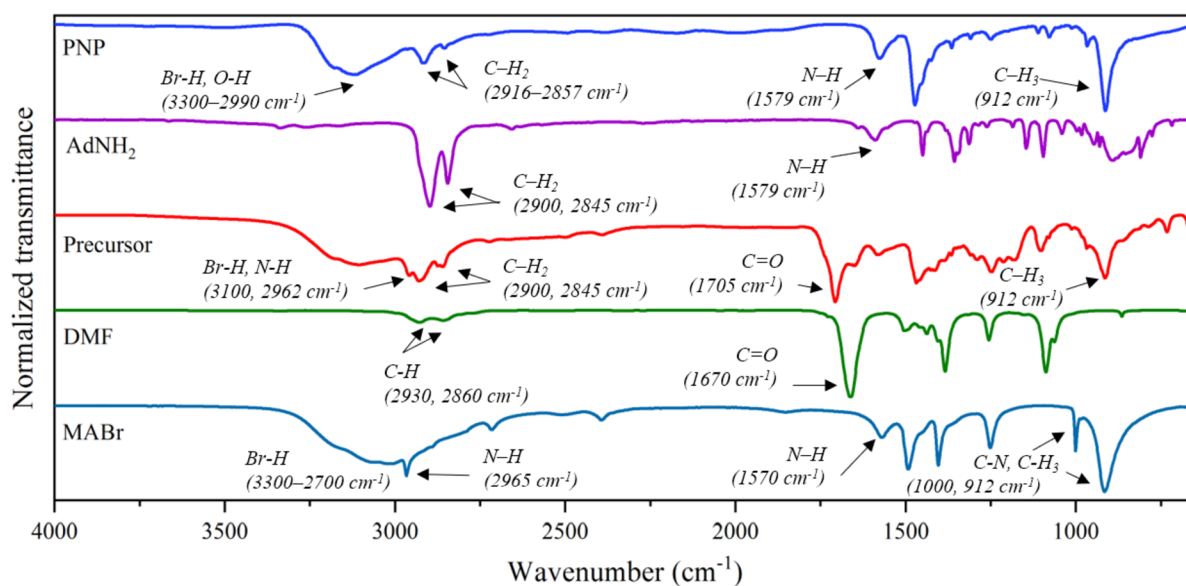
Figure 21: FTIR spectra of precursors of PNP stabilized by AdNH₂ and HeA in amounts of 0.8 and 9.5 mol. eq. with respect to PbBr₂

7.1.9 Testing different carboxylic acids as capping agents

To evaluate the role of the carboxylic acid-based capping agent, different carboxylic acids were selected to stabilize PNP – acetic acid (AcA), trifluoroacetic acid (TriflacA) and propanoic acid (PropA) were selected in order to study short-chain carboxylic acids which act as stronger acids in comparison with already used HeA. Furthermore, n-octanoic acid (OctA), oleic acid (OleicA) and adamantanecarboxylic acid (AdA) were chosen to represent long-chain and bulk-chain carboxylic acids. In addition, a reference sample (noted as ref) without any carboxylic acid addition was prepared for comparison. A fixed ratio of precursors was set to 1:1.1:0.9:9.5 for PbBr₂, MABr, AdNH₂ and carboxylic acid.

All samples containing different carboxylic acid-based capping agents formed colloidal solutions (Figure 23d), and their optical properties are collected in Table 7 and in Figure 23. The emission maxima differed in the range from 520 to 528 nm according to the carboxylic acid. It was observed that the choice of carboxylic acid also had a strong influence on the resulting PLQY which varied from 3 to 58%. From the point of view of PLQY, the best capping agents were PropA and HeA, which is in agreement with already published results [101].
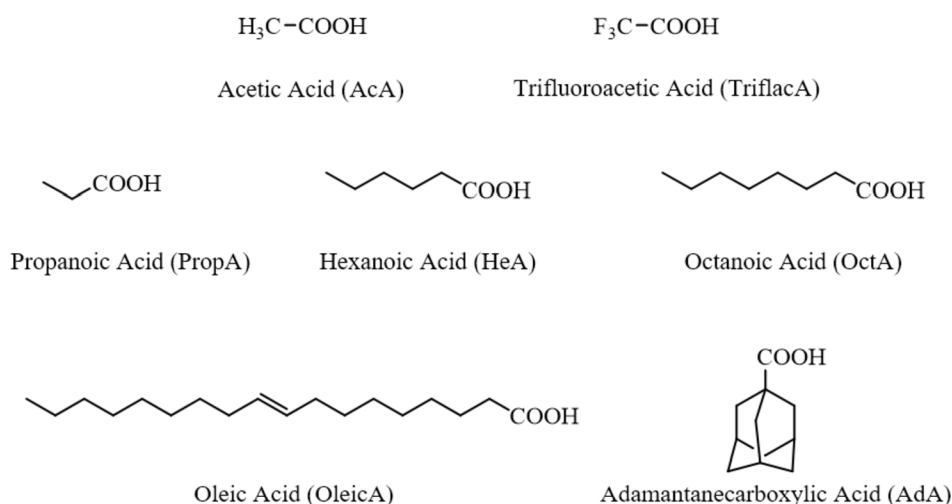
H₃C−COOH

Acetic Acid (AcA)

F₃C−COOH

Trifluoroacetic Acid (TriflacA)

Propanoic Acid (PropA)   Hexanoic Acid (HeA)   Octanoic Acid (OctA)

Oleic Acid (OleicA)   Adamantanecarboxylic Acid (AdA)

Figure 22: Structures of chosen carboxylic acids acting as capping agents for PNP stabilization

Table 7: Comparison of optical properties of PNP colloidal solutions with different capping agents

Carboxylic acid	Emission maximum (nm)	FWHM (nm)	PLQY (%)	Band gap (eV)
AcA	528 ± 2	19 ± 1	42 ± 6	2.30 ± 1
TriflacA	520 ± 2	20 ± 1	3 ± 2	2.33 ± 1
PropA	521 ± 2	25 ± 1	58 ± 7	2.32 ± 1
HeA	521 ± 2	22 ± 1	51 ± 7	2.32 ± 1
OctA	523 ± 2	26 ± 1	35 ± 5	2.31 ± 1
OleicA	521 ± 2	24 ± 1	16 ± 5	2.33 ± 1
AdA	524 ± 2	19 ± 1	7 ± 4	2.27 ± 1
Reference	528 ± 2	20 ± 1	45 ± 6	2.26 ± 1

Obviously, too short carboxylic acids such as AcA and TriflacA are not suitable for the PNP synthesis. They were supposed to protonate $AdNH_2$ easier than long chain carboxylic acids because they are stronger acids and they do not possess steric hindrances [158]. Nevertheless, it was already described that AcA can undergo a reaction with MABr forming a volatile methylammonium acetate which would cause lowering the concentration of reagents in the precursor solution [179]–[180]. On the other hand, long- and bulk-chain carboxylic acids do not seem to be suitable for surface passivation either, probably because of the interplay of steric

hindrances and the strength of the carboxylic acid. OleicA and AdA are weaker acids in comparison with HeA and thus, formation of Brønsted acid-base equilibrium between carboxylic acids and primary amines is not efficient.
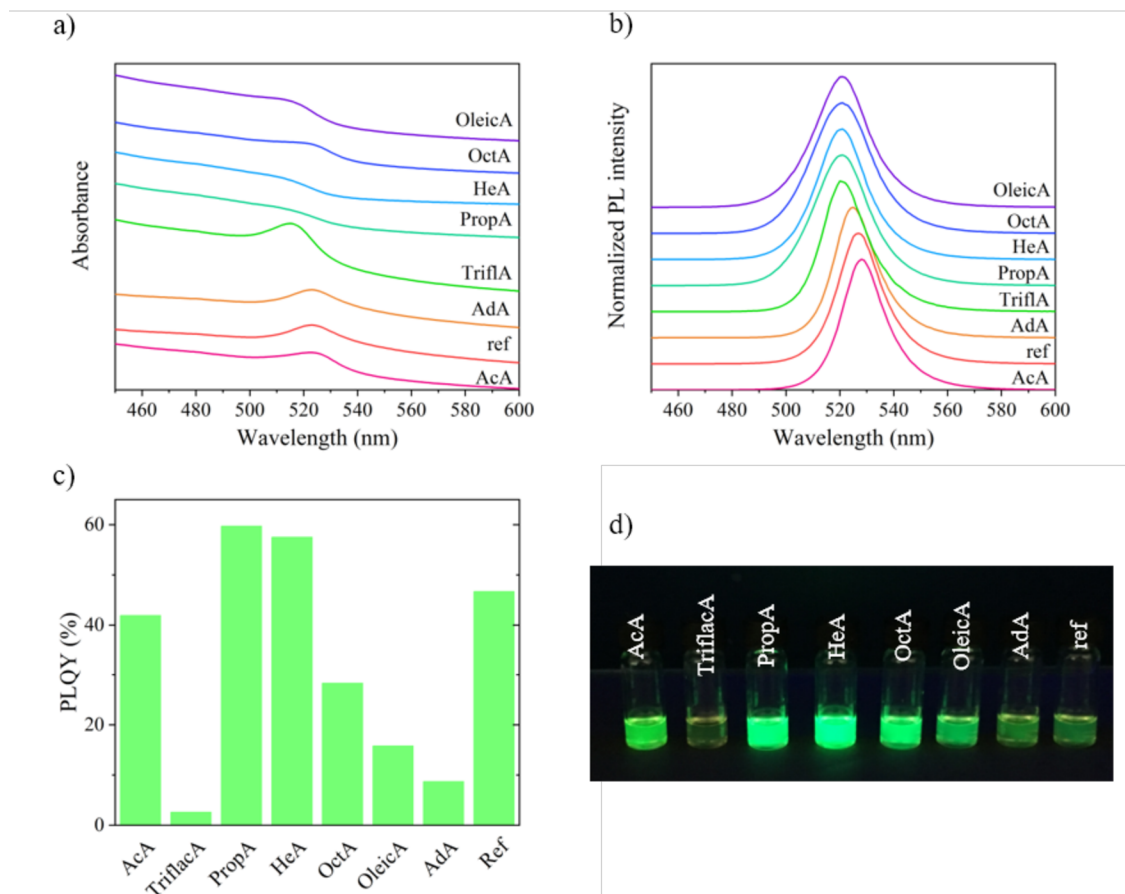

Figure 23: Optical properties of typical colloidal solutions of PNP with different carboxylic acids as capping agents – a) UV-Vis spectra, b) PL spectra, c) PLQY values and d) photos of the colloidal solutions under UV irradiation (excitation wavelength 366 nm).

7.1.10 Colloidal stability

Colloidal stability is an important factor which needs to be evaluated before processing the colloidal solutions into functional devices. Here, the colloidal stability of the colloidal solutions prepared with different carboxylic acid-based capping agents (discussed in the previous section 7.1.9) was studied over the period of 21 days. Namely, emission spectra alongside the PLQYs were monitored to evaluate the colloidal stability (see Figure 24). The colloidal solutions were stored at ambient conditions and sealed externally under parafilm to avoid any contamination. All colloids tended to settle over the time period, nevertheless, it was easy to redisperse them in sonication bath into clear colloidal solutions prior to the measurement.

In general, emission maxima shifted to higher wavelengths and the PLQYs were changing over the time (as shown in Figure 24). For example, freshly prepared PNP stabilized by $AdNH_2$ and PropA exhibited an emission maximum of 521 nm and PLQY of 60%, whereas, the emission maximum was 529 nm and the PLQY was of 27% in case of 21 days old colloidal solution. The band gap shifted from 2.32 to 2.28 eV in the same period of time. Interestingly, colloidal solutions prepared with TriflacA as a carboxylic acid-based capping agent did not exhibit photoluminescence after 3 days anymore.
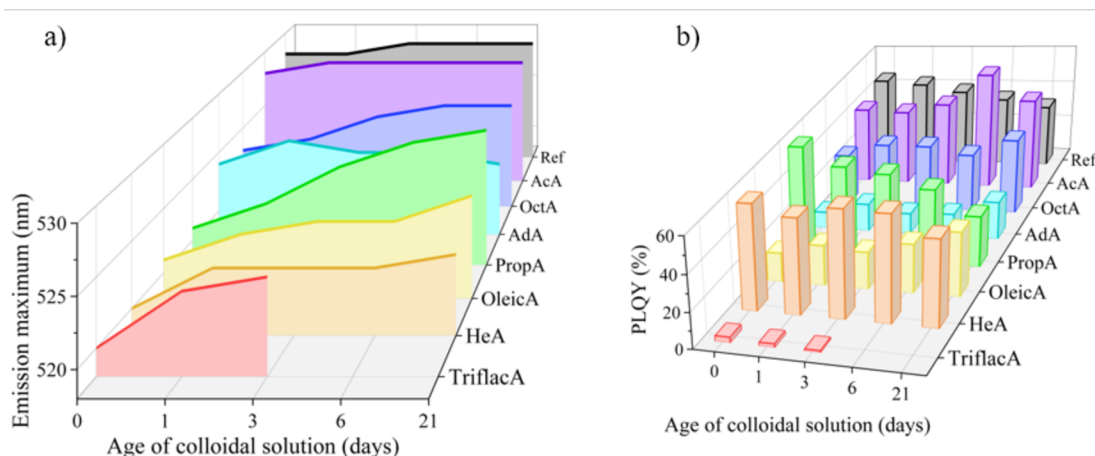
Figure 24: Colloidal stability of PNP prepared with different carboxylic acids as surfactants: a) monitoring emission maxima and b) PLQY over the period of 21 days

The red-shift in the emission spectra was attributed to the degradation of the capping agents attached to the PNP surface. An explanation could be that the organic shell gets thinner because of the leakage of the capping agents over time and the nanoparticles undergo additional growth or aggregation because of the dynamic character of the ligands binding, causing a red shift in the emission spectra [158]. Nevertheless, a different trend was noticed in emission maxima when comparing PropA and HeA with AdA, AcA capping agents for the PNP stabilization.

The AdA and AcA stabilized PNP as well as the reference sample with no carboxylic acid-based capping agent did not possess any significant shift of the emission maxima within the period of 21 days. This observation suggests that no leaking of carboxylic acid-based capping agents causing additional crystal growth or aggregation occurs. Therefore, the hypothesis that AdA and AcA are not able to efficiently stabilize PNP from section 7.1.9 could be correct.

To conclude this study, from the point of view of the colloidal stability, HeA seems to be the best carboxylic acid in combination with AdNH$_2$ since the PLQY decreased from 58 to 46% whereas more significant drop was observed when PropA was used, from 60 to 27%.

7.1.11 Optical properties of centrifugal casted films

Thin films were prepared from PNP dispersion by centrifugal casting method. Centrifugal casting method enables a formation of densely packed and uniform films where the thickness can be easily controlled by adjustment of the PNP concentration in colloidal solutions [101]. Here, PNP stabilized by AdNH$_2$ and HeA (in molar ratio 0.8 and 9.5 with respect to PbBr$_2$) were prepared by precipitating the corresponding precursor solution in toluene in volume ratio 0.002. As prepared colloidal solution of the volume of 25 ml was centrifugal casted (5000 rpm/10 min) onto a glass substrate (1×1 cm). The resulting film was then carefully rinsed with approx. 3 ml of toluene and it was subsequently dried in the toluene atmosphere. A photo of a typical centrifugal casted film is shown in the inset in Figure 25a, the film shows a green light emission under UV irradiation. It is worth emphasizing that PNP were successfully centrifugal casted not only onto glass substrates, but also onto ITO glass, sapphire or glassy carbon substrate. Furthermore, PNP film was also successfully centrifugal casted onto a PEDOT:PSS deposited film showing a high versatility of this method of casting.

UV-Vis and PL spectra of the films prepared on glass substrates are shown in Figure 25a. The emission maximum of 521 nm does not show any significant shift when compared to a typical colloidal solution with emission maximum of 521±2 nm. Nevertheless, a strong decrease in PLQY was observed, the PLQY of the centrifugal casted film was of ~17%, whereas a typical PLQY of the colloidal solution is 48±7%.

In order to demonstrate the surface morphology, atomic force microscopy (AFM) measurements of the centrifugal casted film were performed (Figure 25b). The root mean square (RMS) roughness (Rq) value was 40 nm. Simultaneously, the thickness was measured by a mechanical profilometer, and the detected thickness was 520±100 nm. The standard deviation corresponds to the deviation from the scale bar from Figure 25b. Both AFM and

profilometry showed the inhomogeneous overcoat, even though the substrate was fully covered. From an application point of view, the prepared film was not homogeneous enough to be implemented into a functional device, hence further surface treatment is needed to smooth the resulting films.
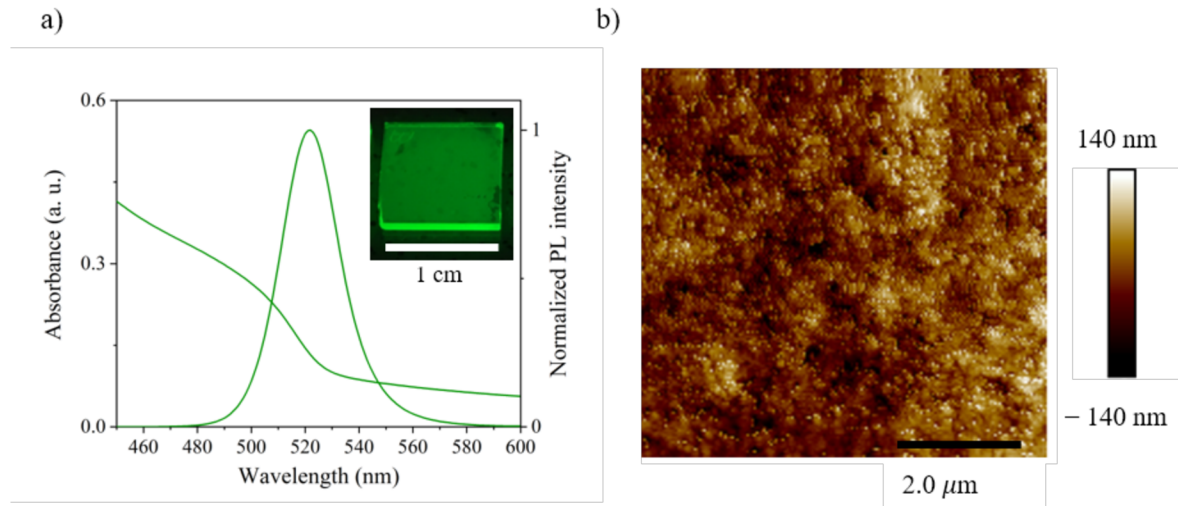

Figure 25: a) Optical properties of centrifugal casted film and its photo under UV irradiation (366 nm) in the inset, b) an AFM image of centrifugal casted film

In order to study the possibility of tuning the thickness of the film, different colloidal solutions were prepared by precipitating the precursor solutions in toluene in volume ratios 0.002, 0.008 and 0.004. The resulting colloidal solution of the volume of 25 ml was centrifugal casted onto the glass substrate by the same procedure as discussed above. The thicknesses of the centrifugal casted films were 520±100, 150±50 and 60±30 nm, respectively. Apparently, lowering the concentration of colloidal solutions helps to prepare films with lowered roughness. For the purposes of this work, volume ratio of precursor solution and toluene was set to 0.002 also for film preparation to obtain comparable data among all samples.

The measured PLQY was significantly lower in films in comparison with the corresponding colloidal solution; it decreased from 48±7% to ca. 17% which is not in agreement with previously reported work [101]. The decrease in PLQY could be caused by preferred non-radiative relaxation processes in PNP at room temperature due to the presence of trap states formed during the loss of capping agents from the nanoparticles surface during the centrifugal casting [181].

To study the effect of the temperature on the optical properties on optical properties, emission spectra were measured at different temperatures ranging from 3 to 300 K.

Wavelengths were calculated into energies in order to evaluate the changes in the symmetry of the emission peaks, as shown in Figure 26a. As expected, the emission intensity increased by two orders of magnitude with decreasing temperature which could be attributed to the suppression of non-radiative relaxation processes [182]. Nevertheless, the emission maxima shifted to lower energies with decreasing temperature, from 2.38 eV (521 nm) to 2.29 eV (540 nm) by decreasing the temperature from 300 to 3 K. Simultaneously, a shoulder in the region of lower wavelengths was observed while reducing temperature. In order to make the changes in emission spectra more evident, emission maxima and FWHM were plotted as functions of logarithm of reciprocal temperature (see in Figure 26b).
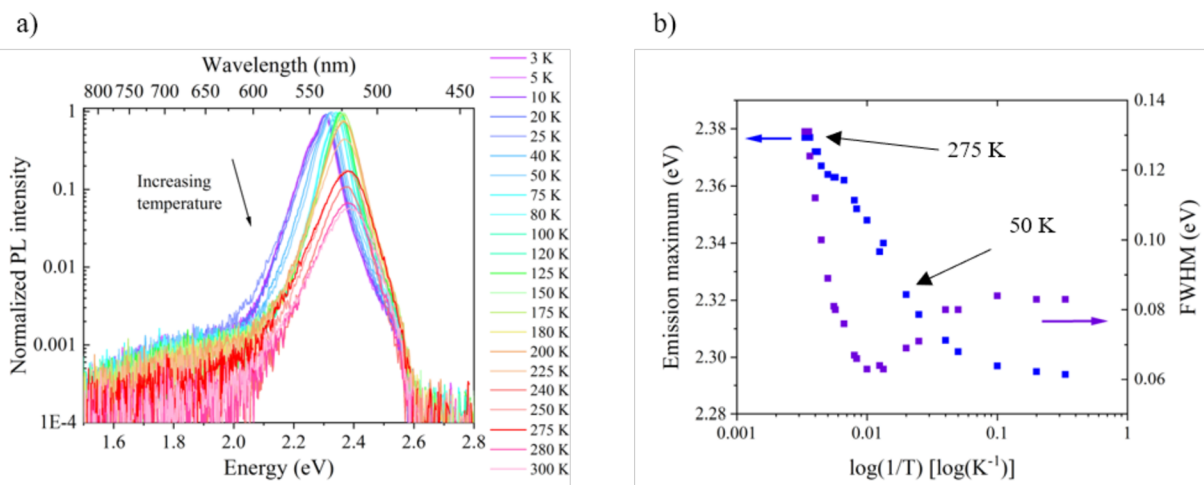

Figure 26: Dependency of emission spectra of centrifugal casted films on temperature – a) emission spectra at different temperatures and b) changes in emission maxima and FWHM at different temperatures

The results presented in Figure 26b highlighted that the temperature may induce changes in crystal lattice. When decreasing temperature, a significant shift in emission maximum to lower energy was detected around 275 K attributed to the phase transition from cubic to tetragonal. From 50 K the emission maximum starts to shift to higher energies related to the phase transition to orthorhombic [183]. In addition, a shoulder in emission spectra detected at lower temperature could indicate a disordered transition to orthorhombic phase. Due to the low mobility of MA cations at lower temperature, MA-ordered and MA-disordered orthorhombic domains of different optical properties can be formed during the phase transition [184].

7.2 Amino acids as ligands for PNP stabilization

In general, amino acids have already been employed in surface decoration of different nanomaterials and they have proved to broaden the functionality of the resulting material as discussed in section 4. For example, decorating CdSe and ZnS quantum dots with cysteine and histidine ligands improves solubility in water and biocompatibility [185]. Moreover, surface decoration of gold nanoparticles with amino acids enables self-assembly properties [186]. Here, PNP were stabilized by proteinogenic essential amino acids L-lysine (Lys) and L-arginine (Arg) (structures are shown in Figure 27), alongside different carboxylic acids, namely HeA, OleicA or AdA, their structures already showed Figure 22. Both Lys and Arg possess primary amine and guanidine moiety in their side chains, respectively, which can be employed in PNP growth control and stabilization. On the other hand, α-amino and carboxylic groups are supposed to be decorating the surface of the shell and being available for further interactions. Results from this section are summarized in a work reported by A. Jancik Prochazkova *et al.* [148].

Figure 27: Structure of amino acids L-lysine and L-arginine

7.2.1 Optical properties of PNP stabilized by amino acids

To support the conclusions from section 7.1, both amino acids Lys and Arg were used for PNP stabilization alongside HeA presenting a short chain carboxylic acid, OleicA presenting a long chain carboxylic acid and with AdA presenting a bulk chain carboxylic acid. Simultaneously, toluene and chloroform were employed as precipitation media to deepen the study about different solvent systems (section 7.1.6). Trying all possible combinations gave 12 samples (see further Table 8 in detail) and in all cases colloidal solutions were formed. Photos of all prepared samples are shown in Figure 28 where the name of the samples referred to the solvent and to a combination of amino- and carboxylic acid-based capping agents.
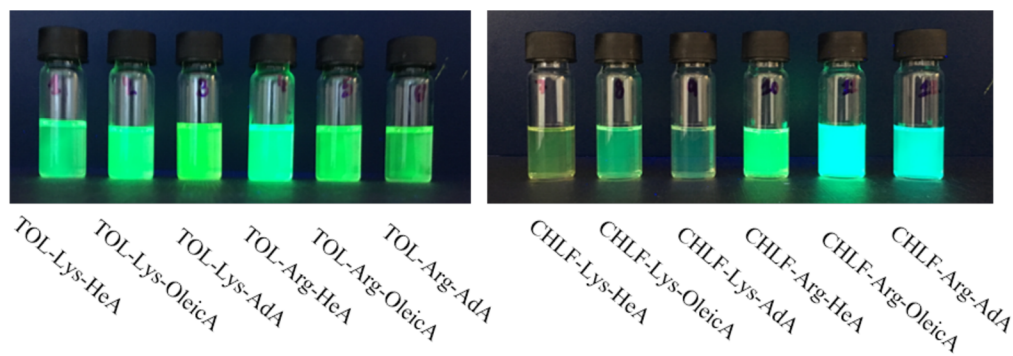
Figure 28: Colloidal solutions of PNP stabilized by amino acids and different carboxylic acids-based capping agents, photos under UV irradiation (366 nm)

UV-Vis and PL spectroscopy techniques were employed in order to evaluate optical properties of colloidal solutions (see in Figure 29 and Table 8). As expected, and according to the previous results (section 7.1), absorption onsets of all samples were in the green part of the visible spectrum. In addition, emission maxima of the toluene-based colloidal solutions were in the range 520–528 nm whereas chloroform-based samples exhibited blue-shift in emission maxima ranging from 491 to 509 nm. Figure 29 showed not only a blue shift of chloroform-based colloidal solutions with comparison to toluene-based samples, but also a broadening of the emission spectra was evident. Table 8 demonstrates that FWHM of emission spectra of toluene-based colloidal solutions is in the range 20–23 nm whereas the FWHM of emission spectra of chloroform-based colloidal solutions is in the range 22–36 nm. Interestingly, it was observed that FWHM tends to be lower in colloids containing AdA (Table 8) which could be attributed to a higher degree of self-organization that is common in adamantyl-based compounds [99] and [100]. Simultaneously, a significant decrease in PLQY was observed when PNP were prepared in chloroform (in agreement with previous experiments described in section 7.1.6). For example, PNP stabilized by Lys and HeA prepared in toluene (noted as sample TOL-Lys-HeA-PNP) and in chloroform (noted as sample CHLF-Lys-HeA-PNP) exhibited PLQY of 76±17 and 5±2%, respectively. Here, it is worth to emphasize that PLQY was measured via "direct excitation" method described in 6.3.2 and quite large values of standard deviation (compared to toluene-based colloidal solution of PNP stabilized by AdNH$_2$ and HeA described in 7.1.1) might be coming from the experiment set-up.

Additionally, the lower PLQY detected in the samples prepared chloroform might be related to the aprotic nature of the solvent that often acts as luminescence quencher, an effect already reported [166]–[167]. To test this assumption, we added an equal amount of toluene to all the samples prepared in chloroform and *vice versa*. As a result, the addition of chloroform to

toluene-based samples showed an average of five-fold PLQY decrease from initial ~100% to ~20%. On the other hand, the addition of toluene to chloroform-based samples yields an approximately two-fold PLQY increase.
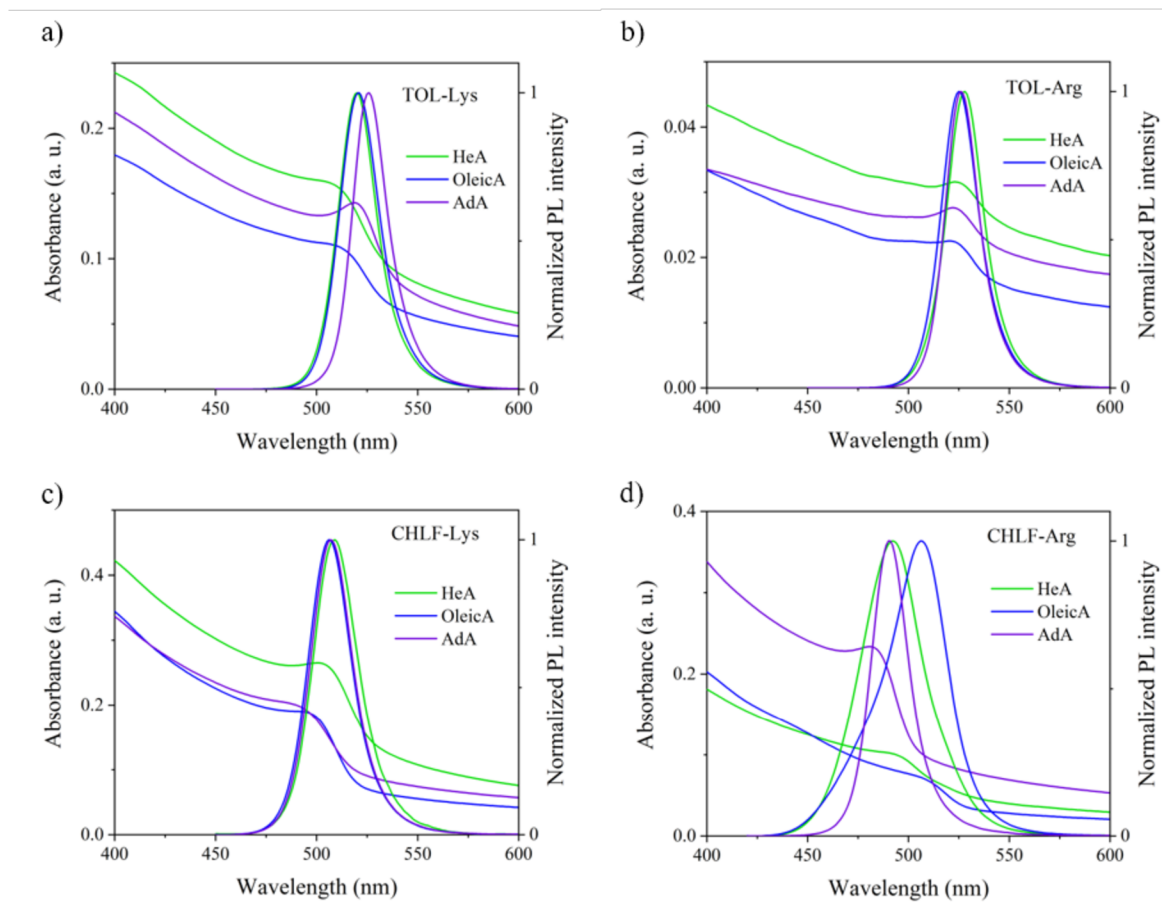

Figure 29: Optical characterization of amino acids stabilized PNP

However, the blue-shift of emission spectra could suggest that PNP prepared in chloroform grow smaller than those prepared in toluene and the broadening of the emission spectra could be attributed to a non-homogeneous size distribution. In order to support these assumptions, TEM images of all samples were taken (Figure 30), typical diameters of PNP are listed in Table 8. The TEM images confirmed the presence of nanoparticles in all samples. In agreement with previous results from $AdNH_2$ stabilized PNP (Figure 13), sub-10 nm PNP stabilized by amino acids were spherical and highly crystalline. As expected, PNP prepared in chloroform exhibited a smaller diameter than nanoparticles prepared in toluene. An average size of PNP prepared in chloroform was in the range of 5–6 nm whereas PNP prepared in toluene had an average diameter of 6–8 nm. Here, the blue-shift in emission spectra of chloroform-based colloidal solutions can be explained by the quantum confinement effects. Lowering the PNP dimension during the precipitation in chloroform was attributed to the

presence of electronegative chlorine atoms of chloroform that can coordinate Pb^{2+} [186] and [187]. Nevertheless, solvatochromism effects due to the solvent induced aggregation could also take place here [188].

Regarding the size distribution of PNP in individual samples, PNP prepared in chloroform exhibited broader size distribution than PNP prepared in toluene. For example, the average size of TOL-Lys-HeA-PNP was of 8±2 nm presenting a deviation of 25% of the average size of nanoparticles whereas the average size of CHLF-Arg-HeA-PNP was of 8±2 nm, presenting a deviation of 33% of the average size of nanoparticles. This finding can support the difference in FWHM which was of 22 and 36 nm for TOL-Lys-HeA-PNP and CHLF-Arg-HeA-PNP samples, respectively. Here, it is worth noting that PNP of sizes below 3–4 nm were not detected because of the resolution of transmission electron microscope.

Table 8: Optical characterization of amino acids stabilized PNP and comparison of their diameters

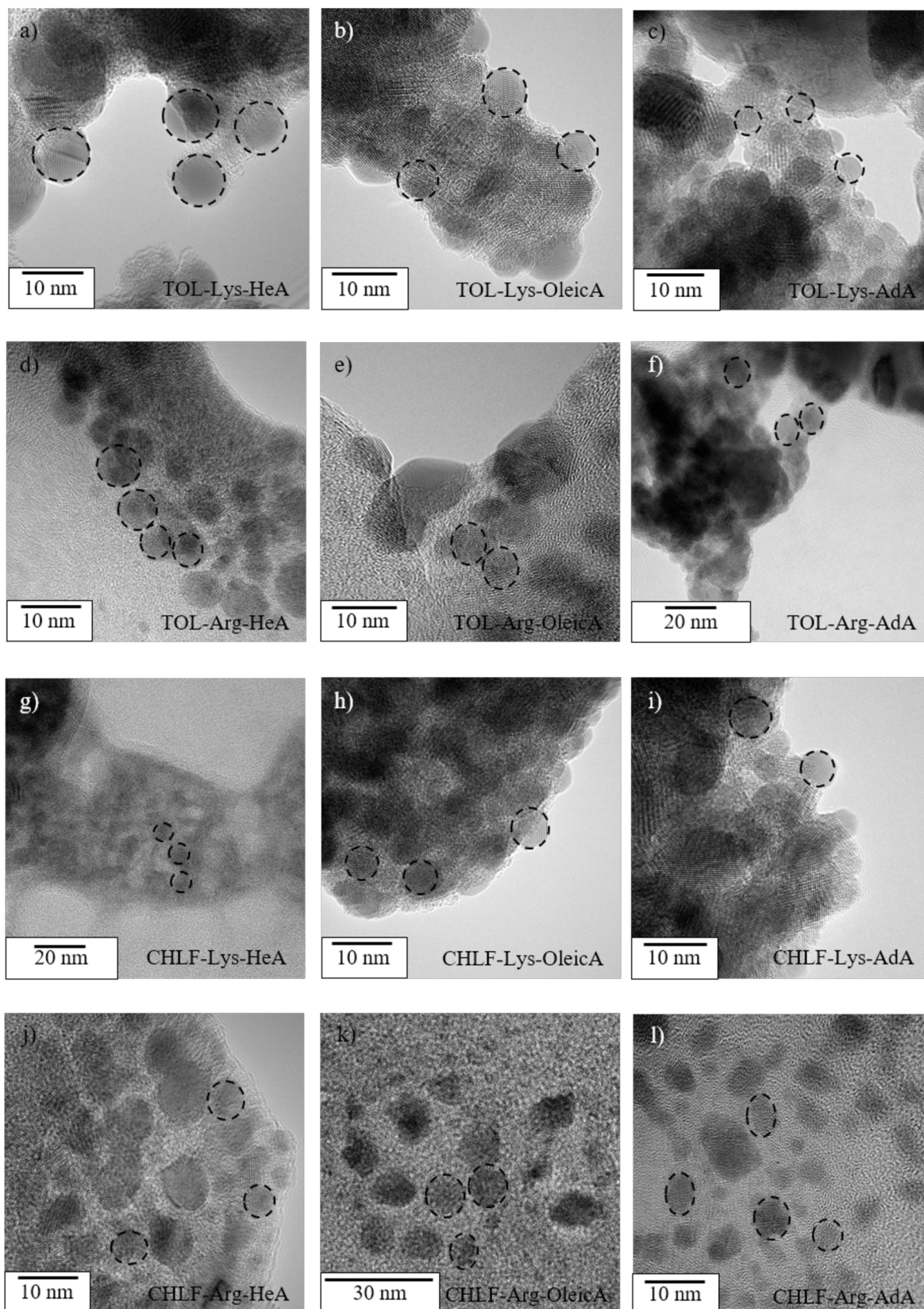| Sample	Carboxylic acid	Emission maximum (nm)	FWHM (nm)	PLQY (%)	E_g(eV)	PNP diameter (nm)
TOL-Lys	HeA	520	22	76±17	2.31	8±2
	OleicA	521	23	75±19	2.31	7±2
	AdA	526	21	71±28	2.30	7±2
TOL-Arg	HeA	528	22	92±7	2.28	6±1
	OleicA	525	22	72±20	2.29	6±1
	AdA	526	20	71±17	2.28	7±1
CHLF-Lys	HeA	509	26	5±2	2.34	5±1
	OleicA	506	25	19±9	2.38	5±1
	AdA	508	26	6±1	2.38	5±1
CHLF-Arg	HeA	492	36	7±2	2.40	6±2
	OleicA	507	36	33±14	2.28	6±2
	AdA	491	22	4±1	2.46	5±1

Figure 30: TEM images of PNP stabilized with amino acids and different capping agents

7.2.2 Comprehensive characterization of PNP stabilized by amino acids

The perovskite-like structure of the amino acids-stabilized PNP was confirmed by powder XRD (spectra shown in Figure 31). The spectra from the nanoparticles were compared to the bulk $MAPbBr_3$ perovskite crystal, see Figure 12. Reflections (001), (011), (111), (002), (021), (211), (220), (300) and (310) were found at peaks positioned at 14.90°, 21.14°, 26.02°, 30.07°, 33.72°, 37.08°, 43.05°, 45.83° and 48.42°2θ which are typical for $MAPbBr_3$ perovskite-like structure with a cubic unit cell structure [76]. In general, PNP samples exhibited peak broadening when compared to bulk $MAPbBr_3$ that stems from the small size of the crystallites [157].
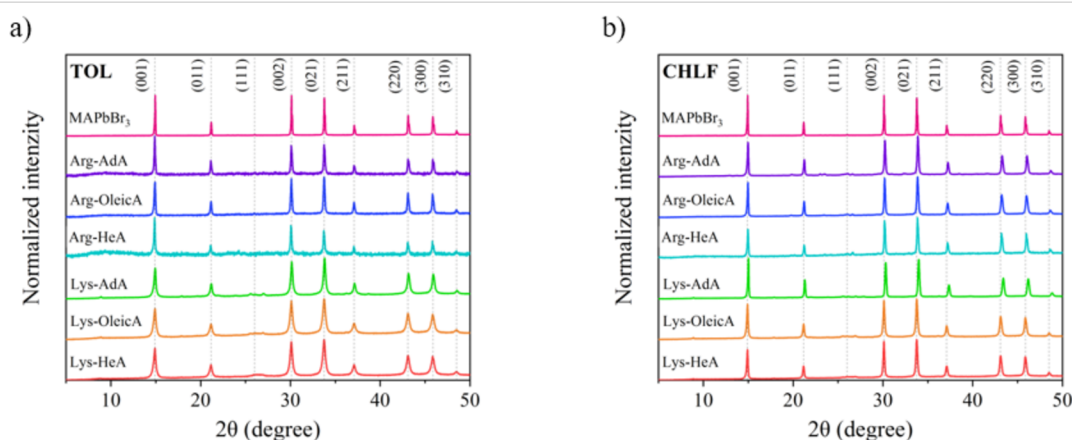

Figure 31: Powder XRD spectra of PNP stabilized by amino acids as capping agents which were prepared in a) toluene and in b) chloroform

In addition, FTIR spectra were recorded and compared with the spectra of precursor chemicals. Figure 32 shows typical FTIR spectra of PNP stabilized by amino acids alongside HeA. As observed previously (section 7.1.8), characteristic N–H stretch vibrations were found around 3100–3200 cm^{-1} as well as C–H rocking bonds at 1000 and 912 cm^{-1} in all PNP samples pointing out to a presence of methyl group from MABr, as reported in [175]–[176] and [189]. Furthermore, a peak in the region around 1498 cm^{-1} is assigned to the interaction between COO^- and NH_3^+ groups from the carboxylic acid and methylammonium or protonated primary amine from amino acids [190].

In general, spectra of pure Lys and Arg show two bands at 2851 and 2925 cm^{-1} attributed to the asymmetric and symmetric CH_2 stretching, respectively [190]. These signals were found in both spectra of PNP. Additionally, as expected, C–N stretching from amine groups from Arg were detected at 1181 cm^{-1} in both Arg stabilized PNP [191]. Finally, C=O vibrations from carboxylic group of Lys (at 1577 cm^{-1}) or Arg (at 1614 cm^{-1}) appear at higher wavenumbers

80

in Lys stabilized PNP (1584 cm^{-1}) and lower in Arg stabilized PNP sample (1564 cm^{-1}), respectively [177] and [191].
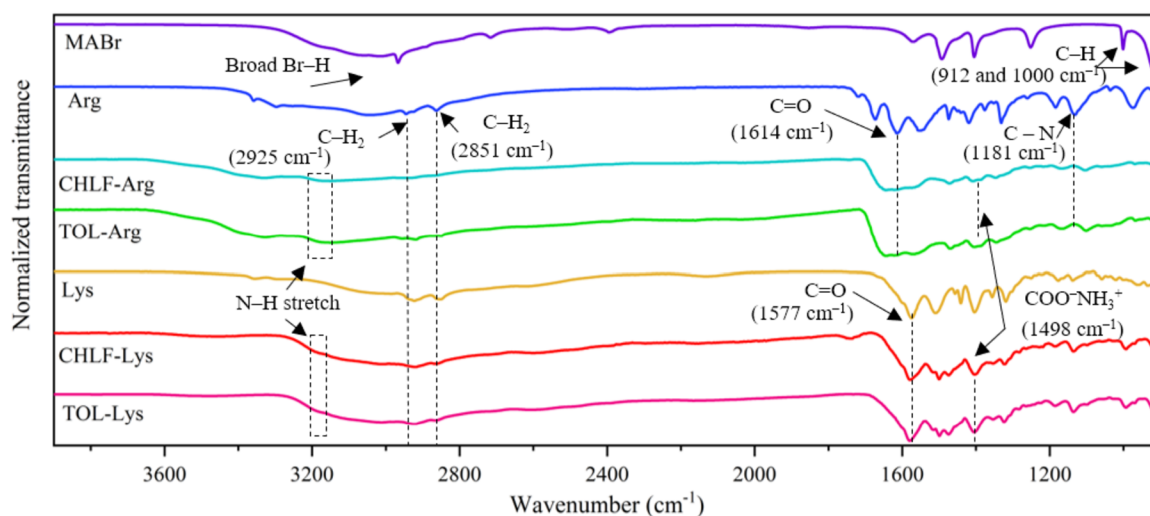
Figure 32: FTIR spectra of PNP stabilized by amino acids Lys or Arg alongside hexanoic acid

7.2.3 Amino acids with protected α−amino groups for PNP stabilization

DFT calculations revealed that the ε−amino group and the guanidyl group of side chains of Lys and Arg are employed in PNP stabilization in preference to the α−amino group [148]. To support the calculation, Lys and Arg analogues with protected α−amino group N_α-(*tert*-Butoxycarbonyl)-L-lysine (boc-Lys) and N_α-(*tert*-Butoxycarbonyl)-L-arginine (boc-Arg) (Figure 33), were used for PNP stabilization to favour selective bonding between positively charged side chains of the amino acids.

N_α-(*tert*-Butoxycarbonyl)-L-lysine
(boc-Lys)

N_α-(*tert*-Butoxycarbonyl)-L-arginine
(boc-Arg)

Figure 33: Structures of boc-Lys and boc-Arg used for PNP stabilization

PNP stabilized by boc-Lys and boc-Arg were prepared using HeA as a carboxylic acid-based capping agent. The colloidal solutions were prepared by the ligand-assisted precipitation method as in case of Lys and Arg stabilized PNP. The precursor ratio was 1:1.1: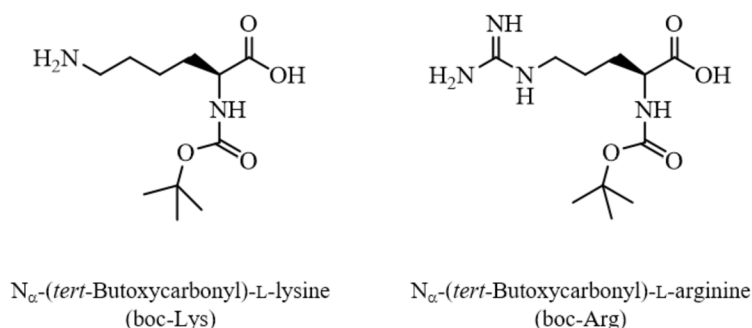0.8:9.5 for PbBr$_2$, MABr, boc-protected amino acid and HeA, respectively, all dissolved in DMF. The precursor solution was subsequently precipitated in toluene in volume ratio 0.002. In both samples, clear colloidal solutions exhibiting green emission under UV irradiation were obtained (see in insets in Figure 34a and b). Both, boc-Lys and boc-Arg PNP suspensions showed bright blue and cyan luminescence, respectively, under UV illumination (insets in Figure 34 a and b). The complete optical data of boc-Lys and boc-Arg stabilized PNP are summarized in Figure 34a and b and Table 9 the. Interestingly, the emission spectra of the PNP stabilized with boc-Lys and boc-Arg are significantly blue-shifted by 38 and 5 nm, respectively, when compared to their unmodified counterparts TOL-Lys-HeA-PNP and TOL-Arg-HeA-PNP (compared with Table 8). Whereas, the PLQY of the samples synthesized with boc-protected amino acids remained high, though for boc-Lys was about 60%, whereas for boc-Arg was about 95%.

Table 9: Optical properties of boc-Lys and boc-Arg stabilized PNP

Ligand	Emission maximum (nm)	FWHM (nm)	PLQY (%)	E$_g$ (eV)	PNP diameter (nm)
boc-Lys	482	32	60±10	2.56	4.4±0.5
boc-Arg	523	22	94±5	2.33	6.1±1.0

In addition, TEM images of PNP (Figure 34c and d) show spherical particles with an average diameter of 4.4±0.5 nm and 6.1±1.0 nm for PNP stabilized by boc-Lys and boc-Arg, respectively. Notably, the nanoparticles prepared using amino acids with a protected α−amino group exhibited smaller diameter, when compared to their unmodified counterparts. As already discussed in Table 8, TOL-Lys-HeA-PNP and TOL-Arg-HeA-PNP exhibited an average diameter of 8±2 nm and 6±1 nm, respectively. Taking this into consideration, the blue shift obtained could be partly attributed to quantum confinement effects.

The formation of smaller PNP with the use of α−amino protected group can be caused by preventing the self-organization of the amino acids in the solution between deprotonated carboxylic group and the protonated α−amino group [192] and [193]. Therefore, side chains in

boc-protected amino acids do not compete with $\alpha-$amino groups to interact with the perovskite precursors, resulting in more efficient PNP formation.
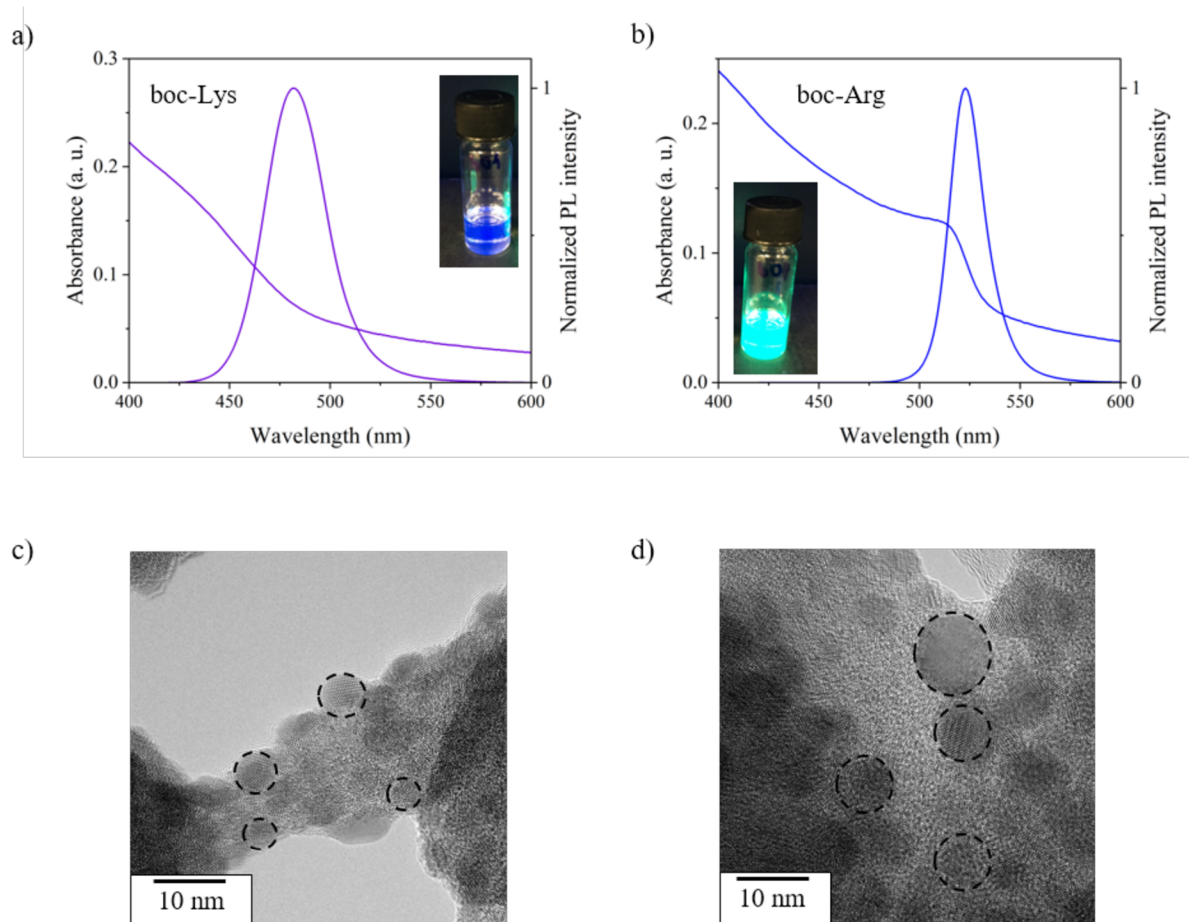

Figure 34: Characterization of PNP stabilized by boc-Lys and boc-Arg: a) and b) UV-Vis and PL spectra of boc-Lys and boc-Arg stabilized PNP; insets:photos of colloidal solutions under UV irradiation (366 nm) and c), d) corresponding TEM images of the samples

7.3 Influence of the additions of water into the precursor solutions

Lead halide perovskite materials are known to undergo a rapid decomposition in humid environments [194]–[195]. Intercalated water molecules interact with halides of PbX_6 and ammonium moiety of MA via hydrogen bonding to form $MAPbX_3 \cdot H_2O$ hydrated species. Water migration through the material is more facile as going from X = Cl⁻ to Br⁻ and to I⁻ in $MAPbX_3$ due to increasing ionic radius and extending Pb–X interaction. Hence, the presence of iodide ions in the perovskite structure provides the easiest passage for ions and water molecules [195].

On the other hand, a certain amount of water present in the precursor chemicals, precursor solutions or present during their processing is reported to facilitate nucleation and crystallization of the perovskite material [155]. In this case, water weakly binds to methylammonium ions and forms a reversible hydrated phase within the perovskite, which quickly forms dehydrated perovskite after the thin film deposition procedure [196]. For example, a defined amount of water added into methylammonium iodide solution in isopropyl alcohol improved the crystallization of the perovskite material, which helped to form larger grain size during the sequential deposition of perovskite films [197]. Simultaneously, a certain amount of water can benefit to form a homogeneous solution by increasing solubility of the precursor chemicals in the precursor solution [198].

In agreement with aforementioned, we found out that optical properties of boc-Lys stabilized PNP described in section 7.2.3 exhibited a dependency on the water content within the precursor solutions. Additions of water into the precursor solutions ranging from 0 to 32 mol. eq. with respect to $PbBr_2$ caused shifting of emission maxima in the range from 476 to 505 nm due to quantum confinement. The above-mentioned findings are presented in a publication by A. Jancik Prochazkova *et al.* [149].

7.3.1 Colloidal solutions characterization

Precursor solutions containing $PbBr_2$, MABr, boc-Lys and HeA in ratio 1:1.1:0.8:9.5 were prepared in a glove box to avoid moisture contamination. Finally, deionized water was added in amounts corresponding to 0–32 mol. eq. with respect to $PbBr_2$. The precursor solutions were left to be stirred for 7 days inside the glove box. It is worth noting that boc-Lys was badly soluble in the precursor solution; if no water was added, and the precursor solution was cloudy. Whereas, the precursor solutions with a small amount of water (e.g. 0.4 mol. eq.) appeared as

a clear solution and thus, more homogeneously dissolved. Obviously, the addition of water favoured dissolving all precursor chemicals in the precursor solution.
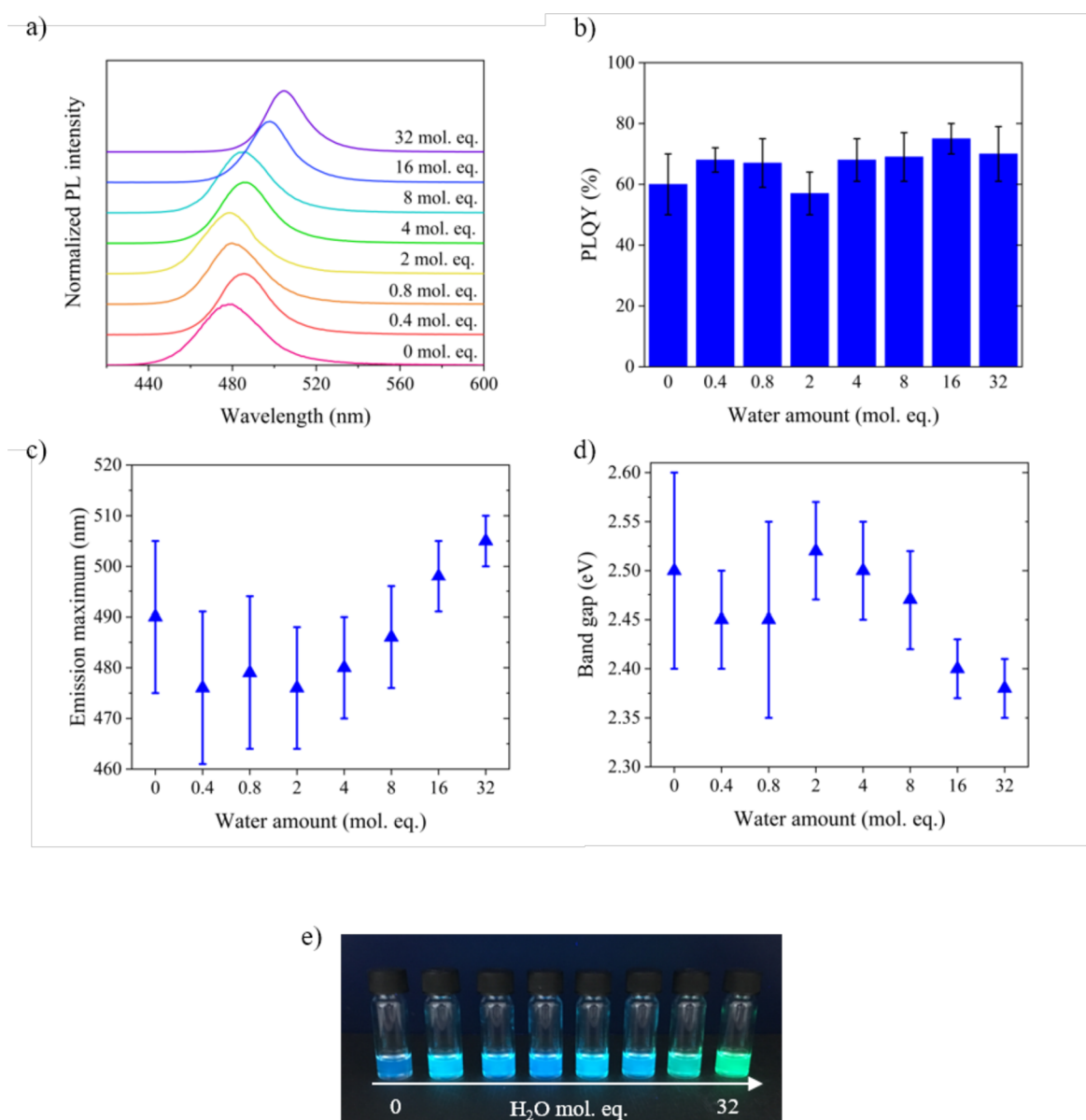
Figure 35: Optical properties of boc-Lys stabilized PNP colloidal solutions, dependency of the addition of water into the precursor solutions on a) emission spectra, b) PLQY, c) emission maxima and d) band gap

All the prepared samples formed a colloidal solution after the precipitation in toluene in the volume ratio 0.002 (Figure 35e). The reference sample without any water addition exhibited greenish-blue emission with an emission maximum at ~490 nm as already shown in section 7.2.3. The emission maximum of the PNP changed rapidly after an addition of water from 0.4 to 2 mol. eq., a blue shift was observed up to 10 nm (Figure 33a). Interestingly, emission maxima shifted to higher wavelengths when the addition of water was further increased, as

demonstrated in Figure 35. The band gaps were changing correspondingly. In addition, increasing additions of water remarkably enhanced the PLQY of the PNP. As shown in Figure 35b, the PNP prepared without any water addition exhibited a PLQY of 60%. An addition of 32 mol. eq. of water with respect to $PbBr_2$ caused an increase of up to 70%. Simultaneously, FWHM of the emission spectra showed a significant decrease with an increasing amount of water in the precursor solution. The colloidal solution without any water addition showed FWHM of 34 nm whereas colloidal solution prepared from the precursor solution containing 32 mol. eq. of water with respect to $PbBr_2$ showed FWHM of 22 nm. All observations, such as the increase of PLQY and the decrease of deviation and FWHM with increasing additions of water into the precursor solutions, suggest better stabilization of PNP in the colloidal solutions. The better stabilization of PNP was attributed to the improvement of the solubility of boc-Lys in the precursor solution. Moreover, water molecule is supposed to support the complex formation in the precursor solution [155].
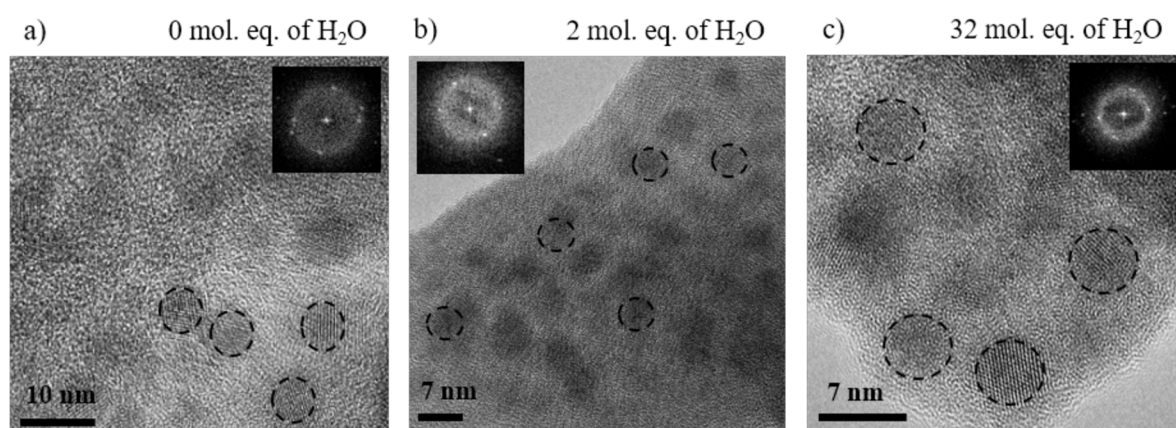
Figure 36: TEM images of boc-Lys stabilized PNP prepared from precursor solutions with different addition of water – a) 0 mol. eq., b) 2 mol. eq. and c) 32 mol. eq. with respect to PbBr₂ with corresponding FFT images in the insets

To evaluate the influence of water in the precursor solutions on the resulting morphology of PNP, TEM images of samples prepared from precursor solutions containing 0, 2 and 32 mol. eq. of water with respect to $PbBr_2$ were taken (Figure 36a, b and c, respectively). The TEM images revealed spherical and crystalline nanoparticles. The average size of PNP was 4.4±0.5, 4.0±0.5 and 6.2±0.6 nm in samples prepared from precursor solutions with addition of 0, 2 and 32 mol. eq. of water with respect to $PbBr_2$, respectively. Aforementioned shifts in emission maxima were probably caused by quantum confinement effects. The most blue-shifted emission maximum of the sample prepared from the precursor solution with 2 mol. eq. of water was of 476 nm, corresponding to the smallest measured diameter of ~4 nm. On the contrary, the

biggest PNP of ~6.2 nm were detected in the sample prepared from the precursor solution with an addition of 32 mol. eq. of water which exhibited the most red-shifted emission spectra with the maximum at 505 nm.

7.3.2 Films characterization

The influence of the additions of water on the optical properties of the corresponding films was evaluated and the same trends as in colloidal solutions were observed, see results in Figure 37. Interestingly, an increase in the PLQYs with an increasing amount of water in the precursor solutions was more significant in films than in colloidal solutions of nanoparticles. Thin films prepared from PNP without any addition of water exhibited the PLQY of 60%. Whereas the solid-state PLQY increased to 87–93% after an addition of 32 mol. eq. of water with respect to $PbBr_2$ (Figure 37b). The comprehensive list of optical properties of the films in comparison with optical properties of the corresponding colloidal solutions is summarized in Table 10.

Table 10: Optical properties of boc-Lys stabilized PNP in colloidal solutions and in films prepared from precursor solutions with different additions of water

Mol. eq. of water	Emission maximum (nm)		FWHM (nm)		PLQY (%)		Band gap (eV)	
	Solution	Film	Solution	Film	Solution	Film	Solution	Film
0	490±15	483±15	34	32	60±10	60±10	2.50±0.10	2.50±0.10
0.4	476±15	485±15	28	23	68±4	75±10	2.45±0.05	2.48±0.05
0.8	479±15	490±15	30	32	67±8	60±10	2.45±0.10	2.50±0.10
2	476±12	492±15	30	23	57±7	60±10	2.52±0.05	2.50±0.05
4	480±10	493±15	28	29	68±7	65±10	2.50±0.05	2.55±0.05
8	486±10	499±10	29	20	69±8	70±10	2.47±0.05	2.47±0.05
16	498±7	502±5	24	22	75±5	80±10	2.40±0.03	2.43±0.03
32	505±5	506±3	22	22	70±9	87±5	2.38±0.03	2.40±0.03

In order to test whether the PLQY can be further enhanced by increasing the concentration of water in the precursor solution, a sample containing 64 mol. eq. of water with respect to $PbBr_2$ was prepared. In this case, an emission maximum of 508 nm in thin film was observed and the PLQY was of 50%, demonstrating that there is a limit of the water content which is needed to obtain the highest PLQY of PNP.
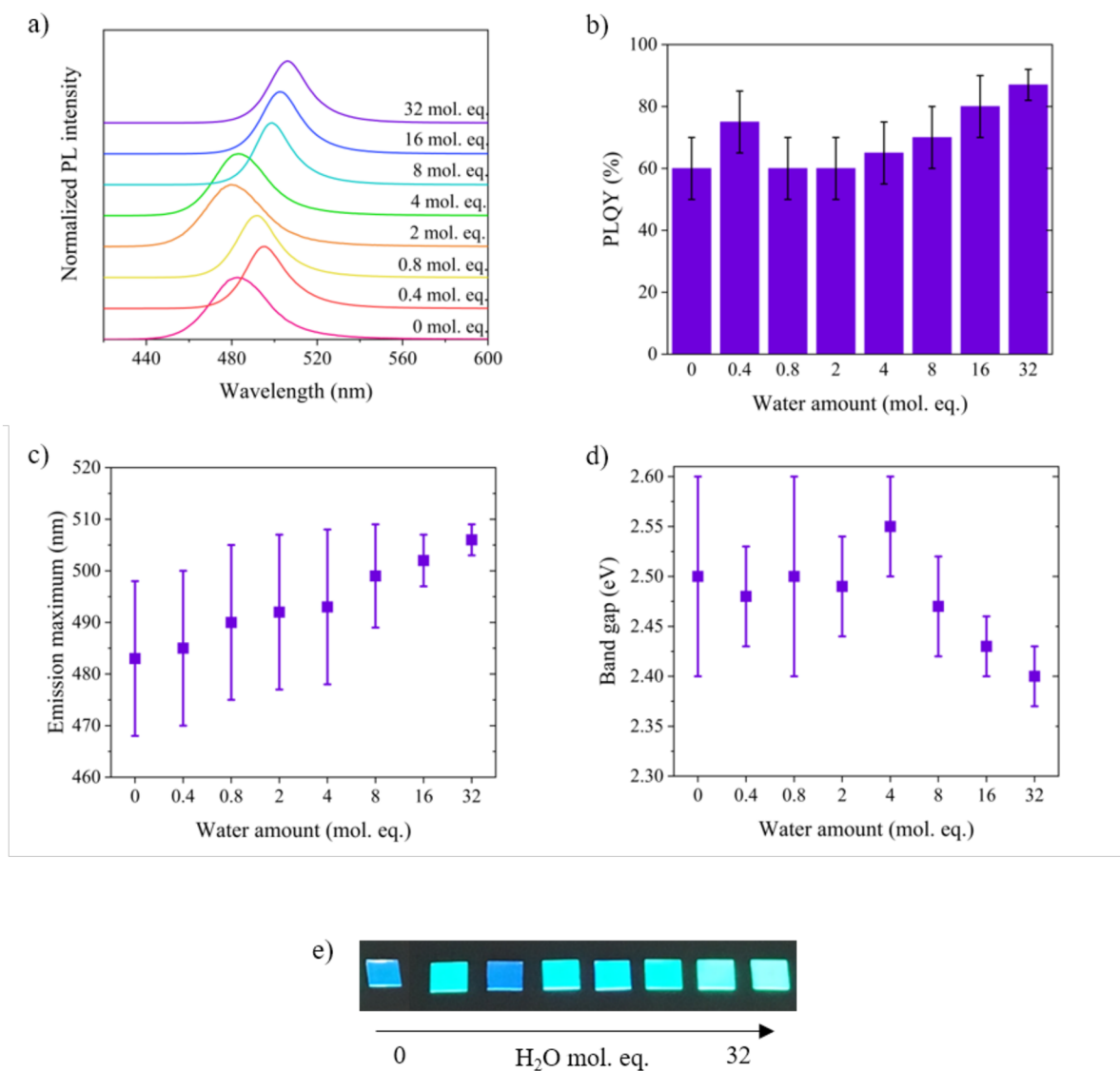

Figure 37: Optical properties of boc-Lys stabilized PNP films, dependency of the addition of water into the precursor solutions on a) emission spectra, b) PLQY, c) emission maxima and d) band gaps

7.3.3 Optical stability

The PL spectra of the prepared colloidal solutions and thin films were re-measured after two days in order to evaluate the optical stability of the samples. The samples were prepared from precursor solutions with 0, 2 and 32 molar equivalents of water with respect to $PbBr_2$ (see Figure 38). In general, it was observed that the emission maxima shifted to higher wavelengths in both colloidal solutions and films after two days (Figure 38a and b). Remarkably, the shift became smaller with an increasing addition of water into the precursor solution. The emission maximum of a film prepared from the precursor solution without any addition of water was red-shifted about 11 nm. Whereas, if 32 mol. eq. of water were added to the precursor solution, the red shift observed was only of 1 nm after two days. In general, a broadening of the emission spectra was detected with time, assuming that aggregates of nanoparticles are formed with time.
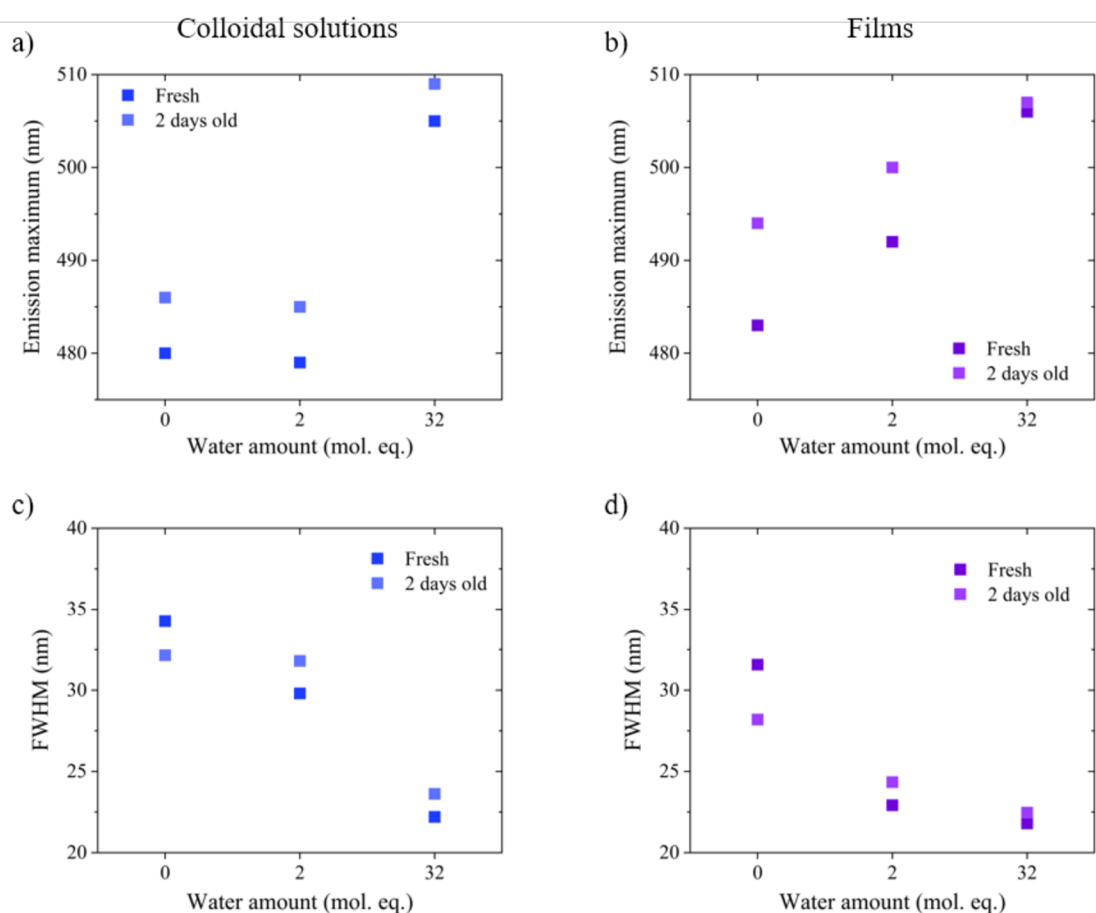

Figure 38: Optical stability of boc-Lys stabilized PNP, emission maxima changes a) in colloidal solutions and b) in films and changes in FWHM c) in colloidal solutions and d) in films

As shown in Figure 38b and d, films prepared from a precursor solution containing 32 mol. eq. of water with respect to $PbBr_2$ exhibit improved stability of optical properties than samples prepared without any water addition to the precursor solution. Therefore, optical properties of the sample prepared from the precursor solution with 32 mol. eq. of water were studied over the period of 77 days (Figure 39). Here, the emission maximum was observed to shift about 4 nm to higher wavelengths over the period of 77 days. At the same time, PLQY dropped from 93% to 86% in the same period. It is worth noting that the film was stored at ambient conditions in the Petri dish in order to avoid any contamination.

Figure 39: Optical stability of film of boc-Lys stabilized PNP with an addition of 32 mol. eq. of water with respect to $PbBr_2$ in the precursor solution

Moreover, the emission spectra were recorded at different temperatures in the range from 2 to 325 K as for $AdNH_2$ stabilized PNP in section 7.1.11. As expected, PL intensity increased with decreasing temperature as shown in Figure 40a. The increase was over an order of magnitude. Simultaneously, shifting of emission maxima to higher wavelengths and thinning of the emission spectra was observed with decreasing temperature, as shown in Figure 40b in detail. Changes in the spectra point out to the phase transition from cubic to tetragonal and to orthorhombic around 275 and 50 K, respectively [183]. Those results were in agreement with previous experiments. From this point of view, it was assumed that the presence of water in the precursor solution favourably assists the complex formation and helps during the precipitation.
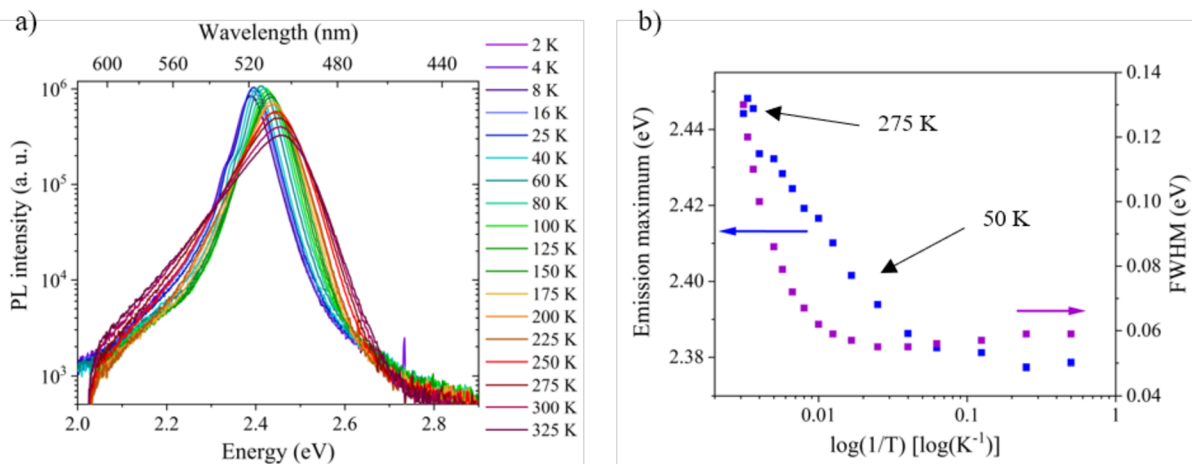
Figure 40: Dependency of emission properties on temperature – a) emission spectra at different temperatures, b) emission maxima and FWHM as a function of temperature for boc-Lys stabilized PNP prepared from precursor solution with an addition of water 32 mol. eq. with respect to PbBr₂

7.3.4 Morphology of the films

From the point of view of high PLQY and good optical stability, PNP prepared from a precursor solutions containing 32 mol. eq. of water with respect to $PbBr_2$ can be expected to be applicable into functional devices. For that aim, it is necessary to evaluate the morphology of the films. As in previous work [101], films were prepared from colloidal solutions with different concentrations of PNP. The colloidal solutions were prepared by precipitating different volume ratios of precursor solution in toluene. The resulting colloidal solutions (in final volume of 25 ml) were centrifugal casted onto glass substrates. As expected, the resulting films were thinner and their roughness was smaller with reducing the concentration of PNP in the colloidal solutions (Table 11).

Table 11: Varying thickness of films by tuning the concentration of PNP by changing the volume ratio between precursor solution and toluene during the precipitation

Volume ratio	Thickness (nm)
0.002	400±100
0.0008	200±60
0.0004	170±70
0.0002	60±20

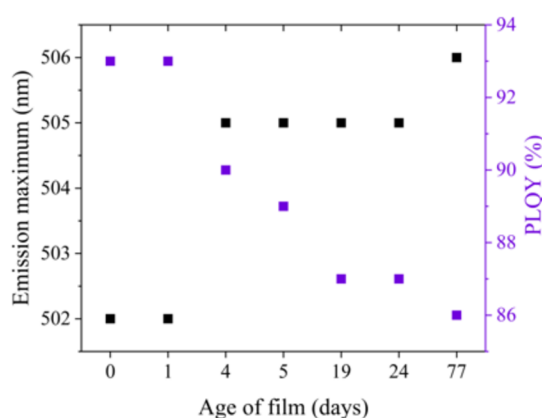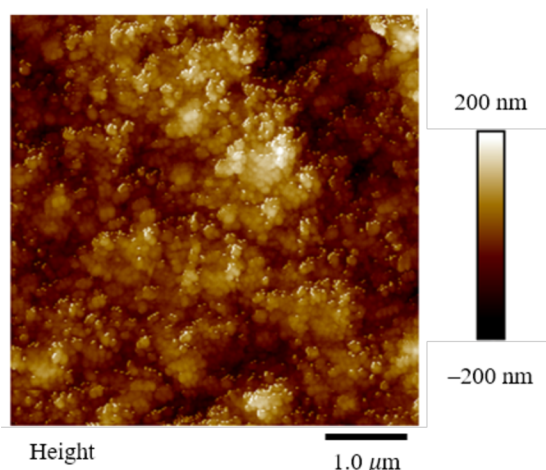*Figure 41: An AFM image of film of boc-Lys stabilized PNP with addition of 32 mol. eq. of water with respect to PbBr2 in the precursor solution (image Rq 55 nm)*

An AFM image of the film prepared by precipitating precursor solution in toluene in volume ratio 0.002 was captured (Figure 41) and the root-mean-square (RMS) roughness (Rq) value estimated to be 55 nm The film was considered then less homogeneous than the one prepared with AdNH2 stabilized PNP, see discussion in section 7.1.11.

7.3.5   Comprehensive characterization of PNP stabilized by boc-Lys

Water-soluble amino acids exhibit limited solubility in organic solvents including polar solvents such as DMF [199], what supported the observation that the precursor chemicals showed poor solubility in the precursor solution without any addition of water as discussed in 7.3.1. Taking into account that the precursor solutions exhibited slightly acidic pH (pH of ~6), a protonation of the amino groups may probably occur since ammonium salts are generally known to be extremely hygroscopic [200]. Hence, boc-Lys can be fixed due to the formation of weak bonds between ammonium groups and water molecules resulting in highly mobile species. Therefore, more effective nanocrystal formation can occur during the ligand-assisted precipitation.

DFT calculations were performed in order to investigate the formation of a complex between $PbBr_3^-$–boc-Lys^+–H_2O [149]. The presence of the hydrated complex was apparent from the FTIR spectra (see Figure 42) where the peak in a region of ~1680 cm^{-1} points out to the

vibration of hydrated species. Obviously, the precursor solution without any addition of water showed a sharper peak in comparison with solutions with water additions ranging from 0.4 to 32 mol. eq. with respect to $PbBr_2$. Altogether, hydration of boc-Lys causing a boc-Lys$^+$–H_2O complex formation is supposed to show a characteristic peak at ~2800 cm^{-1} [149], nevertheless, this peak is overlapped by the CH_2 vibrations in this region [190].
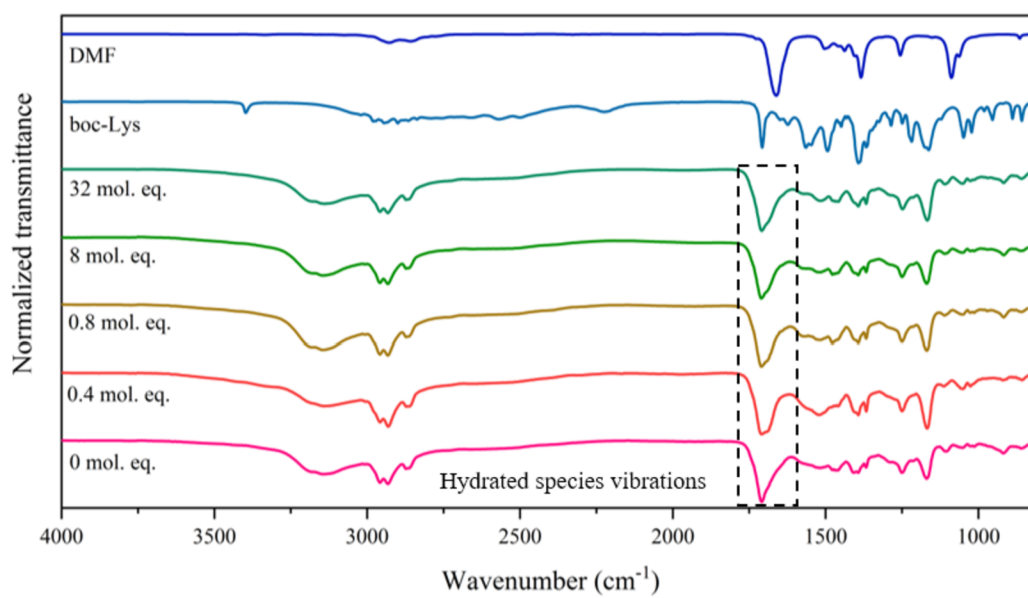
Figure 42: FTIR spectroscopy of precursor solutions containing different additions of water

To investigate the effect of the hydration of ammonium salts deeper, a precursor solution containing AdNH$_2$ (prepared in section 7.1) was prepared with an addition of 8 mol. eq. of water with respect to $PbBr_2$. Interestingly, no detectable shift of the emission maximum was observed when comparing emission spectra of AdNH$_2$ stabilized PNP prepared from precursor solutions with 0 and 8 mol. eq. of water (see in Figure 43). According to the geometry, the distance between the water molecule and the ammonium salt of the capping agent is 1.75 and 1.70 Å for the AdNH$_3^+$–H_2O and boc-Lys$^+$–H_2O complexes, respectively. This suggests that the boc-Lys-based hydrated complex is more stable than the AdNH$_2$-based one [149].
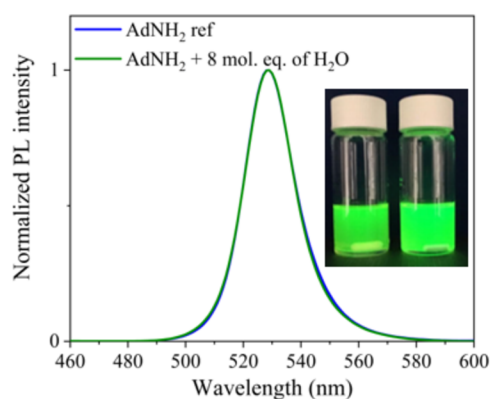
Figure 43: Emission spectra of colloidal solutions of PNP stabilized by AdNH₂ with and without addition of water into the precursor solution. Inset: corresponding photo of the samples under UV irradiation in the inset (366 nm)

In addition, XPS was employed to study PNP and the nature of the ligands binding to the nanoparticles surface. The sample for XPS was prepared from a precursor solution containing 32 mol. eq. of water with respect to PbBr$_2$. The precursor solution was precipitated in toluene in volume ratio 0.002 and the resulting material was centrifugal casted onto a glass substrate as described in section 7.1.8.

In agreement with previous experiments, Pb 4f XPS spectra showed two characteristic symmetric peaks at 138.4 eV and 143.3 eV, attributed to Pb 4f$_{7/2}$ and Pb 4f$_{5/2}$, respectively. The spin–orbit splitting was 4.86 eV, which corresponds with previously reported results [152] and [171]. In comparison with Pb 4f XPS spectra of AdNH$_2$ stabilized PNP (see in section 7.1.8), two additional peaks at 136.4 and 141.3 eV appeared. These peaks could indicate to the lead(0) rich surface of the nanoparticles [172]. On the Br 3d XPS spectrum, two peaks at 68.2 and 69.2 eV were observed. They can be attributed to Br 3d$_{5/2}$ Br 3d$_{3/2}$, respectively [172]. The N 1s XPS spectrum was deconvoluted into two peaks with centres at 400.0 and 401.8 eV indicating the presence of amide group of boc-Lys [171] and of ammonium salts of primary amine of boc-Lys [201] and of the methylammonium salt [152], respectively. It is worth noting that the presence of the only peak at 401.8 eV, which suggested the charged character of the primary ammonium group in the side chain of boc-Lys. The O 1s XPS spectrum showed two peaks at 531.8 and 533.3 eV which are attributed to the carboxylate species C=O and C–O, respectively. Finally, four peaks at 285.0, 286.1, 287.1 and 289.4 eV were deconvoluted from the C 1s XPS spectrum. The peak at 285.0 eV was assigned to C–C and C–H bonds, the next peak at 286.1 eV was attributed to the C–N bond of the amino group, the peak at 287.1 eV

proves the C–N bond of amide group and the peak at the highest binding energy of 289.4 eV, can be assigned to the C–O bond of the carboxylic acid group [173].
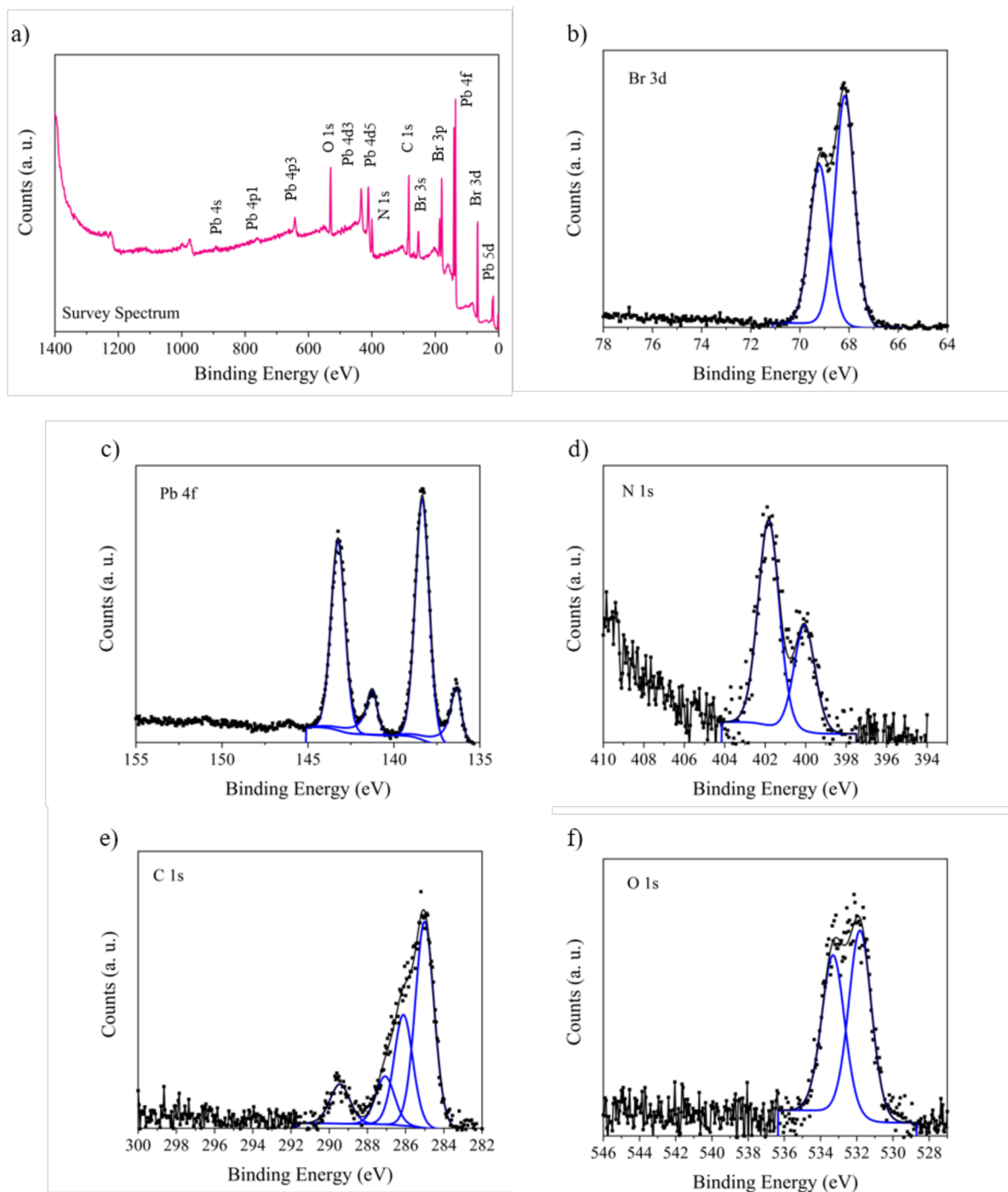
Figure 44: XPS of boc-Lys stabilized PNP which were prepared from precursor solution with an addition of water of 32 mol. eq. with respect to PbBr$_2$

7.4 Cyclic peptide for PNP stabilization

Incorporation of proteins and peptides into nanostructures paves the way for their applications into sensors and functional electrochemical and optoelectrical devices not only for biomedical applications [202]–[204]. Proteins and peptides as nature-inspired materials show selectivity and high affinity to the surfaces of a wide range of solid materials, for example metals, metal oxides, magnetic materials, semiconductors and polymers [205]–[206]. In addition, proteins and peptides are known for their self-assembly properties [207] and additional functionalization of the resulting materials [32].

As far as lysine and arginine were found to be suitable capping agents for PNP stabilization (discussed in section 7.2), oligopeptide containing lysine or arginine moieties are supposed to be suitable candidates for PNP stabilization. RGD peptides (where R: arginine, G: glycine, D: aspartic acid) have been already employed to improve biocompatibility of desired materials due to enabling cell adhesion via the RGD sequence [208]. Since, cyclic oligopeptides in general possess higher stability in comparison with their linear counterparts, we selected cyclo(RGDFK) pentapeptide which contains arginine, glycine, aspartic acid, phenylalanine and lysine, see chemical structure in Figure 45. Cyclo(RGDFK) peptide possesses both lysine and arginine moieties which can be employed in PNP stabilization. Also cyclo(RGDFK) is soluble in DMSO which is an appropriate solvent for PNP precursor solution preparation (as discussed in section 7.1.1). PNP stabilized by the cyclo(RGDFK) peptide were prepared and their properties studied, summarized in a publication by A. Jancik Prochazkova *et al.* [150].
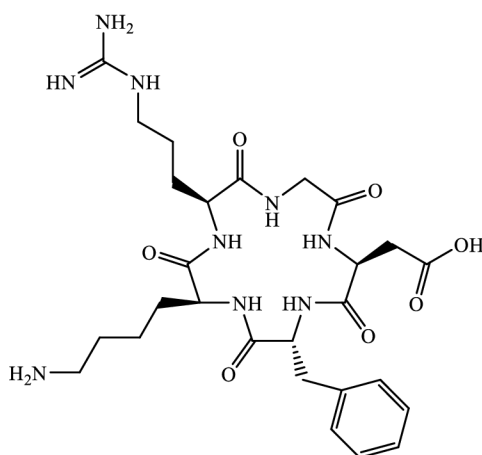
Figure 45: Chemical structure of cyclo(RGDFK) pentapeptide employed for PNP stabilization

Here, a precursor solution was prepared in DMSO because of the solubility of the cyclo(RGDFK) in this solvent. The ratio of precursor chemicals was kept the same as in previous experiments (1:1.1:9.5 for $PbBr_2$, MABr and HeA) while the amount of cyclo(RGDFK) was varied from 0.4 to 1.0 to evaluate an optimal concentration. The colloidal solutions were prepared by precipitating the precursor solutions in toluene or in chloroform in volume ratio of 0.002. Interestingly, a weak emission under UV lamp was observed in case of toluene colloidal solutions, whereas the chloroform colloidal solution exhibited a stronger emission. It was assumed that chloroform as more polar solvent dispersed the perovskite nanoparticles decorated with oligopeptide moieties on its surface more efficiently.

Chloroform colloidal solutions prepared from the precursor solutions with an amount of 0.4 and 0.6 mol. eq. of cyclo(RGDFK) with respect to $PbBr_2$ exhibited green emission under UV irradiation and emission maxima were positioned at 514 and 515 nm with PLQY of 2 and 20%, respectively. No colour change was detected when precipitating precursor solution with 1.0 mol. eq. of cyclo(RGDFK) with respect to $PbBr_2$. Therefore, as an optimal amount of cyclo(RGDFK) was 0.6 mol. eq. with respect to $PbBr_2$. The optical properties of the resulting colloidal solution are shown in Figure 46a.

For the evaluation of the nanoparticles morphology, PNP were studied by TEM. A typical TEM image is shown in Figure 46b, that shows a collection of particles with an average diameter of 6±2 nm. Taking into account the bright dots observed on the corresponding Fourier transform (FFT) pattern, a highly defined crystalline planes on TEM images can be observed, thus the samples were highly crystalline.
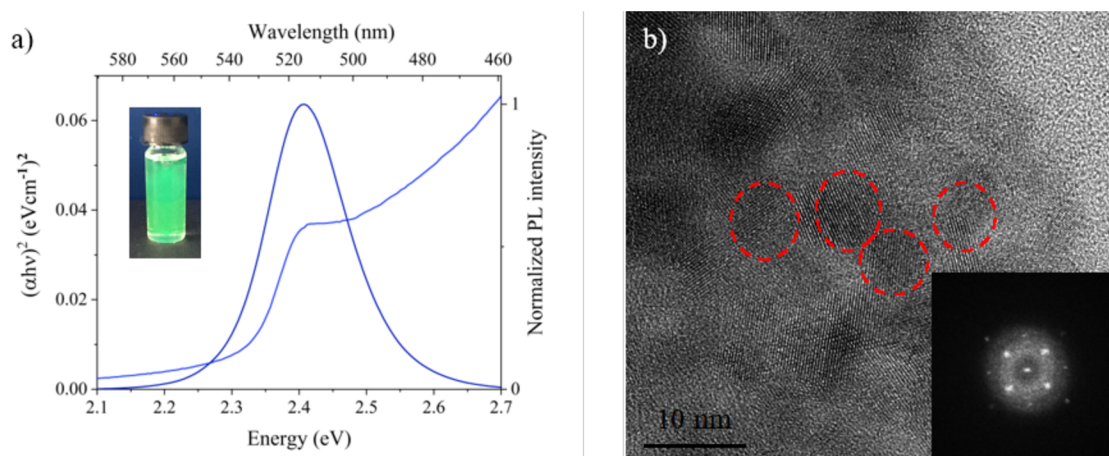
Figure 46: PNP stabilized by cyclo(RGDFK) peptide, a) optical characterization and the photo of the corresponding chloroform-based colloidal solution under UV irradiation in the inset and b) TEM image of the nanoparticles with a FFT image in the inset

To investigate whether the cyclo(RGDFK) is preferably bound to the lead bromide during the complex formation via primary amine of lysine moiety of guanidyl group of arginine moiety, DFT calculations were performed [150]. According to the calculation, Gibbs free energy of the complex of lead bromide and primary amine of the lysine moiety was about 0.39 eV lower than the energy of the complex formed between lead bromide and guanidyl group of the arginine moiety. That calculation was supported by recording the FTIR spectrum of the precursor solution containing 0.6 mol. eq. of cyclo(RGDFK) with respect to $PbBr_2$ (Figure 47). The modelled spectra (shown in the original paper [150]) predicted a sharp peak in the region of 3200 cm^{-1} as an evidence of the interaction between ammonium ion from the lysine moiety and lead bromide. This signal was indeed detected in the FTIR spectrum (see in Figure 47). The spectrum also revealed a typical broad signal in the region 2900–3300 cm^{-1} which is characteristic for perovskite structure. In addition, C–H rocking bonds from methylammonium ions were detected at 1010 and 945 cm^{-1} [175]–[176] and [189]. Furthermore, a characteristic signal of peptide bond was revealed in the region 1650 cm^{-1} (C=O stretching) and 1530 cm^{-1} (N–H bending) [209] indicating to the presence of cyclo(RGDFK).
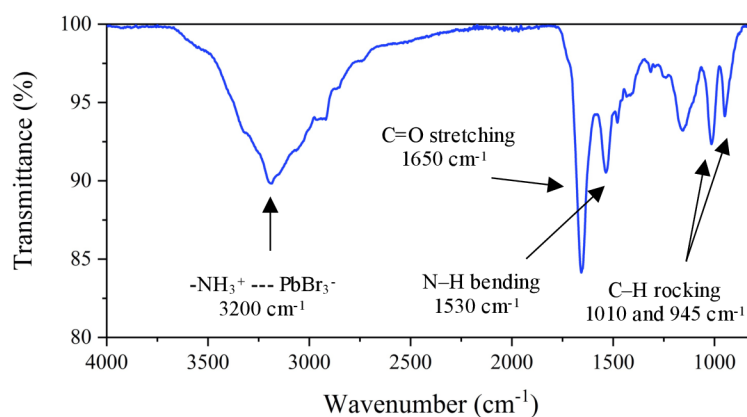
Figure 47: FTIR spectrum of DMSO-based precursor solution containing cyclo(RGDFK) pentapeptide as capping agent

Regarding the PLQY of the chloroform colloidal solution, it was determined to be ca 20%, which was significantly lower than previously prepared nanoparticles. This low PLQY could be caused by quenching properties of chloroform as discussed in section 7.2.1. Furthermore, the colloidal solutions prepared from DMSO-based precursor solution exhibited lower PLQY with comparison to their counterparts prepared from DMF-based precursor solution (discussed in section 7.1.1). Nevertheless, lower values of PLQY could be also attributed to electron

transfer between PNP and the capping agents. Hence, the electron density distribution of the cyclo(RGDFK)-NH_3^+–$PbBr_3^-$ complex was modelled [150]. The highest occupied molecular orbital (HOMO) is supposed to be localized at the guanidyl group in the ground state. However, the lowest unoccupied molecular orbital (LUMO) was displaced at the $PbBr_3^-$. Therefore, it was assumed that the charge carriers generated during the photo excitation can be transferred between the nanoparticle and the capping agents and thus causing the drop in the PLQY.

7.5 Peptide nucleic acids stabilized PNP

Peptide nucleic acid (PNA) is an artificial oligomer which was synthesized in order to mimic DNA/RNA in 1991 by P. E. Nielsen and co-workers [210]. PNA contains the same purine and pyrimidine bases attached to its backbone as DNA or RNA. In addition, thanks to N-(2-aminoethyl)-glycine backbone linked by amide bonds, the distances between neighbouring purine or pyrimidine bases are the same as in the case of DNA or RNA. This gives an opportunity to form complementary pairs not only between PNA-PNA, but also between PNA-DNA or PNA-RNA. In addition, lack of phosphate groups in the PNA structure removes a negative charge among the PNA chain and thus, the PNA-DNA or PNA-RNA complex is bound even stronger than in the case of binding only DNA-DNA or RNA-RNA. And finally, replacing sugar and phosphate groups by N-(2-aminoethyl)-glycine units along the backbone gives PNA oligomers a better stability over a broader pH range and a resistance to degradation by enzymes [211]–[212]. For that reason, PNA is usually used in molecular biology procedures, diagnostic assays or antisense therapies. However, apart from bio-molecular applications, PNA has recently attracted a considerable attention because of charge transfer in PNA-metal complexes [213], the self-assembly properties of PNA layers [214] and the formation of PNA/DNA ensembles from the charge transfer point of view [215].

Bearing in mind these features, PNA was evaluated to be a suitable capping agent for PNP stabilization because of its primary amine in the terminal N-(2-aminoethyl)glycine unit. The use of the amino group for the perovskite crystal growth control would cause decoration of the surface of PNP by purine or pyrimidine bases available for sensing possibilities. Hence, thymine-based monomer (PNA-M) and trimer (PNA-T) of PNA (Figure 48) were synthesized by S. Gaidies from Institute of Polymer Chemistry in Johannes Kepler University Linz and they were used for PNP stabilization among HeA. The results were published by A. Jancik Prochazkova *et al.* [151].

7.5.1 Optimization of PNA stabilized PNP

PNP were prepared according to the standard procedure of the ligand-assisted precipitation method. The precursor solution was prepared by dissolving perovskite precursors $PbBr_2$ and MABr with capping agents PNA-M (the structure is demonstrated in Figure 48a) and HeA alongside, in DMF. To evaluate optimal concentration of capping agents for PNP formation, several precursor solutions containing 0.4–1.6 mol. eq. of PNA-M to $PbBr_2$ were tested.

The ratio between PbBr$_2$, MABr and HeA were kept constant at 1:1.1:9.5. The precursor solution was left to be magnetically stirred for approx. 24 hours to let the complex formation occur. The results are presented in Figure 49 and summarized in Table 12.
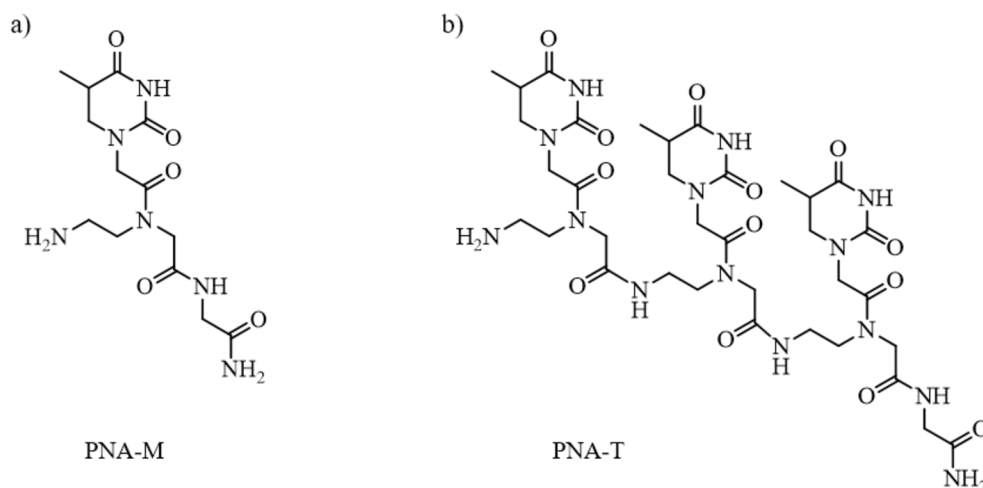
Figure 48: Chemical structure of synthesized thymine-based a) monomer and b) trimer of PNA molecule

In agreement with previously discussed results (section 7.1.7), a blue-shift of emission maxima was observed with increasing PNA-M concentration in the precursor solution. Emission maximum of 514 nm shifted to 511 nm when the amount of PNA-M was increased from 0.4 to 1.6 mol. eq. with respect to PbBr$_2$ in precursor solutions. That shift suggested a better control of the PNP growth during the precipitation. As suggested in section 7.1.7, a sufficient amount of capping agents can induce reduction of size of the resulting nanoparticles which causes a blue-shift in emission spectra.
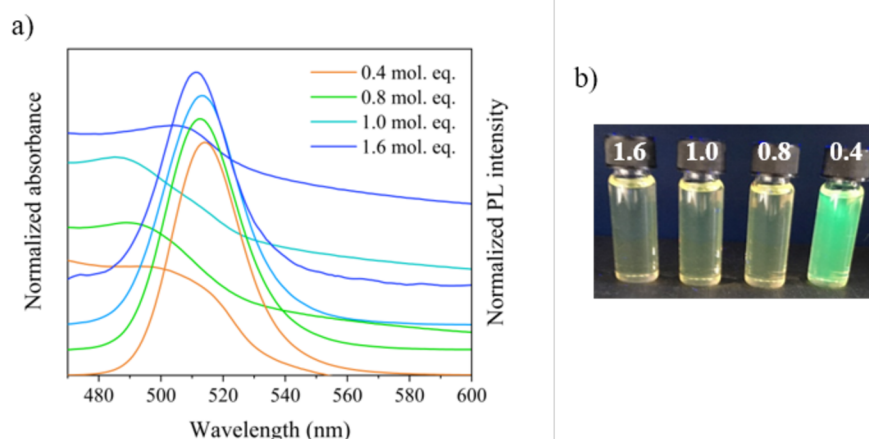
Figure 49: Optimization of concentration of the capping agents for PNA-M stabilized PNP preparation, a) optical properties of PNP prepared from the precursor solutions with different concentration of PNA-M (the concentration is presented in mol. eq. with respect to PbBr$_2$) and b) a photo of the corresponding samples under UV irradiation (366 nm)

Interestingly, the green emission was most obvious in the sample prepared from the precursor solution containing 0.4 mol. eq. of PNA-M with respect to $PbBr_2$ (see in Figure 49b). The detected PLQY was 19% whereas increasing PNA-M concentration in the precursor solution caused a significant drop of PLQY to 1% pointing out to a possible quenching effect of PNA-M capping agent.

Table 12: Optical properties of PNA-M stabilized PNP prepared from precursor solutions with different PNA-M concentration (in mol. eq. with respect to PbBr₂)

PNA-M (mol. eq.)	Emission maximum (nm)	FWHM (nm)	PLQY (%)	Band gap (eV)
0.4	514	26	19	2.33
0.8	513	28	1	2.36
1.0	513	28	1	2.35
1.6	511	26	1	2.35
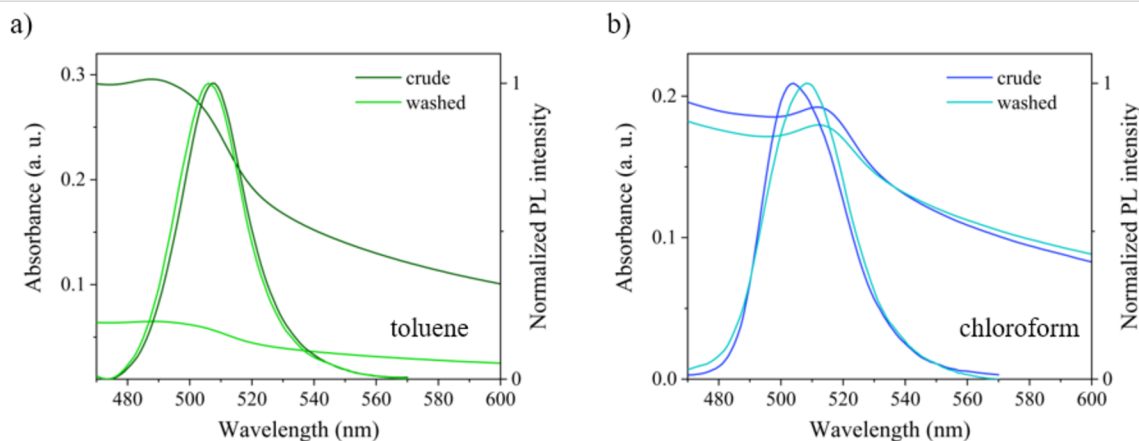
Figure 50: PNA-M stabilized PNP prepared in a) toluene and b) in chloroform and an influence of washing step on optical properties

The reproducibility of PNA-M stabilized PNP was evaluated by preparing several precursor solutions containing 0.8 mol. eq. of PNA-M with respect to $PbBr_2$. An average emission maximum was obtained of 510±3 nm and a PLQY was of 2±1%. The optical band gap was of 2.36±1 eV demonstrating a good reproducibility of PNA-M stabilized PNP.

In addition, chloroform as a precipitation medium was tested. Simultaneously, a washing procedure was performed for both toluene and chloroform colloidal solutions in order to evaluate the influence of purification procedure on the resulting optical properties (Figure 50

102

and Table 13). The use of chloroform as a precipitation medium was observed not to cause any significant change in emission maximum neither in PLQY. The emission maximum appeared at 505 nm and PLQY was 2%. Nevertheless, FWHM increased about 5 nm with comparison to the emission spectrum of the toluene-based colloidal solution which suggested a possible broadening of size distribution of PNP. In addition, a non-symmetrical emission spectrum of PNA-M stabilized PNP prepared in chloroform (Figure 50b, dark blue line) suggested the non-homogeneous size distribution. This observation was in agreement with a previous experiment proposing that the ligand-assisted precipitation technique can be optimized according to the general rules valid for any combination of capping agents.

Table 13: Dependence of washing procedure on the optical properties of PNA-M stabilized PNP

Solvent	Treatment	Emission maximum (nm)	FWHM (nm)	PLQY (%)	Band gap (eV)
Toluene	crude	508	25	1	2.37
	washed	507	25	3	2.37
Chloroform	crude	505	30	2	2.32
	washed	508	31	2	2.31

Considering the influence of washing steps on the resulting optical properties, there was not observed any significant difference between crude and washed colloidal solutions prepared neither in toluene nor in chloroform (Table 13). Nevertheless, considering quite low PLQY obtained from the PNA-M stabilized PNP (~1%), the additional lowering of PLQY due to the purification (as discussed in 7.1.3) was not easy to detect here.

Subsequently, PNA-T was used as a capping agent for PNP stabilization. For that, toluene- and chloroform-based colloidal solutions were prepared from precursor solutions containing 0.4–1.2 mol. eq. of PNA-T with respect to $PbBr_2$. (Figure 51 and Table 14). Interestingly, the precursor solution with 1.2 mol. eq. of PNA-T did not form a colloidal solution neither in toluene nor in chloroform (Figure 51a and b, respectively). As expected, the use of chloroform instead of toluene as a precipitation medium caused a blue-shift in emission spectra of about 16 nm for the sample prepared from a precursor solution containing 0.8 mol. eq. of PNA-T with respect to $PbBr_2$. This observation was in agreement with results from sections 0 and 7.2.1. It is worth noting that the chloroform-based colloidal solution prepared from a precursor solution

containing 0.8 mol. eq. of PNA-T with respect to $PbBr_2$ exhibited weak emission and absorption as shown in a photo in Figure 51b. Therefore, toluene was evaluated to be a better precipitation medium for PNA-T stabilized PNP preparation.
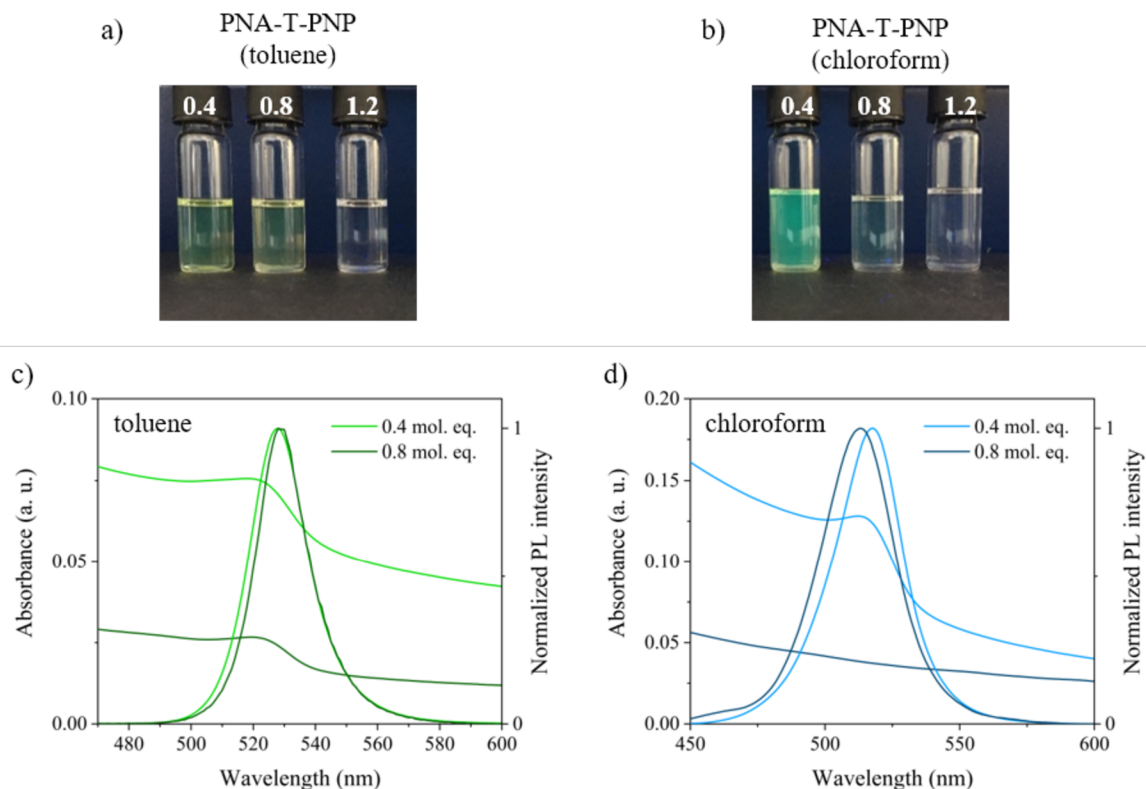
Figure 51: Optimization of capping agents concentration for PNA-T stabilized PNP preparation, a) and b) photos of colloidal solutions with different PNA-T concentration (in mol. eq. with respect to $PbBr_2$) in toluene and chloroform, respectively, under UV irradiation and c), d) corresponding UV-Vis and PL spectra

In agreement with the results from PNA-M-based PNP, PLQY dropped with increasing the concentration of PNA-T in precursor solutions (Table 14). Surprisingly, a negligible red-shift from 528 to 529 nm (see also in Figure 51c) occurred in a toluene-based sample when the concentration of PNA-T was increased from 0.4 to 0.8 mol. eq., respectively. Considering the bulkier nature of PNA-T with comparison to PNA-M, steric hindrance effects between neighbouring PNA-T capping agents on the PNP surface could take place. Hence, the concentration of PNA-T was adjusted to 0.4 mol. eq. with respect to $PbBr_2$ in precursor solutions for further studies.

104

Table 14: Optical properties of PNA-M stabilized PNP prepared from precursor solutions with different concentration of PNA-M (in mol. eq. with respect to PbBr₂)

Solvent	PNA-T (mol. eq.)	Emission maximum (nm)	FWHM (nm)	PLQY (%)	Band gap (eV)
Toluene	0.4	528	23	12	2.30
	0.8	529	20	10	2.30
Chloroform	0.4	518	30	14	2.32
	0.8	513	32	-	-
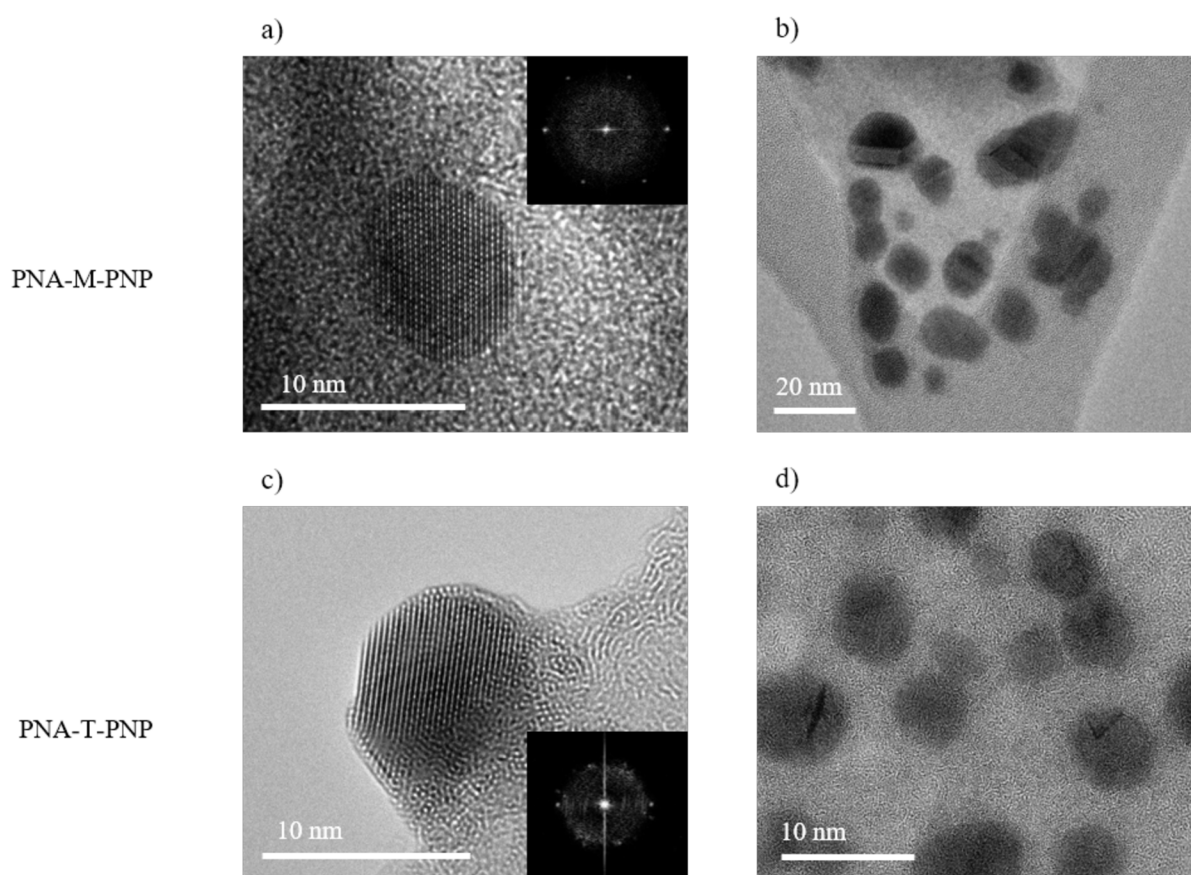
Figure 52: HRTEM images of a-b) PNA-M-PNP with an individual and a group of nanoparticles, respectively, and c-d) PNA-T-PNP with an individual and a group of nanoparticles, respectively. FFT images in insets in a) and c)

To confirm the presence of PNP in prepared samples, HRTEM images were taken for samples of PNA-M and PNA-T stabilized PNP containing 0.8 and 0.4 mol. eq. of capping agents with respect to PbBr₂ in the precursor solutions, respectively. Figure 52 shows HRTEM images of both samples with apparent individual spherical shape and highly crystalline nanoparticles. The typical diameter is 9.4±2.0 and 9.5±2.3 nm for PNA-M and PNA-T

stabilized PNP, respectively, showing a broader size distribution in comparison with PNP with different capping agents. Additionally, Energy Dispersive X-Ray Analysis (EDX) was used to semiquantitatively detect the composition of the nanoparticles stabilized by PNA-T. The significant presence of bromide, lead, carbon, oxygen and nitrogen coming from the perovskites and PNA structures was successfully confirmed. In addition, all mentioned elements were approximately homogeneously distributed (see Figure 53). Figure 53f shows a merged image where a red colour rich area indicates high concentration of Pb. Lead(0)-rich surface was already observed in case of boc-Lys stabilized PNP where XPS analysis was performed (see in section 7.3.5).
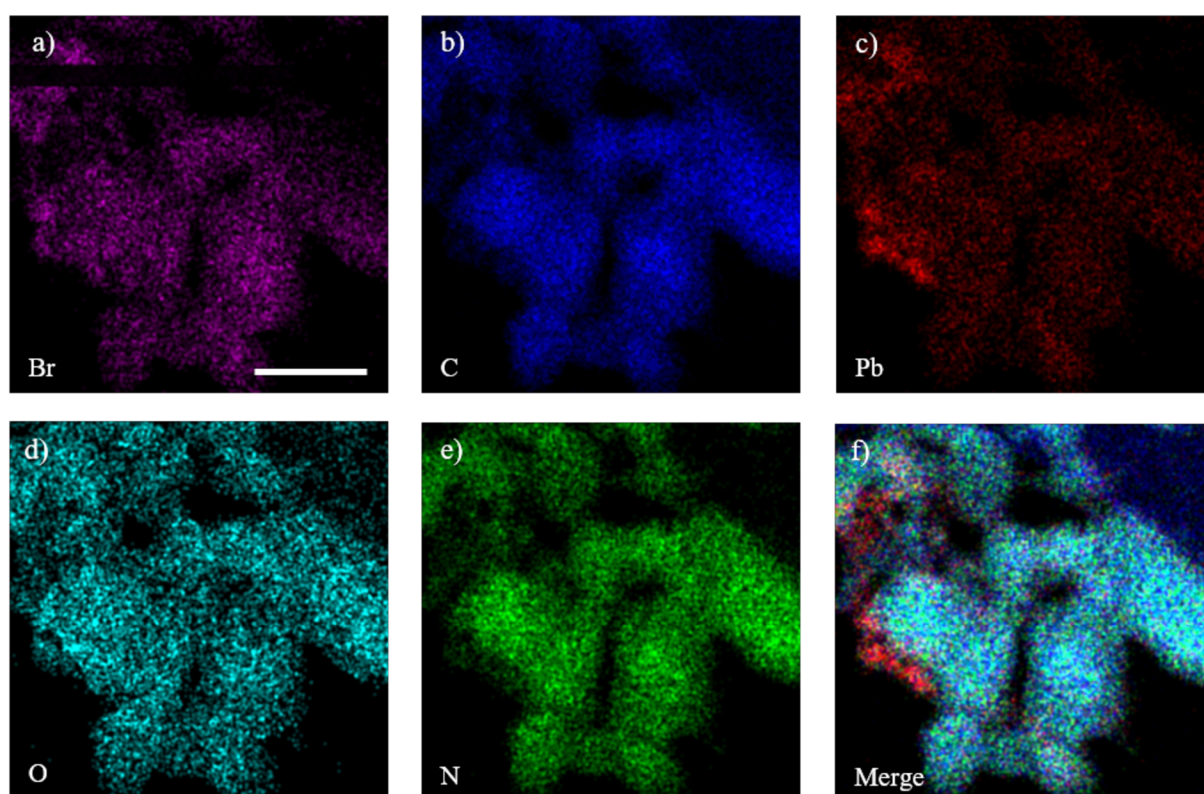
Figure 53: HRTEM-EDS images from elemental mapping of sample PNA-T-PNP, scale bar 100 nm

Finally, the perovskite-like structure was verified by powder XRD spectroscopy in both PNA-M and PNA-T stabilized PNP comparing spectra of PNP samples and bulk $MAPbBr_3$ single crystal (spectra shown in Figure 54). Peaks corresponding to the reflections (001), (011), (111), (002), (021), (211), (220), (300) and (310) were observed at positions 14.88°, 21.11°, 25.93°, 30.03°, 33.68, 37.00°, 43.00°, 45.74° and 48.5°2θ, respectively. In general, the XRD patterns were in a good agreement with previously reported results and confirmed the cubic unit cell structure of the PNP [76]. The broadening of peaks for both PNP samples is attributed to the decreasing crystallite size [157].
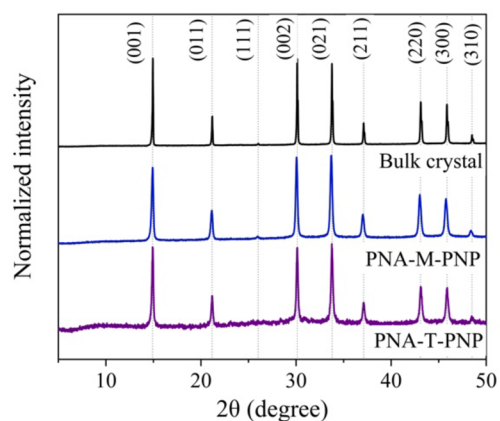
Figure 54: Powder XRD spectra of PNP stabilized by PNA-M and PNA-T and their comparison to bulk MAPbBr₃ crystal

7.5.2 PNA-PNP thin films characterization

Films of PNA stabilized PNP were prepared by centrifugal casting. In order to obtain comparable data with previous experiments, colloidal solutions were prepared by precipitating the precursor solution in toluene in volume ratio 0.002. The resulting colloidal solution of total volume 25 ml was used for the centrifugal casting of PNP onto glass substrates. The films were densely packed and seemed to be homogeneously covering the substrate, photos of the films are shown in Figure 55b and c. Nevertheless, both PNA-M-PNP and PNA-T-PNP films exhibited light scattering which indicates a rough surface. To study the morphology of the films in detail, AFM was used to determine the surface appearance of the film prepared from PNA-M-PNP (Figure 55e). The root-mean-square roughness was of 97 nm which could be an indication of the inhomogeneous overcoat assumed above.

Both samples exhibited green emission under UV irradiation with emission maxima of 519 and 531 nm for PNA-M-PNP and PNA-T-PNP films, respectively (Figure 55 and Table 15). Obviously, the emission peaks of the films were red-shifted when compared to the original colloidal solutions, assumingly due to the partial aggregation. Furthermore, the PLQY of the PNA-M-PNP and of PNA-T-PNP films were around 0.5 and 0.4%, respectively. Moreover, the PNA-M-PNP film was stored at ambient conditions and its optical stability was evaluated over the period of 32 days. As demonstrated in Figure 55d, a red shift in the emission maximum from initial 517 to 524 nm was observed suggesting a good optical stability. The shift is comparable to the shifts in already described PNP samples (section 7.3.3).

Table 15: Optical properties of films of PNA-M and PNA-T stabilized PNP

Capping agent	Emission maximum (nm)	FWHM (nm)	PLQY (%)	Band gap (eV)
PNA-M	518±1	24	~0.5	2.37
PNA-T	530±1	21	~0.4	2.29

Simultaneously, the annealing of the centrifugal casted films was tested as a post-treatment procedure and no significant change in emission spectra was observed when annealing up to 100 °C. However, samples annealed at 130 °C showed a red shift of the emission maxima up to 523 nm (from initial 518 nm) suggesting that PNP start to aggregate at high temperatures due to the dynamical surface instability.
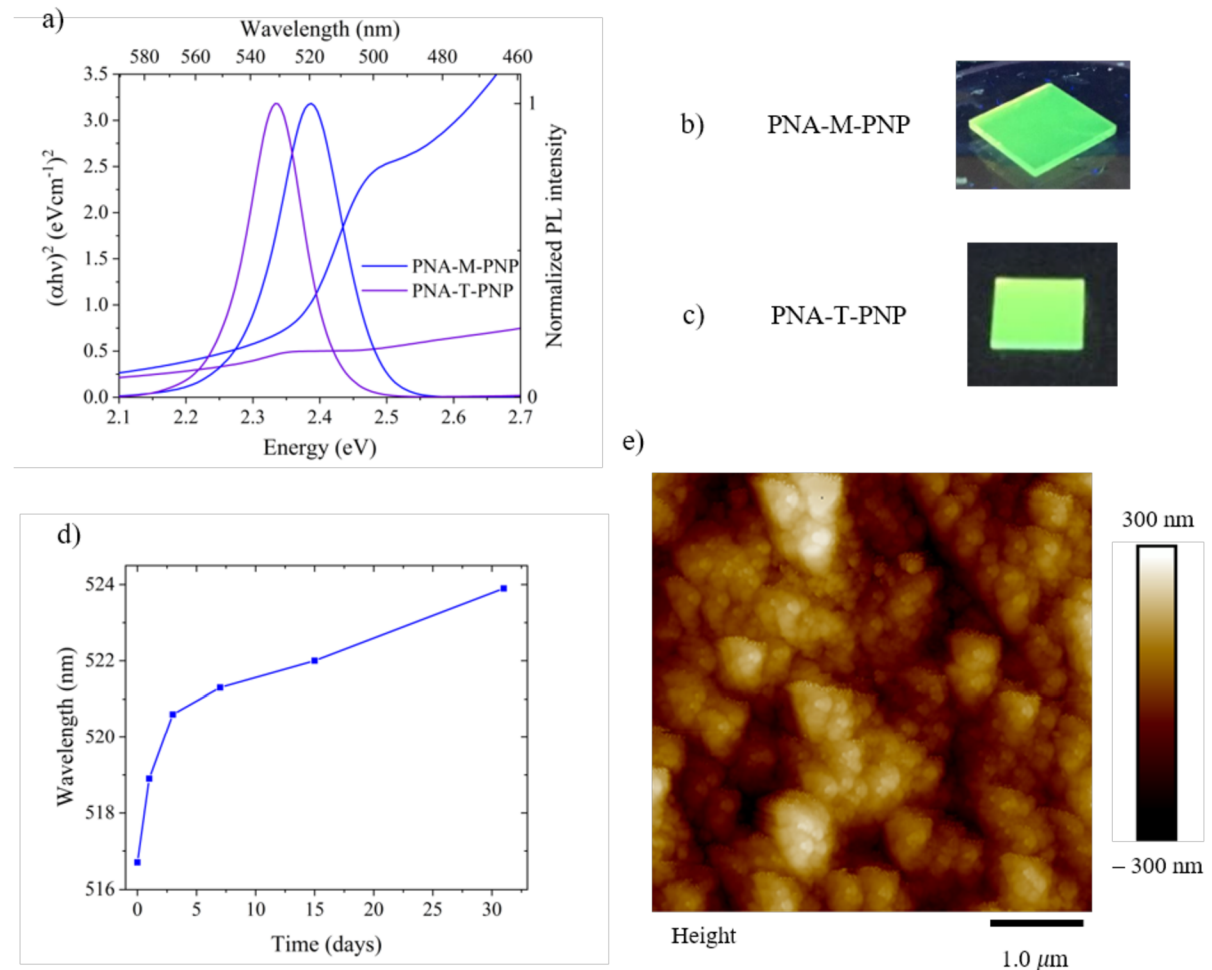
Figure 55: a) Optical properties of films of PNA-M and PNA-T stabilized PNP, b) and c) photos of the corresponding PNA-M and PNA-T stabilized PNP, respectively, under UV irradiation, d) optical stability of PNA-M-PNP film over the period of 32 days, e) AFM image of PNA-M-PNP film

In addition, emission spectra of PNA-M-PNP film were recorded at various temperatures in the range from 10 to 300 K as for AdNH$_2$ and boc-Lys stabilized PNP in sections 7.1.11 and 7.3.3. As expected, with decreasing the temperature the PL intensity increased by two orders of magnitude (Figure 56). The increase in PL intensity detected for AdNH$_2$ (Figure 26) and boc-Lys (Figure 40) stabilized PNP was only by 1.5 and 1 orders of magnitude, respectively. Hence, the increase in PL intensity and therefore the increase in PLQY could confirm the reduction of the non-radiative relaxation processes by lowering the temperature [216]. Nevertheless, changes in emission maxima and the corresponding FWHM of the spectra point out that the phase transition from cubic to tetragonal and to orthorhombic around 250 and 50 K, respectively [183].
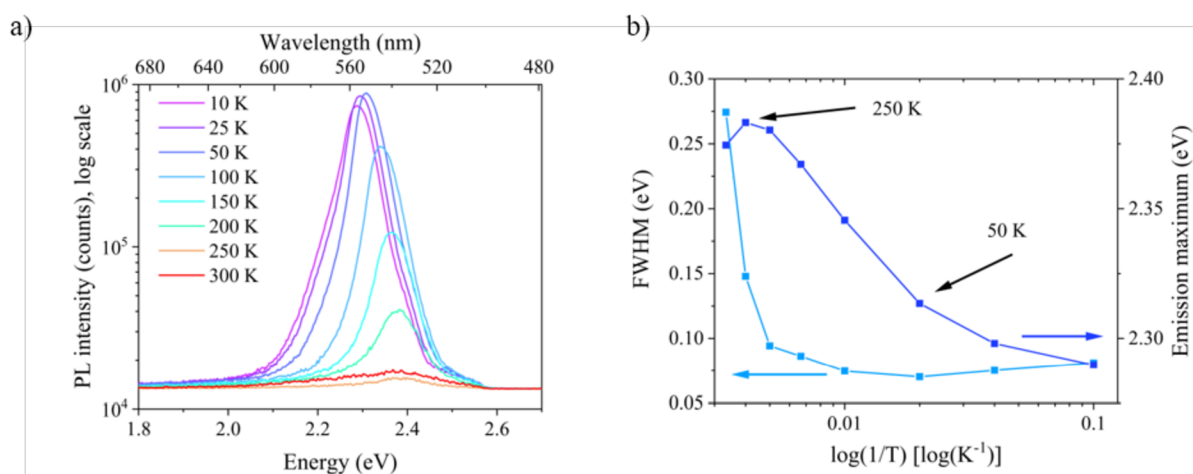
Figure 56: a) PL spectra of PNA-M-PNP film detected at different temperature, b) dependency of FWHM and emission maxima on temperature

7.5.3   PNA-M stabilized PNP for adenine sensing

PNA-M is supposed to bind to the PNP surface via primary amines. Hence, the thymine moiety should be dangling out of the nanoparticles surface being available for further interaction. Considering a possibility of charge transfer between nucleic acid and PNA [213] and [217], adenine was introduced to the colloidal solution as a complementary pair to the thymine moiety decorating the surface (schematically shown in Figure 57). The complementary pairing is realized via hydrogen bonds which can enable PL quenching by the charge transfer between the PNP surface modified with thymine moieties and adenine [218].
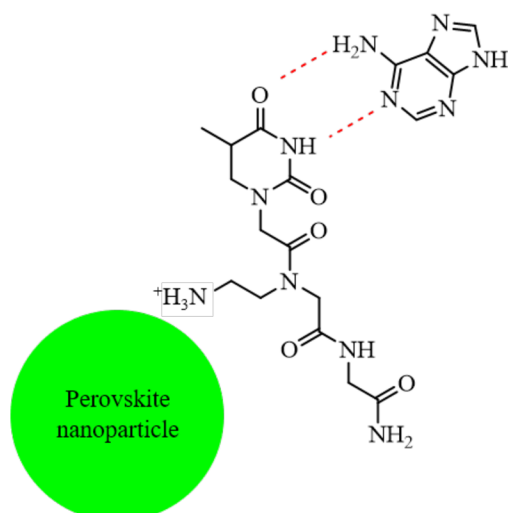
Figure 57: Binding of adenine to thymine-based monomer of PNA modified nanoparticles surface via hydrogen bonds (red dashed lines)

Therefore, adenine was added into toluene-based PNA-M-PNP colloidal solution in a defined amount to reach molar ratios of 0, 20, 60 and 100% with a respect to the amount of thymine-based PNA-M stabilizing the PNP. The solutions were left to be magnetically stirred for 5 hours to let the hydrogen bonds formation to occur. Subsequently, PL spectra of the samples were measured and the changes in PL intensity were studied (Figure 58 and Table 16). As expected, the intensity of fluorescence emission dropped significantly with the adenine addition while no notable changes in emission maxima were detected. The loading of 60% of adenine was evaluated as the limit of detection corresponding to 1.76 ppm which is comparable with other nucleic acid sensors [218].
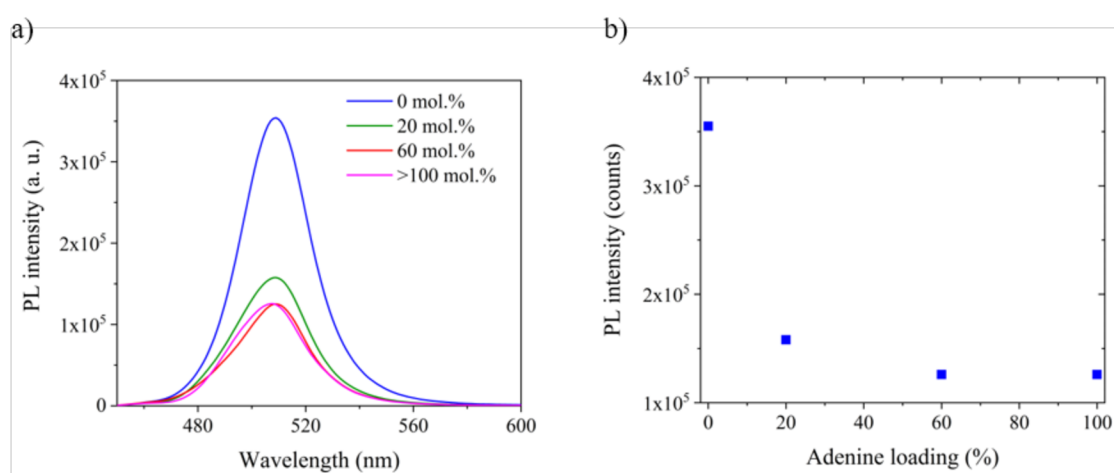
Figure 58: Adenine sensing by PNA-M-PNP, a) PL spectra with different adenine loading in the colloidal solutions and b) changes in PL intensity with increasing adenine concentration in the colloidal solution

Table 16: Optical characterization of PNA-M-PNP colloidal solution with different adenine loading

Adenine conc. (mol·dm^{-1})	Adenine loading (%)	Emission maximum (nm)	PL intensity (a. u.)
0	0	517	354 000
4.4·10^{-6}	20	517	157 000
1.3·10^{-5}	60	517	126 000
3.7·10^{-5}	100	516	126 000

DFT calculations were performed to elucidate electron density distribution in order to better understand the luminescence quenching by the addition of adenine [150]. The HOMO of the ground state was localized at the adenine molecule when considering the formation of the $PbBr_3^-$–PNA^+---adenine complex (--- stands for the suggested hydrogen bonding between thymine moiety and adenine as demonstrated in Figure 57). On the other hand, the LUMO is localized at the $PbBr_3^-$, suggesting that the photogenerated charge carriers can be transferred from the perovskite material to the surface ligands due to the dominant hole mobility in the $MAPbBr_3$ materials [219].

8 Conclusion

To summarize, a comprehensive optimization of the ligand-assisted precipitation method was initially performed for the preparation of AdNH$_2$ stabilized PNP. MAPbBr$_3$ PNP stabilized by AdNH$_2$ formed spherical and highly crystalline sub-10 nm nanoparticles in agreement with already published results [101]. It was demonstrated that there is a crucial influence of the choice of the solvent systems. The most suitable solvent for the precursor solution preparation was DMF. Simultaneously, toluene, diethylether, chloroform and chlorobenzene were evaluated as suitable precipitation media for PNP colloidal solutions preparation. The highest PLQY was detected for colloidal solutions prepared in toluene, nevertheless, the use of different solvents can broaden the applicability of these materials especially into multi-layered systems. In agreement with previous experiments [92], increasing concentration of amino-based capping agents led to the improvement of PLQY. At the same time, the growth of nanoparticles was limited with increasing amounts of capping agents due to better stabilization, hence, quantum confinement effects were observed. Moreover, it was found out that temperature selected during the precipitation has a significant effect on resulting optical properties. An optimal temperature for the ligand-assisted precipitation was found to be about 3 °C, which resulted in a formation of the most emissive colloidal solutions. Finally, different carboxylic acids as additional capping agents were tested as well as their colloidal stability. Namely, TriflacA and AcA were chosen as strong carboxylic acids, then PropA, HeA, OctA and OleicA were tested as carboxylic acids with different length of the side chain and finally, AdA was tested as a bulk-chain carboxylic acid. It was evaluated that propanoic acid alongside AdNH$_2$ induced the formation of the most emissive colloidal solutions, whereas, the use of hexanoic acid alongside AdNH$_2$ improved colloidal stability. Therefore, hexanoic acid was further employed with various amino-based capping agents.

To prove the versatility of the ligand-assisted precipitation method of PNP preparation, different amino-based capping agents were tested. For that, proteinogenic amino acids Lys and Arg were chosen as capping agents for the first time. They were attached to the PNP by their side chains in order to decorate the surface with α-amino and carboxylic groups to broaden the functionality of the resulting nanomaterials. Modifying Lys and Arg molecules by attaching boc groups to the α-amino groups led to an improvement of PLQY. Simultaneously, as formed nanoparticles grew smaller which suggested that boc-Lys and boc-Arg stabilized PNP better than their unmodified counterparts. Moreover, additions of water into the precursor solutions containing boc-Lys with HeA as capping agents facilitated the control of the PNP growth which

was described for the first time. It was assumed that water molecules improved the solubility of boc-Lys and simultaneously enhanced the mobility of the hygroscopic precursors. Hence, better complex formation within the precursor solutions was supposed to facilitate the crystal growth control during the precipitation. Indeed, changes in the dimensionality were observed with different additions of water and therefore, quantum confinement effects occurred. In addition, boc-Lys stabilized PNP were centrifugal casted onto substrates and characterized. oc-Lys stabilized PNP prepared from precursor solution with an addition of water of 32 mol. eq. with respect to $PbBr_2$ exhibited PLQY up to 93% in thin films with an acceptable optical stability over a period of 77 days. In comparison with $AdNH_2$ stabilized PNP, the films exhibited a PLQY of only 17%. The dramatic increase in PLQY could be attributed to the reduction of the traps which cause non-radiative recombination processes. Due to high PLQY, easy variability of optical properties and good optical stability, boc-Lys stabilized PNP are expected to be applicable especially in optoelectronic devices, such as LEDs, lasers and photodetectors.

As a proof-of-concept, a cyclo(RGDFK) pentapeptide was employed as a capping agent for PNP preparation. Nevertheless, peptides are known to be sensitive to the nature of their environment (temperature, pH, solvent systems, etc.). This makes their combination with perovskite materials more difficult (perovskites are sensitive to water, they are soluble in polar aprotic solvents, etc.). Besides, PNA are more abundant materials which are used in biology and sensing applications to mimic DNA/RNA. Hence, monomers and trimers of thymine-based PNA were employed during the PNP stabilization. As demonstrated, thymine moiety decorated the PNP surface and thus, being available to interact and to sense with adenine molecules via hydrogen bonding.

It is worth emphasizing that PNP stabilized by nature-inspired capping agents (such as here selected cyclo(RGDFK) and PNA) exhibited significantly lower PLQY of the resulting colloidal solutions and corresponding thin films. This behaviour was probably caused by charge transfer between perovskite nanoparticles and the capping agents decorating their surface. Therefore, these nanomaterials are not ideal for applications in light emitting devices. Nevertheless, charge transport properties and affinity to desired surfaces or analytes are required in sensing devices where the unique properties of peptides/PNA molecules (i.e. self-assembly properties, sensing abilities and affinity to desired surfaces) can be combined with perovskites to aim for those purposes.

As a result, almost 7 papers directly related to the topic of perovskite materials have been published in peer reviewed journals. The aims of this work were accomplished and the foundations of the study of perovskite nanoparticles modified with nature-inspired capping agents, such as amino acids, peptides and peptide nucleic acids, were laid. The future perspective for this class of hybrid materials is their incorporation in functional devices requiring excellent optical properties with additional self-assembly and sensing abilities. Moreover, the influence of water on the formation of perovskite nanoparticles was described for the first time. Here, the boc-Lys stabilized PNP prepared from the precursor solution with an addition of water exhibited PLQY up to 93% in thin films which predetermines them to be applied in optoelectronic devices, such as LEDs, lasers and photodetectors. An additional study revealing their anti-stokes photoluminescence was published very recently in collaboration with Linz Institute of Organic Solar Cells (LIOS) in Johannes Kepler University Linz, providing the fundamentals for their possible application in optical cooling systems [220].

9 References

[1] FEYNMAN, Richard P. There´s Plenty of Room at the Bottom. *Engineering and Science*. 1960, **23**(5), 22–36. ISSN 0013-7812.

[2] EIGLER, Donald M. and Erhard K. SCHWEIZER. Positioning single atoms with a scanning tunneling microscope. *Nature*. 1990, **344**, 524–526. ISSN 1476-4687.

[3] IRFAN, Muhammad Adeel. This is nanotechnology - one of the fastest growing markets in the world. In: *GAEU Consulting* [online]. Stockholm: GAEU Consulting, 2016 [cit. 2019-03-10]. Dostupné z: http://www.gaeu.com/item/this-is-nanotechnology-one-of-the-fastest-growing-markets-in-the-world

[4] CASE, Fiona. Nanotech decade. In: *Chemistry World* [online]. Vermont, US: Royal Society of Chemistry, 2011 [cit. 2019-03-10]. Dostupné z: www.chemistryworld.com/features/nanotech-decade/3004704.article

[5] Best Research-Cell Efficiencies. In: *NREL* [online]. Golden, 2017, 30. 10. 2017 [cit. 2020-06-22]. Dostupné z: https://www.nrel.gov/pv/cell-efficiency.html

[6] A History of Perovskite Solar Cells. In: *BCC Research* [online]. Wellesley, USA: BCC Research, 2018 [cit. 2019-03-10]. Dostupné z: www.blog.bccresearch.com/a-history-of-perovskite-solar-cells

[7] ZHANG, Feng, Haizheng ZHONG, Cheng CHEN, Xian-gang WU, Xiangmin HU, Hailong HUANG, Junbo HAN, Bingsuo ZOU and Yuping DONG. Brightly Luminescent and Color-Tunable Colloidal $CH_3NH_3PbX_3$ (X = Br, I, Cl) Quantum Dots: Potential Alternatives for Display Technology. *ACS Nano*. 2015, **9**(4), 4533–4542. DOI: 10.1021/acsnano.5b01154. ISSN 1936-0851.

[8] XING, Jun, Fei YAN, Yawen ZHAO, Shi CHEN, Huakang YU, Qing ZHANG, Rongguang ZENG, Hilmi Volkan DEMIR, Xiaowei SUN, Alfred HUAN and Qihua XIONG. High-Efficiency Light-Emitting Diodes of Organometal Halide Perovskite Amorphous Nanoparticles: Potential Alternatives for Display Technology. *ACS Nano*. 2016, **10**(7), 6623–6630. DOI: 10.1021/acsnano.6b01540. ISSN 1936-0851.

[9] RAMASAMY, Parthiban, Da-Hye LIM, Bumjin KIM, Seung-Ho LEE, Min-Sang LEE and Jong-Soo LEE. All-inorganic cesium lead halide perovskite nanocrystals for photodetector applications. *Chemical Communications*. 2016, **52**(10), 2067–2070. DOI: 10.1039/C5CC08643D. ISSN 1359-7345.

[10] WANG, Yue, Xiaoming LI, Jizhong SONG, Lian XIAO, Haibo ZENG and Handong SUN. All-Inorganic Colloidal Perovskite Quantum Dots: A New Class of Lasing Materials

with Favorable Characteristics. *Advanced Materials*. 2015, **27**(44), 7101–7108. DOI: 10.1002/adma.201503573. ISSN 09359648.

[11]   PANDA, Sayak Subhra, Howard E. KATZ and John D. TOVAR. Solid-state electrical applications of protein and peptide based nanomaterials. *Chemical Society Reviews*. 2018, **47**(10), 3640-3658. DOI: 10.1039/C7CS00817A. ISSN 0306-0012.

[12]   TAO, Kai, Pandeeswar MAKAM, Ruth AIZEN and Ehud GAZIT. Self-assembling peptide semiconductors. *Science*. 2017, **358**(6365). DOI: 10.1126/science.aam9756. ISSN 0036-8075.

[13]   ANSTAETT, Philipp and Gilles GASSER. Peptide Nucleic Acid – An Opportunity for Bio-Nanotechnology. *CHIMIA International Journal for Chemistry*. 2014, **68**(4), 264–268. DOI: 10.2533/chimia.2014.264. ISSN 00094293.

[14]   KRATOCHVÍL, Bohumil. *Základy fyziky a chemie pevných látek*. Praha: Vysoká škola chemicko-technologická v Praze, 1990. ISBN 80-708-0055-0.

[15]   RAPTA, Peter a Vladimír LUKEŠ. *Organické materiály pro elektroniku, Optoelektroniku a senzoriku*. STU, 2011. ISBN 978-80-227-3617-6.

[16]   KITTEL, Charles. *Úvod do fyziky pevných látek*. Praha: Academia, 1985.

[17]   KOOLE, Rolf, Esther GROENEVELD, Daniel VANMAEKELBERGH, Andries MEIJERINK and Celso DE MELLO DONEGÁ. Size Effects on Semiconductor Nanoparticles. *Nanoparticles*. Berlin, Heidelberg: Springer Berlin Heidelberg, 2014, 13–51. DOI: 10.1007/978-3-662-44823-6_2. ISBN 978-3-662-44822-9.

[18]   GONZÁLEZ-CARRERO, Soranyel and Julia PÉREZ-PRIETO. Colloidal photoemissive nanoparticles. *ChemTexts*. 2018, **4**(3). DOI: 10.1007/s40828-018-0063-2. ISSN 2199-3793.

[19]   SURESH, Sadadevan. Semiconductor Nanomaterials, Methods and Applications: A Review. *Nanoscience and Nanotechnology*. 2013, **3**(3), 62–74. DOI: 10.5923/j.nn.20130303.06. ISSN 2163-2588.

[20]   TAMIRAT, Y. The Role of Nanotechnology in Semiconductor Industry: Review Article. *Journal of Materials Science & Nanotechnology*. 2017, **2**(5). DOI: 10.15744/2348-9812.5.202.ISSN 2348-9812.

[21]   ALIVISATOS, A. P. Semiconductor Clusters, Nanocrystals, and Quantum Dots. *Science*. 1996, **271**(5251), 933–937. DOI: 10.1126/science.271.5251.933. ISSN 0036-8075.

[22]   SYTNYK, Mykhailo, Eric Daniel GŁOWACKI, Sergii YAKUNIN, Gundula VOSS, Wolfgang SCHÖFBERGER, Dominik KRIEGNER, Julian STANGL, Rinaldo TROTTA,

Claudia GOLLNER, Sajjad TOLLABIMAZRAEHNO, Giuseppe ROMANAZZI, Zeynep BOZKURT, Marek HAVLICEK, Niyazi Serdar SARICIFTCI and Wolfgang HEISS. Hydrogen-Bonded Organic Semiconductor Micro- And Nanocrystals: From Colloidal Syntheses to (Opto-)Electronic Devices. *Journal of the American Chemical Society*. 2014, **136**(47), 16522–16532. DOI: 10.1021/ja5073965. ISSN 0002-7863.

[23] LI, Jinghong and Jin Z. ZHANG. Optical properties and applications of hybrid semiconductor nanomaterials. *Coordination Chemistry Reviews*. 2009, **253**(23-24), 3015–3041. DOI: 10.1016/j.ccr.2009.07.017. ISSN 00108545.

[24] HEINZ, Hendrik, Chandrani PRAMANIK, Ozge HEINZ, Yifu, DING, Ratan K. MISHRA, Delphine MARCHON, Robert J. FLATT, Irina ESTRELA-LOPIS, Jordi LLOP, Sergio MOYA and Ronald F. ZIOLO. Nanoparticle decoration with surfactants: Molecular interactions, assembly, and applications. *Surface Science Reports*. 2017, **72**(1), 1–58. DOI: 10.1016/j.surfrep.2017.02.001. ISSN 01675729.

[25] ZHOU, Min and Indraneel GHOSH. Quantum dots and peptides: A bright future together. *Biopolymers*. 2007, **88**(3), 325–339. DOI: 10.1002/bip.20655. ISSN 00063525.

[26] DAVE, Nikunj a Tejas JOSHI. A Concise Review on Surfactants and Its Significance. *International Journal of Applied Chemistry*. 2017, **13**(3), 663–672. ISSN 0973-1792.

[27] COLLINS, Gillian, Fionán DAVITT, Colm O'DWYER and Justin D. HOLMES. Comparing Thermal and Chemical Removal of Nanoparticle Stabilizing Ligands: Effect on Catalytic Activity and Stability. *ACS Applied Nano Materials*. 2018, **1**(12), 7129–7138. DOI: 10.1021/acsanm.8b02019. ISSN 2574-0970.

[28] BUSSERON, Eric, Yves RUFF, Emilie MOULIN and Nicolas GIUSEPPONE. Supramolecular self-assemblies as functional nanomaterials. *Nanoscale*. 2013, **5**(16). DOI: 10.1039/c3nr02176a. ISSN 2040-3364.

[29] BAUMANN, Verena, Madathumpady Abubaker HABEEB MUHAMMED, Adam J. BLANCH, Priyanka DEY and Jessica RODRÍGUEZ-FERNÁNDEZ. Biomolecules in Metal and Semiconductor Nanoparticle Growth. *Israel Journal of Chemistry*. 2016, **56**(4), 195–213. DOI: 10.1002/ijch.201500031. ISSN 00212148.

[30] SAPSFORD, Kim, Thomas PONS, Igor MEDINTZ and Hedi MATTOUSSI. Biosensing with Luminescent Semiconductor Quantum Dots. *Sensors*. 2006, **6**(8), 925–953. DOI: 10.3390/s6080925. ISSN 1424-8220.

[31] MAXWELL, Tyler, Maria Gabriela NOGUEIRA CAMPOS, Stephen SMITH, Mitsushita DOOMRA, Zon THWIN and Swadeshmukul SANTRA. Quantum Dots.

Nanoparticles for Biomedical Applications. *Elsevier*, 2020, 2020, 243–265. DOI: 10.1016/B978-0-12-816662-8.00015-1. ISBN 9780128166628.

[32]   SEELAJAROEN, Hathaichanok, Aristides BAKANDRITSOS, Michal OTYEPKA, Radek ZBOŘIL and Niyazi Serdar SARICIFTCI. Immobilized Enzymes on Graphene as Nanobiocatalyst. *ACS Applied Materials & Interfaces*. 2019, **12**(1), 250–259. DOI: 10.1021/acsami.9b17777. ISSN 1944-8244.

[33]   SMITH, Andrew M., Hongwei DUAN, Aaron M. MOHS and Shuming NIE. Bioconjugated quantum dots for in vivo molecular and cellular imaging. *Advanced Drug Delivery Reviews*. 2008, **60**(11), 1226–1240. DOI: 10.1016/j.addr.2008.03.015. ISSN 0169409X.

[34]   GŁOWACKI, E. D., R. R. TANGORRA, H. COSKUN, D. FARKA, A. OPERAMOLLA, Y. KANBUR, F. MILANO, L. GIOTTA, G. M. FARINOLA and N. S. SARICFTCI. Bioconjugation of hydrogen-bonded organic semiconductors with functional proteins. *Journal of Materials Chemistry C*. 2015, **3**(25), 6554–6564. DOI: 10.1039/C5TC00556F. ISSN 2050-7526.

[35]   THAKOR, A. S., J. V. JOKERST, P. GHANOUNI, J. L. CAMPBELL, E. MITTRA and S. S. GAMBHIR. Clinically Approved Nanoparticle Imaging Agents. *Journal of Nuclear Medicine*. 2016, **57**(12), 1833–1837. DOI: 10.2967/jnumed.116.181362. ISSN 0161-5505.

[36]   CARE, Andrew, Peter L. BERGQUIST and Anwar SUNNA. Solid-binding peptides: smart tools for nanobiotechnology. *Trends in Biotechnology*. 2015, **33**(5), 259–268. DOI: 10.1016/j.tibtech.2015.02.005. ISSN 01677799.

[37]   DEWI, Melissa R., Geoffry LAUFERSKY and Thomas NANN. A highly efficient ligand exchange reaction on gold nanoparticles: preserving their size, shape and colloidal stability. *RSC Adv*. 2014, **4**(64), 34217–34220. DOI: 10.1039/C4RA05035E. ISSN 2046-2069.

[38]   MA, Quanbao, Xun FANG, Junting ZHANG, Lili ZHU, Xiabing RAO, Qi LU, Zhijun SUN, Huan YU and Qunlin ZHANG. Discrimination of cysteamine from mercapto amino acids through isoelectric point-mediated surface ligand exchange of β-cyclodextrin-modified gold nanoparticles. *Journal of Materials Chemistry B*. 2020, **8**(18), 4039–4045. DOI: 10.1039/D0TB00462F. ISSN 2050-750X.

[39]   MAMEDOVA, Nataliya N., Nicholas A. KOTOV, Andrey L. ROGACH and Joe STUDER. Albumin−CdTe Nanoparticle Bioconjugates: Preparation, Structure, and

Interunit Energy Transfer with Antenna Effect. Nano Letters. 2001, **1**(6), 281–286. DOI: 10.1021/nl015519n. ISSN 1530-6984.

[40]   DJALALI, Ramin, Yung-fou CHEN and Hiroshi MATSUI. Au Nanocrystal Growth on Nanotubes Controlled by Conformations and Charges of Sequenced Peptide Templates. *Journal of the American Chemical Society.* 2003, **125**(19), 5873–5879. DOI: 10.1021/ja0299598. ISSN 0002-7863.

[41]   HEDDLE, Jonathan. Protein cages, rings and tubes: useful components of future nanodevices? *Nanotechnology, Science and Applications.* 2008, **1**, 67–78. DOI: 10.2147/NSA.S4092. ISSN 1177-8903.

[42]   WANG, Zidong, Jieqian ZHANG, Jonathan M. EKMAN, Paul J. A. KENIS and Yi LU. DNA-Mediated Control of Metal Nanoparticle Shape: One-Pot Synthesis and Cellular Uptake of Highly Stable and Functional Gold Nanoflowers. *Nano Letters.* 2010, **10**(5), 1886–1891. DOI: 10.1021/nl100675p. ISSN 1530-6984.

[43]   HINDS, Sean, Bradford J. TAFT, Larissa LEVIAN, Vlad SUKHOVATKIN, Chad J. DOOLEY, Marc D. ROY, Dean D. MacNEIL, Edward H. SARGENT and Shana O. KELLEY. Nucleotide-Directed Growth of Semiconductor Nanocrystals. *Journal of the American Chemical Society.* 2006, **128**, 64–65. DOI: 10.1021/ja057002+. ISSN 0002-7863.

[44]   SOTO-VERDUGO, Víctor, Horia METIU and Elisabeth GWINN. The properties of small Ag clusters bound to DNA bases. *The Journal of Chemical Physics.* 2010, **132**(19). DOI: 10.1063/1.3419930. ISSN 0021-9606.

[45]   WEN, Qiu-Lin, Jun PENG, An-Yong LIU, Yi-Lin HU, Jun WANG, Jian LING and Qiu-E. CAO. Fluorescent silver nanoclusters stabilized in guanine-enhanced DNA hybridization for recognizing different small biological molecules. *Journal of Luminescence.* 2020, **221**. DOI: 10.1016/j.jlumin.2020.117038. ISSN 00222313.

[46]   DOOLEY, Chad J., Jessica ROUGE, Nan MA, Michael INVERNALE and Shana O. KELLEY. Nucleotide-stabilized cadmium sulfide nanoparticles. *Journal of Materials Chemistry.* 2007, **17**(17). DOI: 10.1039/b616306h. ISSN 0959-9428.

[47]   NEURATH, Hans, Jesse P. GREENSTEIN, Frank W. PUTNAM and John A. ERICKSON. The Chemistry of Protein Denaturation. Chemical Reviews. 1944, **34**(2), 157–265. DOI: 10.1021/cr60108a003. ISSN 0009-2665.

[48]   CHEN, Kun, Stefan SCHÜNEMANN, Seulki SONG and Harun TÜYSÜZ. Structural effects on optoelectronic properties of halide perovskites. *Chemical Society Reviews.* 2018, **47**(18), 7045–7077. DOI: 10.1039/C8CS00212F. ISSN 0306-0012.

[49]   BABU, Ramavath, Lingamallu GIRIBABU and Surya Prakash SINGH. Recent
Advances in Halide-Based Perovskite Crystals and Their Optoelectronic Applications.
Crystal growth and design. 2018, **18**(4), 2645–2664. DOI: 10.1021/acs.cgd.7b01767. ISSN
1528-7483.

[50]   ZHANG, Qiaohui, Hungkit TING, Shiyuan WEI, Daiqiang HUANG, Cuncun WU,
Weihai SUN, Bo QU, Shufeng WANG, Zhijian CHEN and Lixin XIAO. Recent progress
in lead-free perovskite (-like) solar cells. *Materials Today Energy.* 2018, **8**, 157–165. DOI:
10.1016/j.mtener.2018.03.001. ISSN 24686069.

[51]   JACOBSSON, T. Jesper, Meysam PAZOKI, Anders HAGFELDT and Tomas
EDVINSSON. Goldschmidt's Rules and Strontium Replacement in Lead Halogen
Perovskite Solar Cells: Theory and Preliminary Experiments on $CH_3NH_3SrI_3$. *The Journal
of Physical Chemistry C.* 2015, **119**(46), 25673–25683. DOI: 10.1021/acs.jpcc.5b06436.
ISSN 1932-7447.

[52]   MITZI, D. B., C. A. FEILD, W. T. A. HARRISON and A. M. GULOY. Conducting
tin halides with a layered organic-based perovskite structure. *Nature.* 1994, **369**(6480),
467–469. DOI: 10.1038/369467a0. ISSN 0028-0836.

[53]   KOJIMA, Akihiro, Kenjiro TESHIMA, Yasuo SHIRAI and Tsutomu MIYASAKA.
Organometal Halide Perovskites as Visible-Light Sensitizers for Photovoltaic Cells.
Journal of the American Chemical Society. 2009, **131**(17), 6050–6051. DOI:
10.1021/ja809598r. ISSN 0002-7863.

[54]   LEE, M. M., J. TEUSCHER, T. MIYASAKA, T. N. MURAKAMI and H. J.
SNAITH. Efficient Hybrid Solar Cells Based on Meso-Superstructured Organometal
Halide Perovskites. *Science.* 2012, **338**(6107), 643–647. DOI: 10.1126/science.1228604.
ISSN 0036-8075.

[55]   SHA, Wei E. I., Xingang REN, Luzhou CHEN and Wallace C. H. CHOY. The
efficiency limit of $CH_3NH_3PbI_3$ perovskite solar cells. *Applied Physics Letters.* 2015,
106(22). DOI: 10.1063/1.4922150. ISSN 0003-6951.

[56]   KIM, Young-Hoon, Himchan CHO, Jin Hyuck HEO, Tae-Sik KIM, NoSoung
MYOUNG, Chang-Lyoul LEE, Sang Hyuk IM and Tae-Woo LEE. Multicolored
Organic/Inorganic Hybrid Perovskite Light-Emitting Diodes. *Advanced Materials.* 2015,
27(7), 1248–1254. DOI: 10.1002/adma.201403751. ISSN 09359648.

[57]   XING, Guichuan, Nripan MATHEWS, Swee Sien LIM, Natalia YANTARA, Xinfeng
LIU, Dharani SABBA, Michael GRÄTZEL, Subodh MHAISALKAR and Tze Chien

SUM. Low-temperature solution-processed wavelength-tunable perovskites for lasing. *Nature Materials*. 2014, **13**(5), 476–480. DOI: 10.1038/nmat3911. ISSN 1476-1122.

[58]   DONG, Rui, Yanjun FANG, Jungseok CHAE, Jun DAI, Zhengguo XIAO, Qingfeng DONG, Yongbo YUAN, Andrea CENTRONE, Xiao Cheng ZENG and Jinsong HUANG. High-Gain and Low-Driving-Voltage Photodetectors Based on Organolead Triiodide Perovskites. *Advanced Materials*. 2015, **27**(11), 1912–1918. DOI: 10.1002/adma.201405116. ISSN 09359648.

[59]   YAKUNIN, Sergii, Mykhailo SYTNYK, Dominik KRIEGNER, Shreetu SHRESTHA, Moses RICHTER, Gebhard J. MATT, Hamed AZIMI, Christoph J. BRABEC, Julian STANGL, Maksym V. KOVALENKO and Wolfgang HEISS. Detection of X-ray photons by solution-processed lead halide perovskites. *Nature Photonics*. 2015, **9**(7), 444–449. DOI: 10.1038/nphoton.2015.82. ISSN 1749-4885.

[60]   YAKUNIN, Sergii, Dmitry N. DIRIN, Yevhen SHYNKARENKO, Viktoriia MORAD, Ihor CHERNIUKH, Olga NAZARENKO, Dominik KREIL, Thomas NAUSER and Maksym V. KOVALENKO. Detection of gamma photons using solution-grown single crystals of hybrid lead halide perovskites. *Nature Photonics*. 2016, **10**(9), 585–589. DOI: 10.1038/nphoton.2016.139. ISSN 1749-4885.

[61]   WALSH, Aron. Principles of Chemical Bonding and Band Gap Engineering in Hybrid Organic–Inorganic Halide Perovskites. *The Journal of Physical Chemistry C*. 2015, **119**(11), 5755–5760. DOI: 10.1021/jp512420b. ISSN 1932-7447.

[62]   GREEN, Martin A., Yajie JIANG, Arman Mahboubi SOUFIANI and Anita HO-BAILLIE. Optical Properties of Photovoltaic Organic–Inorganic Lead Halide Perovskites. *The Journal of Physical Chemistry Letters*. 2015, **6**(23), 4774–4785. DOI: 10.1021/acs.jpclett.5b01865. ISSN 1948-7185.

[63]   GALKOWSKI, Krzysztof, Anatolie MITIOGLU, Atsuhiko MIYATA, Paulina PLOCHOCKA, Oliver PORTUGALL, Giles E. EPERON, Jacob Tse-Wei WANG, Thomas STERGIOPOULOS, Samuel D. STRANKS, Henry J. SNAITH and Robin J. NICHOLAS. Determination of the exciton binding energy and effective masses for methylammonium and formamidinium lead tri-halide perovskite semiconductors. *Energy & Environmental Science*. 2016, **9**(3), 962–970. DOI: 10.1039/C5EE03435C. ISSN 1754-5692.

[64]   STRANKS, S. D., G. E. EPERON, G. GRANCINI, Christopher MENELAOU, Marcelo J. P. ALCOCER, Tomas LEIJTENS, Laura M. HERZ, Annamaria PETROZZA and Henry J. SNAITH. Electron-Hole Diffusion Lengths Exceeding 1 Micrometer in an

Organometal Trihalide Perovskite Absorber. *Science.* 2013, **342**(6156), 341–344. DOI: 10.1126/science.1243982. ISSN 0036-8075.

[65]   XING, G., N. MATHEWS, S. SUN, S. S. LIM, Y. M. LAM, M. GRATZEL, S. MHAISALKAR and T. C. SUM. Long-Range Balanced Electron- and Hole-Transport Lengths in Organic-Inorganic $CH_3NH_3PbI_3$. *Science.* 2013, **342**(6156), 344–347. DOI: 10.1126/science.1243167. ISSN 0036-8075.

[66]   BRANDT, Riley E., Vladan STEVANOVIĆ, David S. GINLEY and Tonio BUONASSISI. Identifying defect-tolerant semiconductors with high minority-carrier lifetimes: beyond hybrid lead halide perovskites. *MRS Communications.* 2015, **5**(02), 265–275. DOI: 10.1557/mrc.2015.26. ISSN 2159-6859.

[67]   YIN, Wan-Jian, Yanfa YAN and Su-Huai WEI. Anomalous Alloy Properties in Mixed Halide Perovskites. *The Journal of Physical Chemistry Letters.* 2014, **5**(21), 3625–3631. DOI: 10.1021/jz501896w. ISSN 1948-7185.

[68]   CHEN, Yameng, Yongsheng LIU and Maochun HONG. Cation-doping matters in caesium lead halide perovskite nanocrystals: from physicochemical fundamentals to optoelectronic applications. Nanoscale. 2020. DOI: 10.1039/D0NR02922J. ISSN 2040-3364.

[69]   CHEN, Liang, Yan-Yan TAN, Zhi-Xin CHEN, Tan WANG, Shu HU, Zi-Ang NAN, Li-Qiang XIE, Yong HUI, Jing-Xin HUANG, Chao ZHAN, Su-Heng WANG, Jian-Zhang ZHOU, Jia-Wie YAN, Bing-Wie MAO and Zhong-Qun TIAN. Toward Long-Term Stability: Single-Crystal Alloys of Cesium-Containing Mixed Cation and Mixed Halide Perovskite. *Journal of the American Chemical Society.* 2019, **141**(4), 1665–1671. DOI: 10.1021/jacs.8b11610. ISSN 0002-7863.

[70]   WANI, Ab Latif, Anjum ARA and Jawed Ahmad USMANI. Lead toxicity: a review. *Interdisciplinary Toxicology.* 2015, **8**(2), 55–64. DOI: 10.1515/intox-2015-0009. ISSN 1337-9569

[71]   MIYASAKA, Tsutomu, Ashish KULKARNI, Gyu Min KIM, Senol ÖZ a Ajay K. JENA. Perovskite Solar Cells: Can We Go Organic-Free, Lead-Free, and Dopant-Free? *Advanced Energy Materials.* 2020, **10**(13), 1902500. DOI: 10.1002/aenm.201902500. ISSN 1614-6832.

[72]   KAMAT, Prashant V., Juan BISQUERT and Jillian BURIAK. Lead-Free Perovskite Solar Cells. *ACS Energy Letters.* 2017, **2**(4), 904–905. DOI: 10.1021/acsenergylett.7b00246. ISSN 2380-8195.

[73]   HONG, Kootak, Quyet Van LE, Soo Young KIM and Ho Won JANG. Low-dimensional halide perovskites: review and issues. *Journal of Materials Chemistry C.* 2018, **6**(9), 2189–2209. DOI: 10.1039/C7TC05658C. ISSN 2050-7526.

[74]   SAIDAMINOV, Makhsud I., Ahmed L. ABDELHADY, Banavoth MURALI, Erkki ALAROUSU, Victor M. BURLAKOV, Wei PENG, Ibrahim DURSUN, Lingfei WANG, Yao HE, Giacomo MACULAN, Alain GORIELY, Tom WU, Omar F. MOHAMMED and Osman M. BAKR. High-quality bulk hybrid perovskite single crystals within minutes by inverse temperature crystallization. *Nature Communications.* 2015, **6**(1). DOI: 10.1038/ncomms8586. ISSN 2041-1723.

[75]   SAIDAMINOV, Makhsud I., Ahmed L. ABDELHADY, Giacomo MACULAN and Osman M. BAKR. Retrograde solubility of formamidinium and methylammonium lead halide perovskites enabling rapid single crystal growth. *Chemical Communications.* 2015, **51**(100), 17658–17661. DOI: 10.1039/C5CC06916E. ISSN 1359-7345.

[76]   JANCIK, Jan, Anna JANCIK PROCHAZKOVA, Markus C. SCHARBER, Alexander KOVALENKO, Jiří MÁSILKO, Niyazi S. SARICIFTCI, Martin WEITER and Jozef KRAJCOVIC. Microwave-Assisted Preparation of Organo-Lead Halide Perovskite Single Crystals. *Crystal Growth & Design.* 2020, **20**(3), 1388–1393. DOI: 10.1021/acs.cgd.9b01670. ISSN 1528-7483.

[77]   YANG, Zhichun, Shasha ZHANG, Lingbo LI and Wei CHEN. Research progress on large-area perovskite thin films and solar modules. *Journal of Materiomics.* 2017, **3**(4), 231–244. DOI: 10.1016/j.jmat.2017.09.002. ISSN 23528478.

[78]   SHAO, Yuchuan, Yanjun FANG, Tao LI, Qi WANG, Qingfeng DONG, Yehao DENG, Yongbo YUAN, Haotong WEI, Meiyu WANG, Alexei GRUVERMAN, Jeffery SHIELD and Jinsong HUANG. Grain boundary dominated ion migration in polycrystalline organic–inorganic halide perovskite films. *Energy & Environmental Science.* 2016, **9**(5), 1752–1759. DOI: 10.1039/C6EE00413J. ISSN 1754-5692.

[79]   HAILEGNAW, Bekele, Getachew ADAM, Dominik WIELEND, Johannes David PEDARNIG, Niyazi Serdar SARICIFTCI and Markus Clark SCHARBER. Acetylacetone Improves the Performance of Mixed Halide Perovskite Solar Cells. *The Journal of Physical Chemistry C.* 2019, **123**(39), 23807–23816. DOI: 10.1021/acs.jpcc.9b05058. ISSN 1932-7447.

[80]   XIE, Lujia, Taiyang ZHANG and Yixin ZHAO. Stabilizing the $MAPbI_3$ perovksite via the in-situ formed lead sulfide layer for efficient and robust solar cells. *Journal of Energy Chemistry.* 2020, **47**, 62–65. DOI: 10.1016/j.jechem.2019.11.023. ISSN 20954956.

[81]   HA, Son-Tung, Rui SU, Jun XING, Qing ZHANG and Qihua XIONG. Metal halide perovskite nanomaterials: synthesis and applications. *Chemical Science*. 2017, **8**(4), 2522–2536. DOI: 10.1039/C6SC04474C. ISSN 2041-6520.

[82]   SUN, Shibin, Dan YUAN, Yuan XU, Aifei WANG and Zhengtao DENG. Ligand-Mediated Synthesis of Shape-Controlled Cesium Lead Halide Perovskite Nanocrystals via Reprecipitation Process at Room Temperature. *ACS Nano*. 2016, **10**(3), 3648–3657. DOI: 10.1021/acsnano.5b08193. ISSN 1936-0851.

[83]   DEMCHYSHYN, Stepan, Janina Melanie ROEMER, Heiko GROIß, Herwig HEILBRUNNER, Christoph ULBRICH, Dogukan APAYDIN, Anton BÖHM, Uta RÜTT, Florian BERTRAM, Günter HESSER, Markus Clark SCHARBER, Niyazi Serdar SARICIFTCI, Bert NICKEL, Siegfried BAUER, Eric Daniel GLOWACKI and Martin KALTENBRUNNER. Confining metal-halide perovskites in nanoporous thin films. *Science Advances*. 2017, **3**(8). DOI: 10.1126/sciadv.1700738. ISSN 2375-2548.

[84]   HINTERMAYR, Verena A., Alexander F. RICHTER, Florian EHRAT, Markus DÖBLINGER, Willem VANDERLINDEN, Jasmina A. SICHERT, Yu TONG, Lakshminarayana POLAVARAPU, Jochen FELDMANN and Alexander S. URBAN. Tuning the Optical Properties of Perovskite Nanoplatelets through Composition and Thickness by Ligand-Assisted Exfoliation. *Advanced Materials*. 2016, **28**(43), 9478–9485. DOI: 10.1002/adma.201602897. ISSN 09359648.

[85]   TIGUNTSEVA, E. Y., G. P. ZOGRAF, F. E. KOMISSARENKO, D. A. ZUEV, A. A. ZAKHIDOV, S. V. MAKAROV and Yuri. S. KIVSHAR. Light-Emitting Halide Perovskite Nanoantennas. *Nano Letters*. 2018, **18**(2), 1185–1190. DOI: 10.1021/acs.nanolett.7b04727. ISSN 1530-6984.

[86]   POLAVARAPU, Lakshminarayana, Bert NICKEL, Jochen FELDMANN and Alexander S. URBAN. Advances in Quantum-Confined Perovskite Nanocrystals for Optoelectronics. *Advanced Energy Materials*. 2017, **7**(16). DOI: 10.1002/aenm.201700267. ISSN 16146832.

[87]   SCHMIDT, Luciana C., Antonio PERTEGÁS, Soranyel GONZÁLEZ-CARRERO, Olga MALINKIEWICZ, Said AGOURAM, Guilermo Mínguez ESPALLARGAS, Henk J. BOLINK, Raquel E. GALIAN and Julia PÉREZ-PRIETO. Nontemplate Synthesis of $CH_3NH_3PbBr_3$ Perovskite Nanoparticles. *Journal of the American Chemical Society*. 2014, **136**(3), 850–853. DOI: 10.1021/ja4109209. ISSN 0002-7863.

[88]   TONG, Yu-Long, Ya-Wen ZHANG, Kangzhe MA, Rui CHENG, Fengxiang WANG and Su CHEN. One-Step Synthesis of FA-Directing FAPbBr$_3$ Perovskite Nanocrystals

toward High-Performance Display. *ACS Applied Materials and Interfaces.* 2018, **10**(37), 31603–31609. DOI: 10.1021/acsami.8b10366. ISSN 1944-8244.

[89]   NEDELCU, Georgian, Loredana PROTESESCU, Sergii YAKUNIN, Maryna I. BODNARCHUK, Matthias J. GROTEVENT and Maksym V. KOVALENKO. Fast Anion-Exchange in Highly Luminescent Nanocrystals of Cesium Lead Halide Perovskites (CsPbX$_3$, X = Cl, Br, I). *Nano Letters.* 2015, **15**(8), 5635–5640. DOI: 10.1021/acs.nanolett.5b02404. ISSN 1530-6984.

[90]   HASSAN, Yasser, Olivia J. ASHTON, Jong Hyun PARK, Guangru LI, Nobuya SAKAI, Bernard WENGER, Amir-Abbas HAGHIGHIRAD, Nakita K. NOEL, Myoung Hoon SONG, Bo Ram LEE, Richard H. FRIEND and Henry J. SNAITH. Facile Synthesis of Stable and Highly Luminescent Methylammonium Lead Halide Nanocrystals for Efficient Light Emitting Devices. *Journal of the American Chemical Society.* 2019, **141**(3), 1269–1279. DOI: 10.1021/jacs.8b09706. ISSN 0002-7863.

[91]   NOEL, Nakita K., Severin N. HABISREUTINGER, Bernard WENGER, Matthew T. KLUG, Maximilian T. HÖRANTNER, Michael B. JOHNSTON, Robin J. NICHOLAS, David T. MOORE and Henry J. SNAITH. A low viscosity, low boiling point, clean solvent system for the rapid crystallisation of highly specular perovskite films. *Energy & Environmental Science.* 2017, **10**(1), 145–152. DOI: 10.1039/c6ee02373h. ISSN 1754-5692.

[92]   DE ROO, Jonathan, Maria IBANEZ, Pieter GEIREGAT, Georgian NEDELCU, Willem WALRAVENS, Jorick MAES, Jose, C. MARTINS, Isabel VAN DRIESSCHE, Maksym V. KOVALENKO and Zeger HENS. Highly Dynamic Ligand Binding and Light Absorption Coefficient of Cesium Lead Bromide Perovskite Nanocrystals. *ACS Nano.* 2016, **10**(2), 2071–2081. DOI: 10.1021/acsnano.5b06295. ISSN 1936-0851.

[93]   KRIEG, Franziska, Stefan T. OCHSENBEIN, Sergii YAKUNIN, Stephanie ten BRINCK, Philipp AELLEN, Adrian SÜESS, Baptiste CLERC, Dominic GUGGISBERG, Olga NAZARENKO, Yevhen SHYNKARENKO, Sudhir KUMAR, Chih-Jen SHIH, Ivan INFANTE and Maksym V. KOVALENKO. Colloidal CsPbX$_3$ (X = Cl, Br, I) Nanocrystals 2.0: Zwitterionic Capping Ligands for Improved Durability and Stability. *ACS Energy Letters.* 2018, **3**(3), 641–646. DOI: 10.1021/acsenergylett.8b00035. ISSN 2380-8195.

[94]   KIM, Hyunki, Nicholas HIGHT-HUF, Ji-Hwan KANG, Phoebe BISNOFF, Suvin SUNDARARAJAN, Theo THOMPSON, Michael BARNES, Ryan C. HAYWARD and Todd EMRICK. Polymer Zwitterions for Stabilization of CsPbBr$_3$ Perovskite

Nanoparticles and Nanocomposite Films. *Angewandte Chemie International Edition*. 2020, **59**. DOI: 10.1002/anie.201916492. ISSN 1433-7851.

[95]   WHEELER, Lance M., Erin M. SANEHIRA, Ashley R. MARSHALL, Philip SCHULZ, Mokshin SURI, Nicholas C. ANDERSON, Jeffrey A. CHRISTIANS, Dennis NORDLUND, Dimosthenis SOKARAS, Thomas KROLL, Steven P. HARVEY, Joseph J. BERRY, Lih Y. LIN and Joseph M. LUTHER. Targeted Ligand-Exchange Chemistry on Cesium Lead Halide Perovskite Quantum Dots for High-Efficiency Photovoltaics. *Journal of the American Chemical Society*. 2018, **140**(33), 10504–10513. DOI: 10.1021/jacs.8b04984. ISSN 0002-7863.

[96]   ORTEGA, Silvia, Maria IBÁÑEZ, Yu LIU, Yu ZHANG, Maksym V. KOVALENKO, Doris CADAVID and Andreu CABOT. Bottom-up engineering of thermoelectric nanomaterials and devices from solution-processed nanoparticle building blocks. *Chemical Society Reviews*. 2017, **46**(12), 3510–3528. DOI: 10.1039/C6CS00567E. ISSN 0306-0012.

[97]   SANEHIRA, Erin M., Ashley R. MARSHALL, Jeffrey A. CHRISTIANS, Steven P. HARVEY, Peter N. CIESIELSKI, Lance M. WHEELER, Philip SCHULZ, Lih Y. LIN, Matthew C. BEARD and Joseph M. LUTHER. Enhanced mobility $CsPbI_3$ quantum dot arrays for record-efficiency, high-voltage photovoltaic cells. *Science Advances*. 2017, **3**(10). DOI: 10.1126/sciadv.aao4204. ISSN 2375-2548.

[98]   GONZALEZ-CARRERO, Soranyel, Laura FRANCÉS-SORIANO, María GONZÁLEZ-BÉJAR, Saïd AGOURAM, Raquel E. GALIAN and Julia PÉREZ-PRIETO. The Luminescence of $CH_3NH_3PbBr_3$ Perovskite Nanoparticles Crests the Summit and Their Photostability under Wet Conditions is Enhanced. *Small*. 2016, **12**(38), 5245–5250. DOI: 10.1002/smll.201600209. ISSN 16136810.

[99]   KRAJČOVIČ, Jozef, Alexander KOVALENKO, Patricie HEINRICHOVÁ, Martin VALA and Martin WEITER. Adamantyl side groups boosting the efficiency and thermal stability of organic solid-state fluorescent dyes. *Journal of Luminescence*. 2016, **175**, 94–99. DOI: 10.1016/j.jlumin.2016.02.019. ISSN 00222313.

[100]   KOVALENKO, Alexander, Cigdem YUMUSAK, Patricie HEINRICHOVA, Stanislav STRITESKY, Ladislav FEKETE, Martin VALA, Martin WEITER, Niyazi Serdar SARICIFTCI and Jozef KRAJCOVIC. Adamantane substitutions: a path to high-performing, soluble, versatile and sustainable organic semiconducting materials. *Journal of Materials Chemistry C*. 2017, **5**(19), 4716–4723. DOI: 10.1039/C6TC05076J. ISSN 2050-7526.

[101]   GONZÁLEZ-CARRERO, Soranyel, Laura MARTÍNEZ-SARTI, Michele SESSOLO, Raquel E. GALIAN and Julia PÉREZ-PRIETO. Highly photoluminescent, dense solid films from organic-capped $CH_3NH_3PbBr_3$ perovskite colloids. *Journal of Materials Chemistry C*. 2018, **6**(25), 6771–6777. DOI: 10.1039/C8TC01344F. ISSN 2050-7526.

[102]   WANG, Sangni, Furong HUANG, Liya ZHOU, Jianwu WEI, Youling XIN, Peng JIN, Zhuo CAI, Zuodong YIN, Qi PANG and Jin Zhong ZHANG. Enhanced Photoluminescence and Stability of $CH_3NH_3PbBr_3$ Perovskite Nanocrystals with Protonated Melamine. *ChemNanoMat*. 2018, **4**(4), 409–416. DOI: 10.1002/cnma.201800006. ISSN 2199692X.

[103]   LUO, Binbin, Sara Bonabi NAGHADEH, A'Lester ALLEN, Xueming LI and Jin Z. ZHANG. Peptide-Passivated Lead Halide Perovskite Nanocrystals Based on Synergistic Effect between Amino and Carboxylic Functional Groups. *Advanced Functional Materials*. 2017, **27**(6). DOI: 10.1002/adfm.201604018. ISSN 1616301X.

[104]   WANG, Sangni, Liya ZHOU, Furong HUANG, Youling XIN, Peng JIN, Qiuxia MA, Qi PANG, Yibo CHEN and Jin Zhong ZHANG. Hybrid organic–inorganic lead bromide perovskite supercrystals self-assembled with L-cysteine and their good luminescence properties. *Journal of Materials Chemistry C*. 2018, **6**(41), 10994–11001. DOI: 10.1039/C8TC03668C. ISSN 2050-7526.

[105]   ZHAO, Jinyuan, Sunan CAO, Zhi LI a Nan MA. Amino Acid-Mediated Synthesis of $CsPbBr_3$ Perovskite Nanoplatelets with Tunable Thickness and Optical Properties. *Chemistry of Materials*. 2018, **30**(19), 6737–6743. DOI: 10.1021/acs.chemmater.8b02396. ISSN 0897-4756.

[106]   DIRIN, Dmitry N., Loredana PROTESESCU, David TRUMMER, Ilia V. KOCHETYGOV, Sergii YAKUNIN, Frank KRUMEICH, Nicholas P. STADIE and Maksym V. KOVALENKO. Harnessing Defect-Tolerance at the Nanoscale: Highly Luminescent Lead Halide Perovskite Nanocrystals in Mesoporous Silica Matrixes. *Nano Letters*. 2016, **16**(9), 5866–5874. DOI: 10.1021/acs.nanolett.6b02688. ISSN 1530-6984.

[107]   WANG, Yanan, Juan HE, Hao CHEN, Jiangshan CHEN, Ruidong ZHU, Pin MA, Andrew TOWERS, Yuan LIN, Andre J. GESQUIERE, Shin-Tson WU and Yajie DONG. Ultrastable, Highly Luminescent Organic-Inorganic Perovskite-Polymer Composite Films. *Advanced Materials*. 2016, **28**(48), 10710–10717. DOI: 10.1002/adma.201603964. ISSN 09359648.

[108]   HUI, L. S., C. BESWICK, A. GETACHEW, H. HEILBRUNNER, K. LIANG, G. HANTA, R. ARBI, M. MUNIR, H. DAWOOD, N. ISIK GOKTAS, R. LaPIERRE, M. C.

SCHARBER, N. S. SARICIFTCI and A. TURAK. Reverse Micelle Templating Route to Ordered Monodispersed Spherical Organo-Lead Halide Perovskite Nanoparticles for Light Emission. *ACS Applied Nano Materials.* 2019, **2**(7), 4121–4132. DOI: 10.1021/acsanm.9b00585. ISSN 2574-0970.

[109]   TEUNIS, Meghan B., Atanu JANA, Poulami DUTTA, Merrell A. JOHNSON, Manik MANDAL, Barry B. MUHOBERAC and Rajesh SARDAR. Mesoscale Growth and Assembly of Bright Luminescent Organolead Halide Perovskite Quantum Wires. *Chemistry of Materials.* 2016, **28**(14), 5043–5054. DOI: 10.1021/acs.chemmater.6b01793. ISSN 0897-4756.

[110]   ALMEIDA, Guilherme, Luca GOLDONI, Quinten AKKERMAN, Zhiya DANG, Ali Hossain KHAN, Sergio MARRAS, Iwan MOREELS and Liberato MANNA. Role of Acid–Base Equilibria in the Size, Shape, and Phase Control of Cesium Lead Bromide Nanocrystals. *ACS Nano.* 2018, **12**(2), 1704–1711. DOI: 10.1021/acsnano.7b08357. ISSN 1936-0851.

[111]   ZHANG, Dandan, Samuel W. EATON, Yi YU, Letian DOU and Peidong YANG. Solution-Phase Synthesis of Cesium Lead Halide Perovskite Nanowires. *Journal of the American Chemical Society.* 2015, **137**(29), 9230–9233. DOI: 10.1021/jacs.5b05404. ISSN 0002-7863.

[112]   IMRAN, Muhammad, Francesco DI STASIO, Zhiya DANG, Claudio CANALE, Ali Hossain KHAN, Javad SHAMSI, Rosaria BRESCIA, Mirko PRATO and Liberato MANNA. Colloidal Synthesis of Strongly Fluorescent $CsPbBr_3$ Nanowires with Width Tunable down to the Quantum Confinement Regime. *Chemistry of Materials.* 2016, **28**(18), 6450–6454. DOI: 10.1021/acs.chemmater.6b03081. ISSN 0897-4756.

[113]   SHAMSI, Javad, Zhiya DANG, Paolo BIANCHINI, Claudio CANALE, Francesco DI STASIO, Rosaria BRESCIA, Mirko PRATO and Liberato MANNA. Colloidal Synthesis of Quantum Confined Single Crystal $CsPbBr_3$ Nanosheets with Lateral Size Control up to the Micrometer Range. *Journal of the American Chemical Society.* 2016, **138**(23), 7240–7243. DOI: 10.1021/jacs.6b03166. ISSN 0002-7863.

[114]   ZHANG, Dandan, Yiming YANG, Yehonadav BEKENSTEIN, Yi YU, Natalie A. GIBSON, Andrew B. WONG, Samuel W. EATON, Nikolay KORNIENKO, Qiao KONG, Minliang LAI, A. Paul ALIVISATOS, Stephen R. LEONE and Peidong YANG. Synthesis of Composition Tunable and Highly Luminescent Cesium Lead Halide Nanowires through Anion-Exchange Reactions. *Journal of the American Chemical Society.* 2016, **138**(23), 7236–7239. DOI: 10.1021/jacs.6b03134. ISSN 0002-7863.

[115]   AMGAR, Daniel, Avigail STERN, Dvir ROTEM, Danny PORATH and Lioz ETGAR. Tunable Length and Optical Properties of $CsPbX_3$ (X = Cl, Br, I) Nanowires with a Few Unit Cells. *Nano Letters*. 2017, **17**(2), 1007–1013. DOI: 10.1021/acs.nanolett.6b04381. ISSN 1530-6984.

[116]   ZHU, Feng, Long MEN, Yijun GUO, Qiaochu ZHU, Ujjal BHATTACHARJEE, Peter M. GOODWIN, Jacob W. PETRICH, Emily A. SMITH and Javier VELA. Shape Evolution and Single Particle Luminescence of Organometal Halide Perovskite Nanocrystals. *ACS Nano*. 2015, **9**(3), 2948–2959. DOI: 10.1021/nn507020s. ISSN 1936-0851.

[117]   AHARON, Sigalit and Lioz ETGAR. Two Dimensional Organometal Halide Perovskite Nanorods with Tunable Optical Properties. *Nano Letters*. 2016, **16**(5), 3230–3235. DOI: 10.1021/acs.nanolett.6b00665. ISSN 1530-6984.

[118]   HA, Son Tung, Xinfeng LIU, Qing ZHANG, David GIOVANNI, Tze Chien SUM and Qihua XIONG. Synthesis of Organic-Inorganic Lead Halide Perovskite Nanoplatelets: Towards High-Performance Perovskite Solar Cells and Optoelectronic Devices. *Advanced Optical Materials*. 2014, **2**(9), 838–844. DOI: 10.1002/adom.201400106. ISSN 21951071.

[119]   AKKERMAN, Quinten A., Silvia Genaro MOTTI, Ajay Ram SRIMATH KANDADA, Edoardo MOSCONI, Valerio D'INNOCENZO, Giovanni BERTONI, Sergio MARRAS, Brett A. KAMINO, Laura MIRANDA, Filippo De ANGELIS, Annamaria PETROZZA, Mirko PRATO and Liberato MANNA. Solution Synthesis Approach to Colloidal Cesium Lead Halide Perovskite Nanoplatelets with Monolayer-Level Thickness Control. *Journal of the American Chemical Society*. 2016, **138**(3), 1010–1016. DOI: 10.1021/jacs.5b12124. ISSN 0002-7863.

[120]   AHMED, Ghada H., Jun YIN, Riya BOSE, Lutfan SINATRA, Erkki ALAROUSU, Emre YENGEL, Noktan M. AlYAMI, Makhsud I. SAIDAMINOV, Yuhai ZHANG, Mohamed N. HEDHILI, Osman M. BAKR, Jean-Luc BRÉDAS and Omar F. MOHAMMED. Pyridine-Induced Dimensionality Change in Hybrid Perovskite Nanocrystals. *Chemistry of Materials*. 2017, **29**(10), 4393–4400. DOI: 10.1021/acs.chemmater.7b00872. ISSN 0897-4756.

[121]   ZHAO, Jinyuan, Sunan CAO, Zhi LI and Nan MA. Amino Acid-Mediated Synthesis of $CsPbBr_3$ Perovskite Nanoplatelets with Tunable Thickness and Optical Properties. *Chemistry of Materials*. 2018, **30**(19), 6737–6743. DOI: 10.1021/acs.chemmater.8b02396. ISSN 0897-4756.

[122]   KOH, Teck Ming, Benny FEBRIANSYAH and Nripan MATHEWS. Ruddlesden-Popper Perovskite Solar Cells. *Chem.* 2017, **2**(3), 326–327. DOI: 10.1016/j.chempr.2017.02.015. ISSN 24519294.

[123]   KULKARNI, Sneha A., Natalia YANTARA, Kim Seng TAN, Nripan MATHEWS and Subodh G. MHAISALKAR. Perovskite nanostructures: Leveraging quantum effects to challenge optoelectronic limits. *Materials Today.* 2020, 33, 122–140. DOI: 10.1016/j.mattod.2019.10.021. ISSN 13697021.

[124]   SMITH, Ian C., Eric T. HOKE, Diego SOLIS-IBARRA, Michael D. MCGEHEE and Hemamala I. KARUNADASA. A Layered Hybrid Perovskite Solar-Cell Absorber with Enhanced Moisture Stability. *Angewandte Chemie.* 2014, **126**(42), 11414–11417. DOI: 10.1002/ange.201406466. ISSN 00448249.

[125]   CAO, Duyen H., Constantinos C. STOUMPOS, Omar K. FARHA, Joseph T. HUPP and Mercouri G. KANATZIDIS. 2D Homologous Perovskites as Light-Absorbing Materials for Solar Cell Applications. *Journal of the American Chemical Society.* 2015, **137**(24), 7843–7850. DOI: 10.1021/jacs.5b03796. ISSN 0002-7863.

[126]   TSAI, Hsinhan, Wanyi NIE, Jean-Christophe BLANCON, Constantinos C. STOUMPOS, Reza ASADPOUR, Boris HARUTYUNYAN, Amanda J. NEUKIRCH, Rafael VERDUZCO, Jared J. CROCHET, Sergei TRETIAK, Laurent PEDESSEAU, Jacky EVEN, Muhammad A. ALAM, Gautam GUPTA, Jun LOU, Pulickel M. AJAYAN, Michael J. BEDZYK, Mercouri G. KANATZIDIS and Aditya D. MOHITE. High-efficiency two-dimensional Ruddlesden-Popper perovskite solar cells. *Nature.* 2016, **536**(7616), 312–317. DOI: 10.1038/nature18306. ISSN 0028-0836.

[127]   RODRÍGUEZ-ROMERO, Jesús, Bruno Clasen HAMES, Iván MORA-SERÓ and Eva M. BAREA. Conjugated Organic Cations to Improve the Optoelectronic Properties of 2D/3D Perovskites. *ACS Energy Letters.* 2017, **2**(9), 1969–1970. DOI: 10.1021/acsenergylett.7b00654. ISSN 2380-8195.

[128]   ZHANG, Taiyang, Liqiang XIE, Liang CHEN, Nanjie GUO, Ge LI, Zhongqun TIAN, Bingwei MAO and Yixin ZHAO. In Situ Fabrication of Highly Luminescent Bifunctional Amino Acid Crosslinked 2D/3D $NH_3C_4H_9COO(CH_3NH_3PbBr_3)_n$ Perovskite Films. *Advanced Functional Materials.* 2017, **27**(1). DOI: 10.1002/adfm.201603568. ISSN 1616301X.

[129]   QUAN, Li Na, Mingjian YUAN, Riccardo COMIN, Oleksandr VOZNYY, Eric M. BEAUREGARD, Sjoerd HOOGLAND, Andrei BUIN, Ahmad R. KIRMANI, Kui ZHAO, Aram AMASSIAN, Dong Ha KIM and Edward H. SARGENT. Ligand-Stabilized

Reduced-Dimensionality Perovskites. *Journal of the American Chemical Society*. 2016, **138**(8), 2649–2655. DOI: 10.1021/jacs.5b11740. ISSN 0002-7863.

[130]   GRANCINI, G., C. ROLDÁN-CARMONA, I. ZIMMERMANN, E. MOSCONI, X. LEE, D. MARTINEAU, S. NARBEY, F. OSWALD, F. De ANGELIS, M. GRAETZEL and Mohammad Khaja NAZEERUDDIN. One-Year stable perovskite solar cells by 2D/3D interface engineering. *Nature Communications*. 2017, **8**. DOI: 10.1038/ncomms15684. ISSN 2041-1723.

[131]   ZHANG, Taiyang, M. Ibrahim DAR, Ge LI, Feng XU, Nanjie GUO, Michael GRÄTZEL and Yixin ZHAO. Bication lead iodide 2D perovskite component to stabilize inorganic α-CsPbI$_3$ perovskite phase for high-efficiency solar cells. *Science Advances*. 2017, **3**(9). DOI: 10.1126/sciadv.1700841. ISSN 2375-2548.

[132]   HATTORI, Toshiaki, Takahiro TAIRA, Masanao ERA, Tetsuo TSUTSUI and Shugu SAITO. Highly efficient electroluminescence from a heterostructure device combined with emissive layered-perovskite and an electron-transporting organic compound. *Chemical Physics Letters*. 1996, **254**(1–2), 103–108. DOI: 10.1016/0009-2614(96)00310-7. ISSN 00092614.

[133]   ILIE, C. C., F. GUZMAN, B. L. SWANSON, I. R. EVANS, P. S. COSTA, J. D. TEETER, M. SHEKHIREV, N. BENKER, S. SIKICH, A. ENDERS, P. A. DOWBEN, A. SINITSKII and J. J. YOST. Inkjet printable-photoactive all inorganic perovskite films with long effective photocarrier lifetime. *Journal of Physics: Condensed Matter*. 2018, **30**(18), DOI: 10.1088/1361-68X/aab986. ISSN 0953-8984.

[134]   LING, Yichuan, Zhao YUAN, Yu TIAN, Xi WANG, Jamie C. WANG, Yan XIN, Kenneth HANSON, Biwu MA and Hanwei GAO. Bright Light-Emitting Diodes Based on Organometal Halide Perovskite Nanoplatelets. *Advanced Materials*. 2016, **28**(2), 305–311. DOI: 10.1002/adma.201503954. ISSN 09359648.

[135]   ZHANG, Qiao and Yadong YIN. All-Inorganic Metal Halide Perovskite Nanocrystals: Opportunities and Challenges. *ACS Central Science*. 2018, **4**(6), 668–679. DOI: 10.1021/acscentsci.8b00201. ISSN 2374-7943.

[136]   SONG, Jizhong, Jianhai LI, Xiaoming LI, Leimeng XU, Yuhui DONG and Haibo ZENG. Quantum Dot Light-Emitting Diodes Based on Inorganic Perovskite Cesium Lead Halides (CsPbX$_3$). *Advanced Materials*. 2015, **27**(44), 7162–7167. DOI: 10.1002/adma.201502567. ISSN 09359648.

[137]   LI, Guangru, Florencia Wisnivesky Rocca RIVAROLA, Nathaniel J. L. K. DAVIS, Sai BAI, Tom C. JELLICOE, Francisco de la PENA, Shaocong HOU, Caterina DUCATI,

Feng GAO, Richard H. FRIEND, Neil C. GREENHAM and Zhi-Kuang TAN. Highly Efficient Perovskite Nanocrystal Light-Emitting Diodes Enabled by a Universal Crosslinking Method. *Advanced Materials*. 2016, **28**(18), 3528–3534. DOI: 10.1002/adma.201600064. ISSN 09359648.

[138] LI, Jianhai, Leimeng XU, Tao WANG, Jizhong SONG, Jiawei CHEN, Jie XUE, Yuhui DONG, Bo CAI, Qingsong SHAN, Boning HAN and Haibo ZENG. 50-Fold EQE Improvement up to 6.27% of Solution-Processed All-Inorganic Perovskite $CsPbBr_3$ QLEDs via Surface Ligand Density Control. *Advanced Materials*. 2017, **29**(5). DOI: 10.1002/adma.201603885. ISSN 09359648.

[139] CHIBA, Takayuki, Keigo HOSHI, Yong-Jin PU, Yuya TAKEDA, Yukihiro HAYASHI, Satoru OHISA, So KAWATA and Junji KIDO. High-Efficiency Perovskite Quantum-Dot Light-Emitting Devices by Effective Washing Process and Interfacial Energy Level Alignment. *Applied Materials and Interfaces*. 2017, **9**(21), 18054–18060. DOI: 10.1021/acsami.7b03382. ISSN 1944-8244.

[140] ZHU, Haiming, Yongping FU, Fei MENG, Xiaoxi WU, Zizhou GONG, Qi DING, Martin V. GUSTAFSSON, M. Tuan TRINH, Song JIN and X-Y. ZHU. Lead halide perovskite nanowire lasers with low lasing thresholds and high quality factors. *Nature Materials*. 2015, **14**(6), 636–642. DOI: 10.1038/nmat4271. ISSN 1476-1122.

[141] XING, Jun, Xin Feng LIU, Qing ZHANG, Son Tung HA, Yan Wen YUAN, Chao SHEN, Tze Chien SUM and Qihua XIONG. Vapor Phase Synthesis of Organometal Halide Perovskite Nanowires for Tunable Room-Temperature Nanolasers. *Nano Letters*. 2015, **15**(7), 4571–4577. DOI: 10.1021/acs.nanolett.5b01166. ISSN 1530-6984.

[142] TIGUNTSEVA, Ekaterina Y., Denis G. BARANOV, Anatoly P. PUSHKAREV, Battulga MUNKHBAT, Filipp KOMISSARENKO, Marius FRANCKEVIČIUS, Anvar A. ZAKHIDOV, Timur SHEGAI, Yuri S. KIVSHAR and Sergey V. MAKAROV. Tunable Hybrid Fano Resonances in Halide Perovskite Nanoparticles. *Nano Letters*. 2018, **18**(9), 5522–5529. DOI: 10.1021/acs.nanolett.8b01912. ISSN 1530-6984.

[143] ZHANG, Qing, Rui SU, Xinfeng LIU, Jun XING, Tze Chien SUM and Qihua XIONG. High-Quality Whispering-Gallery-Mode Lasing from Cesium Lead Halide Perovskite Nanoplatelets. *Advanced Functional Materials*. 2016, **26**(34), 6238–6245. DOI: 10.1002/adfm.201601690. ISSN 1616301X.

[144] XU, Yang-Fan, Mu-Zi YANG, Bai-Xue CHEN, Xu-Dong WANG, Hong-Yan CHEN, Dai-Bin KUANG and Cheng-Yong SU. A $CsPbBr_3$ Perovskite Quantum Dot/Graphene

Oxide Composite for Photocatalytic CO_2 Reduction. *Journal of the American Chemical Society*. 2017, **139**(16), 5660–5663. DOI: 10.1021/jacs.7b00489. ISSN 0002-7863.

[145]   PARREY, Khursheed Ahmad, Anver AZIZ, S. G. ANSARI, Sajjad Husain MIR, Ajit KHOSLA and Asad NIAZI. Synthesis and Characterization of an Efficient Hole-Conductor Free Halide Perovskite $CH_3NH_3PbI_3$ Semiconductor Absorber Based Photovoltaic Device for IOT. *Journal of The Electrochemical Society*. 2018, **165**(8), B3023–B3029. DOI: 10.1149/2.0051808jes. ISSN 0013-4651.

[146]   HUANG, He, Andrei S. SUSHA, Stephen V. KERSHAW, Tak Fu HUNG and Andrey L. ROGACH. Control of Emission Color of High Quantum Yield $CH_3NH_3PbBr_3$ Perovskite Quantum Dots by Precipitation Temperature. *Advanced Science*. 2015, **2**(9). DOI: 10.1002/advs.201500194. ISSN 21983844.

[147]   JANCIK PROCHAZKOVA, Anna, Markus Clark SCHARBER, Cigdem YUMUSAK, Ján JANČÍK, Jiří MÁSILKO, Oliver   BRÜGGEMANN, Martin WEITER, Niyazi Serdar SARICIFTCI, Jozef KRAJČOVIČ, Yolanda SALINAS and Alexander KOVALENKO. Synthesis conditions influencing formation of MAPbBr$_3$ perovskite nanoparticles prepared by the ligand-assisted precipitation method. *Scientific Reports*. Under revision.

[148]   JANCIK PROCHAZKOVA, Anna, Stepan DEMCHYSHYN, Cigdem YUMUSAK, Jiří MÁSILKO, Oliver BRÜGGEMANN, Martin WEITER, Martin KALTENBRUNNER, Niyazi Serdar SARICIFTCI, Jozef KRAJCOVIC, Yolanda SALINAS and Alexander KOVALENKO. Proteinogenic Amino Acid Assisted Preparation of Highly Luminescent Hybrid Perovskite Nanoparticles. *ACS Applied Nano Materials*. 2019, **2**(7), 4267–4274. DOI: 10.1021/acsanm.9b00725. ISSN 2574-0970.

[149]   JANCIK PROCHAZKOVA, Anna, Yolanda SALINAS, Cigdem YUMUSAK, Markus Clark SCHARBER, Oliver BRÜGGEMANN, Martin WEITER, Niyazi Serdar SARICIFTCI, Jozef KRAJCOVIC and Alexander KOVALENKO. Controlling Quantum Confinement in Luminescent Perovskite Nanoparticles for Optoelectronic Devices by the Addition of Water. *ACS Applied Nano Materials*. 2020, **3**(2), 1242–1249. DOI: 10.1021/acsanm.9b01857. ISSN 2574-0970.

[150]   JANCIK PROCHAZKOVA, Anna, Yolanda SALINAS, Cigdem YUMUSAK, Oliver BRÜGGEMANN, Martin WEITER, Niyazi Serdar SARICIFTCI, Jozef KRAJCOVIC and Alexander KOVALENKO. Cyclic Peptide Stabilized Lead Halide Perovskite Nanoparticles. *Scientific Reports*. 2019, **9**(1). DOI: 10.1038/s41598-019-49643-7. ISSN 2045-2322.

[151] JANCIK PROCHAZKOVA, Anna, Sabrina GAIDIES, Cigdem YUMUSAK, Oliver BRÜGGEMANN, Martin WEITER, Niyazi Serdar SARICIFTCI, Markus Clark SCHARBER, Klára ČÉPE, Radek ZBOŘIL, Jozef KRAJCOVIC, Yolanda SALINAS and Alexander KOVALENKO. Peptide nucleic acid stabilized perovskite nanoparticles for nucleic acid sensing. *Materials Today Chemistry*. 2020, **17**. DOI: 10.1016/j.mtchem.2020.100272. ISSN 24685194.

[152] GONZALEZ-CARRERO, Soranyel, Raquel E. GALIAN and Julia PÉREZ-PRIETO. Maximizing the emissive properties of $CH_3NH_3PbBr_3$ perovskite nanoparticles. *Journal of Materials Chemistry A*. 2015, **3**(17), 9187–9193. DOI: 10.1039/C4TA05878J. ISSN 2050-7488.

[153] HAMILL, J. Clay, Jeffrey SCHWARTZ and Yueh-Lin LOO. Influence of Solvent Coordination on Hybrid Organic–Inorganic Perovskite Formation. *ACS Energy Letters*. 2017, **3**(1), 92–97. DOI: 10.1021/acsenergylett.7b01057. ISSN 2380-8195.

[154] YANG, Yuqian, Jihuai WU, Tongyue WU, Zhe XU, Xuping LIU, Qiyao GUO and Xin HE. An efficient solvent additive for the preparation of anion-cation-mixed hybrid and the high performance perovskite solar cells. *Journal of Colloid and Interface Science*. 2018, **531**, 602–608. DOI: 10.1016/j.jcis.2018.07.106. ISSN 00219797.

[155] HUANG, Jianbing, Shunquan TAN, Peter D. LUND and Huanping ZHOU. Impact of H_2O on organic-inorganic hybrid perovskite solar cells. *Energy & Environmental Science*. 2017, **10**(11), 2284–2311. DOI: 10.1039/c7ee01674c. ISSN 1754-5692.

[156] WU, Yongzhen, Ashraful ISLAM, Xudong YANG, Chuanjiang QIN, Jian LIU, Kun ZHANG, Wenqin PENG and Liyuan HAN. Retarding the crystallization of PbI_2 for highly reproducible planar-structured perovskite solar cells via sequential deposition. *Energy Environ. Sci.* 2014, **7**(9), 2934–2938. DOI: 10.1039/C4EE01624F. ISSN 1754-5692.

[157] VENKATESWARLU, K., A. CHANDRA BOSE and N. RAMESHIBABU. X-ray peak broadening studies of nanocrystalline hydroxyapatite by Williamson-Hall analysis. *Physica B: Condensed Matter*. 2010, **405**(20), 4256–4261. DOI: 10.1016/j.physb.2010.07.020. ISSN 09214526.

[158] SETH, Sudipta, Tasnim AHMED, Apurba DE and Anunay SAMANTA. Tackling the Defects, Stability, and Photoluminescence of $CsPbX_3$ Perovskite Nanocrystals. *ACS Energy Letters*. 2019, **4**(7), 1610–1618. DOI: 10.1021/acsenergylett.9b00849. ISSN 2380-8195.

[159]   TAN, Yeshu, Yatao ZOU, Linzhong WU, Qi HUANG, Di YANG, Min CHEN, Muyang BAN, Chen WU, Tian WU, Sai BAI, Tao SONG, Qiao ZHANG and Baoquan SUN. Highly Luminescent and Stable Perovskite Nanocrystals with Octylphosphonic Acid as a Ligand for Efficient Light-Emitting Diodes. *ACS Applied Materials & Interfaces*. 2018, **10**(4), 3784–3792. DOI: 10.1021/acsami.7b17166. ISSN 1944-8244.

[160]   PRATAP, Shambhavi, Elisabeth KELLER and Peter MÜLLER-BUSCHBAUM. Emergence of lead halide perovskite colloidal dispersions through aggregation and fragmentation: insights from the nanoscale to the mesoscale. *Nanoscale*. 2019, **11**(8), 3495–3499. DOI: 10.1039/C8NR09853K. ISSN 2040-3364.

[161]   RAN, Junhui, Ondrej O. DYCK, Xiaozheng WANG, Bin YANG, David B. GEOHEGAN and Kai XIAO. Electron-Beam-Related Studies of Halide Perovskites: Challenges and Opportunities. *Advanced Energy Materials*. 2020, 1903191. DOI: 10.1002/aenm.201903191. ISSN 1614-6832.

[162]   SICHERT, Jasmina A., Yu TONG, Niklas MUTZ, Mathias VOLLMER, Stefan FISCHER, Karolina Z. MILOWSKA, Ramon García CORTADELLA, Bert NICKEL, Carlos CARDENAS-DAW, Jacek K. STOLARCZYK, Alexander S. URBAN and Jochen FELDMANN. Quantum Size Effect in Organometal Halide Perovskite Nanoplatelets. *Nano Letters*. 2015, **15**(10), 6521–6527. DOI: 10.1021/acs.nanolett.5b02985. ISSN 1530-6984.

[163]   LEWANDOWSKA-ANDRALOJC, Anna and Bronislaw MARCINIAK. Five Major Sins in Fluorescence Spectroscopy of Light-Harvesting Hybrid Materials. *ACS Energy Letters*. 2019, **4**(8), 1898–1901. DOI: 10.1021/acsenergylett.9b01146. ISSN 2380-8195.

[164]   XIAO, Meng, Li ZHAO, Min GENG, Yanyan LI, Binghai DONG, Zuxun XU, Wenlu LI and Shimin WANG. Selection of Anti-solvent of Efficient and Stable Cesium-containing Triple Cation Planar Perovskite Solar Cells. *Nanoscale*. 2018, **10**(25), 12141–12148. DOI: 10.1039/C8NR03580F. ISSN 2040-3364.

[165]   WANG, Yafei, Shibin LI, Peng ZHANG, Detao LIU, Xiangling GU, Hojjatollah SARVARI, Zhongbiao Ye, Jiang WU, Zhiming WANG and Zhi David CHEN. Solvent Annealing of PbI$_2$ for High-Quality Crystallization of Perovskite Films for Solar Cells with Efficiency Exceeding 18%. *Nanoscale*. 2016, **8**(47), 19654–19661. DOI: 10.1039/C6NR07076K. ISSN 2040-3364.

[166]   PARVEEN, Abdulrazack, Venkatsan SUGHANYA and Samuthira NAGARAJAN. Quenching of fluorescence in C$_{60}$ fulleropyrrolidines by chloroform. *Spectrochimica Acta*

Part A: Molecular and Biomolecular Spectroscopy. 2016, **152**, 77–81. DOI: 10.1016/j.saa.2015.07.069. ISSN 13861425.

[167]   SAPERSTEIN, David. Fluorescence quenching of ultraviolet excited aromatic solutions by chloroform an several related chlorinated methanes. *The Journal of Chemical Physics.* 1975, **62**(9). DOI: 10.1063/1.430948. ISSN 00219606.

[168]   MASI, Sofia, Silvia COLELLA, Andrea LISTORTI, Vittoria ROIATI, Andrea LISCIO, Vincenzo PALERMO, Aurora RIZZO and Giuseppe GIGLI. Growing perovskite into polymers for easy-processable optoelectronic devices. *Scientific Reports.* 2015, **5**(1). DOI: 10.1038/srep07725. ISSN 2045-2322.

[169]   WANG, Qiang, Xiao-Dan LIU, Yun-Hang QIU, Kai CHEN, Li ZHOU and Qu-Quan WANG. Quantum confinement effect and exciton binding energy of layered perovskite nanoplatelets. *AIP Advances.* 2018, **8**(2). DOI: 10.1063/1.5020836. ISSN 2158-3226.

[170]   MEYERS, Robert. *Encyclopedia of Analytical Chemistry* [online]. Chichester, UK: John Wiley, 2006 [cit. 2020-05-14]. DOI: 10.1002/9780470027318. ISBN 0471976709.

[171]   ACIK, Muge, In Kee PARK, Rachel E. KORITALA, Geunsik LEE and Richard A. ROSENBERG. Oxygen-induced defects at the lead halide perovskite/graphene oxide interfaces. *Journal of Materials Chemistry A.* 2018, **6**(4), 1423–1442. DOI: 10.1039/C7TA10010H. ISSN 2050-7488.

[172]   YI, Ningbo, Shuai WANG, Zonghui DUAN, Kaiyang WANG, Qinghai SONG and Shumin XIAO. Tailoring the Performances of Lead Halide Perovskite Devices with Electron-Beam Irradiation. *Advanced Materials.* 2017, **29**(34). DOI: 10.1002/adma.201701636. ISSN 09359648.

[173]   LASHKOR, Minhaj, Frankie J. RAWSON, Jon A. PREECE and Paula M. MENDES. Switching specific biomolecular interactions on surfaces under complex biological conditions. *The Analyst.* 2014, **139**(21), 5400–5408. DOI: 10.1039/C4AN01225A. ISSN 0003-2654

[174]   WANG, Ying, Liangjun LI, Pengcheng DAI, Liting YAN, Lei CAO, Xin GU and Xuebo ZHAO. Missing-node directed synthesis of hierarchical pores on a zirconium metal–organic framework with tunable porosity and enhanced surface acidity via a microdroplet flow reaction. *Journal of Material Chemistry A.* 2017, **5**(42), 22372–22379. DOI: 10.1039/C7TA06060B. ISSN 2050-7488.

[175]   SUN, Haizhu, Zhenyu YANG, Mingyang WEI, Wei SUN, Xiyan LI, Shuyang YE, Yongbiao ZHAO, Hairen TAN, Emily L. KYNASTON, Tyler B. SCHON, Han YAN, Zheng-Hong LU, Geoffrey A. OZIN, Edward H. SARGENT and Dwight S. SEFEROS.

Chemically Addressable Perovskite Nanocrystals for Light-Emitting Applications. *Advanced Materials*. 2017, **29**(34). DOI: 10.1002/adma.201701153. ISSN 09359648.

[176]   CABANA, A. and C. SANDORFY. The infrared spectra of solid methylammonium halides. *Spectrochimica Acta*. 1962, **18**(6), 843–861. DOI: 10.1016/0371-1951(62)80089-7. ISSN 03711951.

[177]   GUO, Xin, Christopher McCLEESE, Charles KOLODZIEJ, Anna C. S. SAMIA, Yixin ZHAO and Clemens BURDA. Identification and characterization of the intermediate phase in hybrid organic-inorganic MAPbI$_3$ perovskite. *Dalton Transactions*. 2016, **45**(9), 3806–3813. DOI: 10.1039/C5DT04420K. ISSN 1477-9226.

[178]   ECK, Michael. Performance enhancement of hybrid nanocrystal/polymer bulk heterojunction solar cells: aspects of device efficiency, reproducibility and stability [online]. Freiburg, 2014 [cit. 2020-05-15]. Dostupné z: https://freidok.uni-freiburg.de/data/9808. Dizertační práce. Albert Ludwigs Universität Freiburg im Breisgau.

[179]   LI, Yong, Junwei SHI, Jianghui ZHENG, Jueming BING, Jianyu YUAN, Yongyoon CHON, Shi TANG, Meng ZHANG, Yin YAO, Cho Fai Jonathan LAU, Da Seul LEE, Chwenhaw LIAO, Martin A. GREEN, Shujuan HUANG, Wanli MA and Anita W. Y. HO-BAILLIE. Acetic Acid Assisted Crystallization Strategy for High Efficiency and Long-Term Stable Perovskite Solar Cell. *Advanced Science*. 2020, **7**(5). DOI: 10.1002/advs.201903368. ISSN 2198-3844.

[180]   ZHANG, Wei, Michael SALIBA, David T. MOORE, Sandeep K. PATHAK, Maximilian T. HÖRANTNER, Thomas STERGIOPOULOS, Samuel D. STRANKS, Giles E. EPERON, Jack A. ALEXANDER-WEBBER, Antonio ABATE, Aditya SADHANALA, Shuhua YAO, Yulin CHEN, Richard H. FRIEND, Lara A. ESTROFF, Ulrich WIESNER and Henry J. SNAITH. Ultrasmooth organic–inorganic perovskite thin-film formation and crystallization for efficient planar heterojunction solar cells. *Nature Communications*. 2015, **6**(1). DOI: 10.1038/ncomms7142. ISSN 2041-1723.

[181]   SETH, Sudipta, Tasnim AHMED and Anunay SAMANTA. Photoluminescence Flickering and Blinking of Single CsPbBr$_3$ Perovskite Nanocrystals: Revealing Explicit Carrier Recombination Dynamics. *The Journal of Physical Chemistry Letters*. 2018, **9**(24), 7007–7014. DOI: 10.1021/acs.jpclett.8b02979. ISSN 1948-7185.

[182]   GFROERER, T. H., L. P. PRIESTLEY, M. F. FAIRLEY and M. W. WANLASS. Temperature dependence of nonradiative recombination in low-band gap $In_xGa_{1-x}As/InAs_yP_{1-y}$ double heterostructures grown on InP substrates. *Journal of Applied Physics*. 2003, **94**(3), 1738–1743. DOI: 10.1063/1.1586468. ISSN 0021-8979.

[183]   LIU, Yting, Haizhou LU, Jiaxin NIU, Huotian ZHANG, Shitao LOU, Chunlei GAO, Yiqiang ZHAN, Xiaolei ZHANG, Qingyuan JIN and Lirong ZHENG. Temperature-dependent photoluminescence spectra and decay dynamics of $MAPbBr_3$ and $MAPbI_3$ thin films. *AIP Advances*. 2018, **8**(9). DOI: 10.1063/1.5042489. ISSN 2158-3226.

[184]   DAR, M. Ibrahim, Gwénolé JACOPIN, Simone MELONI, Alessandro MATTONI, Neha ARORA, Ariadni BOZIKI, Shaik M. ZAKEERUDDIN, Ursula ROTHLISBERGER and Michael GRÄTZEL. Origin of unusual bandgap shift and dual emission in organic-inorganic lead halide perovskites. *Science Advances*. 2016, **2**(10). DOI: 10.1126/sciadv.1601156. ISSN 2375-2548.

[185]   SHAO, Qing and Carol K. HALL. Binding Preferences of Amino Acids for Gold Nanoparticles: A Molecular Simulation Study. *Langmuir*. 2016, **32**(31), 7888–7896. DOI: 10.1021/acs.langmuir.6b01693. ISSN 0743-7463.

[186]   RAHIMNEJAD, Sara, Alexander KOVALENKO, Sergio Martí FORÉS, Clara ARANDA and Antonio GUERRERO. Coordination Chemistry Dictates the Structural Defects in Lead Halide Perovskites. *ChemPhysChem*. 2016, **17**(18), 2795–2798. DOI: 10.1002/cphc.201600575. ISSN 14394235.

[187]   YUFIT, D. S. and J. A. K. HOWARD. Low-melting molecular complexes of chloroform. *CrystEngComm*. 2010, **12**(3), 737–741. DOI: 10.1039/B914851E. ISSN 1466-8033.

[188]   KUROIWA, K., N. ODA and N. KIMIZUKA. Supramolecular solvatochromism. Effect of solvents on the self-assembly and charge transfer absorption characteristics of lipid-packaged, linear mixed-valence platinum complexes. *Science and Technology of Advanced Materials*. 2016, **7**(7), 629–634. DOI: 10.1016/j.stam.2006.09.011. ISSN 1468-6996.

[189]   WANG, Qun, Sicao YU, Wei QIN and Xiaohong WU. Isopropanol-assisted synthesis of highly stable $MAPbBr_3$/p-g-C_3N_4 intergrowth composite photocatalysts and their interfacial charge carrier dynamics. *Nanoscale Advances*. 2020, **2**(1), 274–285. DOI: 10.1039/C9NA00634F. ISSN 2516-0230.

[190]   EBRAHIMINEZHAD, Alireza, Younes GHASEMI, Sara RASOUL-AMINI, Jaleh BARAR and Soodabeh DAVARAN. Impact of Amino-Acid Coating on the Synthesis and Characteristics of Iron-Oxide Nanoparticles (IONs). *Bulletin of the Korean Chemical Society*. 2012, **33**(12), 3957–3962. DOI: 10.5012/bkcs.2012.33.12.3957. ISSN 0253-2964.

[191] RAYA, Anthony Samy Sahaya and Susai RAJENDRAN. Inhibition of corrosion of carbon steel in well water *by arginine-Zn^{2+} system. Journal of Electrochemical Science and Engineering*. 2012, **2**, 91–104. DOI: 10.5599/jese.2012.0012. ISSN 18479286.

[192] DURU, İlayda and Duygu EGE. Self-Assembly of L-Arginine on Electrophoretically Deposited Hydroxyapatite Coatings. *ChemistrySelect*. 2018, **3**(31), 9041–9045. DOI: 10.1002/slct.201801913. ISSN 23656549.

[193] LI, Wan-Chao and Sang-Wha LEE. The characteristics of lysine-mediated self-assembly of gold nanoparticles on the ITO glass. *Current Applied Physics*. 2012, **12**(5), 1361–1365. DOI: 10.1016/j.cap.2012.03.027. ISSN 15671739.

[194] LIAO Wan-Ci, Bernard Haochih LIU and Ching-Chich LEU. Nanoscale mapping of humid degradation-induced local mechanical property variation in $CH_3NH_3PbI_3$ polycrystalline film by scanning probe microscopy. *Applied Surface Science*. 2020, 507. DOI: 10.1016/j.apsusc.2019.145078. ISSN 01694332.

[195] JONG, Un-Gi, Chol-Jun YU, Gum-Chol RI, Andrew P. MCMAHON, Nicholas M. HARRISON, Piers R. F. BARNES and Aron WALSH. Influence of water intercalation and hydration on chemical decomposition and ion transport in methylammonium lead halide perovskites. *Journal of Materials Chemistry A*. 2018, **6**(3), 1067–1074. DOI: 10.1039/C7TA09112E. ISSN 2050-7488.

[196] LIU, Dianyi, Christopher J. TRAVERSE, Pei CHEN, Mark ELINSKI, Chenchen YANG, Lili WANG, Margaret YOUNG and Richard R. LUNT. Aqueous-Containing Precursor Solutions for Efficient Perovskite Solar Cells. *Advanced Science*. 2018, **5**(1). DOI: 10.1002/advs.201700484. ISSN 21983844.

[197] ADHIKARI, Nirmal, Ashish DUBEY, Eman A. GAML, Bjorn VAAGENSMITH, Khan Mamun REZA, Sally Adel Abdelsalam MABROUK, Shaopeng GU, Jiantao ZAI, Xuefeng QIAN and Qiquan QIAO. Crystallization of a perovskite film for higher performance solar cells by controlling water concentration in methyl ammonium iodide precursor solution. *Nanoscale*. 2016, **8**(5), 2693–2703. DOI: 10.1039/C5NR06687E. ISSN 2040-3364.

[198] WU, Chun-Guey, Chien-Hung CHIANG, Zong-Liang TSENG, Md. K. NAZEERUDDIN, Anders HAGFELDT and Michael GRÄTZEL. High efficiency stable inverted perovskite solar cells without current hysteresis. *Energy & Environmental Science*. 2015, **8**(9), 2725–2733. DOI: 10.1039/C5EE00645G. ISSN 1754-5692.

[199] NEEDHAM, Thomas E. *The Solubility of Amino Acids in Various Solvent Systems*. Kingston, USA, 1970. Ph.D. Dissertation. University of Rhode Island.

[200]   HU, Dawei, Jianmin CHEN, Xingnan YE, Ling LI and Xin YANG. Hygroscopicity and evaporation of ammonium chloride and ammonium nitrate: Relative humidity and size effects on the growth factor. *Atmospheric Environment*. 2011, **45**(14), 2349–2355. DOI: 10.1016/j.atmosenv.2011.02.024. ISSN 13522310.

[201]   NIEDZIALKOWSKI, P., T. OSSOWSKI, P. ZIEBA, A. CIROCKA, P. ROCHOWSKI, S. J. POGORZELSKI, J. RYL, M. SOBASZEK and R. BOGDANOWICZ. Poly-L-lysine-modified boron-doped diamond electrodes for the amperometric detection of nucleic acid bases. *Journal of Electroanalytical Chemistry*. 2015, **756**, 84–93. DOI: 10.1016/j.jelechem.2015.08.006. ISSN 15726657.

[202]   SARIKAYA, Mehmet, Candan TAMERLER, Alex K. -Y. JEN, Klaus SCHULTEN and François BANEYX. Molecular biomimetics: nanotechnology through biology. *Nature Materials*. 2003, **2**(9), 577–585. DOI: 10.1038/nmat964. ISSN 1476-1122.

[203]   TORCULAS, Maria, Jethro MEDINA, Wei XUE and Xiao HU. Protein-Based Bioelectronics. *ACS Biomaterials Science & Engineering*. 2016, **2**(8), 1211–1223. DOI: 10.1021/acsbiomaterials.6b00119. ISSN 2373-9878.

[204]   LAKSHMANAN, Anupama, Shuguang ZHANG and Charlotte A.E. HAUSER. Short self-assembling peptides as building blocks for modern nanodevices. *Trends in Biotechnology*. 2012, 30(3), 155–165. DOI: 10.1016/j.tibtech.2011.11.001. ISSN 01677799.

[205]   SPICER, Christopher D., Coline JUMEAUX, Bakul GUPTA and Molly M. STEVENS. Peptide and protein nanoparticle conjugates: versatile platforms for biomedical applications. *Chemical Society Reviews*. 2018, **47**(10), 3574–3620. DOI: 10.1039/C7CS00877E. ISSN 0306-0012.

[206]   WANG, Wei and Neal W. WOODBURY. Selective protein–peptide interactions at surfaces. *Acta Biomaterialia*. 2014, **10**(2), 761–768. DOI: 10.1016/j.actbio.2013.10.025. ISSN 17427061.

[207]   AMDURSKY, Nadav, Michel MOLOTSKII, Ehud GAZIT and Gil ROSENMAN. Elementary Building Blocks of Self-Assembled Peptide Nanotubes. *Journal of the American Chemical Society*. 2010, **132**(44), 15632–15636. DOI: 10.1021/ja104373e. ISSN 0002-7863.

[208]   HERSEL, Ulrich, Claudia DAHMEN and Horst KESSLER. RGD modified polymers: biomaterials for stimulated cell adhesion and beyond. *Biomaterials*. 2003, **24**(24), 4385–4415. DOI: 10.1016/S0142-9612(03)00343-0. ISSN 01429612.

[209]   HE, Hua, Xing SUN, Xiaojuan WANG, Yawei SUN, Hai XU and Jian R. LU. Cyclic arginyl–glycyl–aspartic acid (RGD) peptide-induced synthesis of uniform and stable one-dimensional CdTe nanostructures in aqueous solution. *RSC Advances*. 2014, **4**(23). DOI: 10.1039/c3ra47253a. ISSN 2046-2069.

[210]   NIELSEN, Peter E., Michael EGHOLM, Rolf H. BERG and Ole BUCHARDT. Sequence-selective recognition of DNA by strand displacement with a thymine-substituted polyamide. *Science*. 1991, **254**(5037), 1497–1500. DOI: 10.1126/science.1962210. ISSN 0036-8075.

[211]   EGHOLM, Michael, Ole BUCHARDT, Peter E. NIELSEN and Rolf H. BERG. Peptide nucleic acids (PNA). Oligonucleotide analogs with an achiral peptide backbone. *Journal of the American Chemical Society*. 1992, **114**(5), 1895–1897. DOI: 10.1021/ja00031a062. ISSN 0002-7863.

[212]   EGHOLM, Michael, Ole BUCHARDT, Leif CHRISTENSEN, Carsten BEHRENS, Susan M. FREIER, David A. DRIVER, Rolf H. BERG, Seog K. KIM, Bengt NORDEN and Peter E. NIELSEN. PNA hybridizes to complementary oligonucleotides obeying the Watson–Crick hydrogen-bonding rules. *Nature*. 1993, **365**(6446), 566–568. DOI: 10.1038/365566a0. ISSN 0028-0836.

[213]   WIERZBINSKI, Emil, Arnie de LEON, Kathryn L. DAVIS, Silvia BEZER, Matthäus A. WOLAK, Matthew J. KOFKE, Rudy SCHLAF, Catalina ACHIM and David H. WALDECK. Charge Transfer through Modified Peptide Nucleic Acids. *Langmuir*. 2011, **28**(4), 1971–1981. DOI: 10.1021/la204445u. ISSN 0743-7463.

[214]   PAUL, Amit, Richard M. WATSON, Paul LUND, Yangjun XING, Kathleen BURKE, Yufan HE, Eric BORGUET, Catalina ACHIM and David H. WALDECK. Charge Transfer through Single-Stranded Peptide Nucleic Acid Composed of Thymine Nucleotides. *The Journal of Physical Chemistry C*. 2008, **112**(18), 7233–7240. DOI: 10.1021/jp711764q. ISSN 1932-7447.

[215]   HATCHER, Elizabeth, Alexander BALAEFF, Shahar KEINAN, Ravindra VENKATRAMANI and David N. BERATAN. PNA versus DNA: Effects of Structural Fluctuations on Electronic Structure and Hole-Transport Mechanisms. *Journal of the American Chemical Society*. 2008, **130**(35), 11752–11761. DOI: 10.1021/ja802541e. ISSN 0002-7863.

[216]   WOO, Hee Chul, Jin Woo CHOI, Jisoo SHIN, Sang-Hyun CHIN, Myung Hyun ANN and Chang-Lyoul LEE. Temperature-Dependent Photoluminescence of $CH_3NH_3PbBr_3$

Perovskite Quantum Dots and Bulk Counterparts. *The Journal of Physical Chemistry Letters*. 2018, **9**(14), 4066–4074. DOI: 10.1021/acs.jpclett.8b01593. ISSN 1948-7185.

[217] VENKATRAMANI, Ravindra, Shahar KEINAN, Alexander BALAEFF and David N. BERATAN. Nucleic acid charge transfer: Black, white and gray. *Coordination Chemistry Reviews*. 2011, **255**(7-8), 635–648. DOI: 10.1016/j.ccr.2010.12.010. ISSN 00108545.

[218] LIU, Juewen, Zehui CAO and Yi LU. Functional Nucleic Acid Sensors. *Chemical Reviews*. 2009, **109**(5), 1948–1998. DOI: 10.1021/cr030183i. ISSN 0009-2665.

[219] HERZ, Laura M. Charge-Carrier Mobilities in Metal Halide Perovskites: Fundamental Mechanisms and Limits. *ACS Energy Letters*. 2017, **2**(7), 1539–1548. DOI: 10.1021/acsenergylett.7b00276. ISSN 2380-8195.

[220] JANCIK PROCHAZKOVA, Anna, Felix MAYR, Katarina GUGUJONOVIC, Bekele HAILEGNAW, Jozef KRAJCOVIC, Yolanda SALINAS, Oliver BRÜGGEMANN, Niyazi Serdar SARICIFTCI and Markus C. SCHARBER. Anti-Stokes Photoluminescence Study on a Methylammonium Lead Bromide Nanoparticle Film. *Nanoscale*, accepted.

10 List of abbreviations and symbols

10.1 Abbreviations

AcA	Acetic Acid
ACN	Acetonitrile
AdA	Adamantane-1-carboxylic Acid
AdNH$_2$	Adamantyl-1-amine
AFM	Atomic Force Microscopy
Arg	L-Arginine
ATR	Attenuated Total Reflectance
boc-Arg	N_α-(*tert*-Butoxycarbonyl)-L-Arginine
boc-Lys	N_α-(*tert*-Butoxycarbonyl)-L-Lysine
CB	Conduction Band
cyclo(RGDFK)	Cyclic (RGDFK) pentapeptide
DLS	Dynamic Light Scattering
DMF	*N,N*-Dimethylformamide
DMSO	Dimethyl sulfoxide
DNA	Deoxyribonucleic Acid
EDS	Energy Dispersive X-ray Spectroscopy
FA	Formamidinium
FFT	Fast Fourier Transform
FTIR	Fourier-Transform Infrared (spectroscopy)
FWHM	Full Width at Half Maximum
GBL	γ-Butyrolactone
HeA	Hexanoic Acid
HRTEM	High Resolution Transmission Electron Microscopy
ITC	Inverse Temperature Crystallization Method
LED	Light Emitting Diode
Lys	L-Lysine
MA	Methylammonium
OctA	n-Octanoic Acid
OLED	Organic Light Emitting Diode
OleicA	Oleic Acid
PCE	Power Conversion Efficiency
PL	Photoluminescence (spectroscopy)
PLQY	Photoluminescence Quantum Yield
PropA	Propanoic Acid
PNA	Peptide Nucleic Acid
PNA-M	Monomer of Peptide Nucleic Acid

PNA-T	Trimer of Peptide Nucleic Acid
PNP	Perovskite Nanoparticles
QLED	Quantum Dot Light Emitting Diodes
RMS	Root Mean Square
RNA	Ribonucleic Acid
Rpm	Rotates per Minute
Rq	Roughness
STM	Scanning Tuneling Microscope
TEM	Transmission Electron Microscopy
TriflacA	Trifluoroacetic Acid
UV	Ultraviolet
VB	Valence Band
XPS	X-ray Photoelectron Spectroscopy
XRD	X-ray Diffraction

10.2 Symbols

α	absorption coefficient
η	absolute photoluminescence quantum yield (PLQY)
ν	photon frequency
$1/n$	constant denoting the nature of the transition above photoexcitation
a_0	Bohr radius
A	constant of proportionality
e^-	electron
E	energy
E_B	integral of the emission spectrum
E_F	Fermi energy
E_g	energy of bandgap
E_{kin}	kinetic energy
h^+	hole
h	Plank´s constant
$m*$	effective mass
S_A and S_B	integrals of the emission spectra in the excitation area of the sample and pure solvent
t	tolerance factor

144

11 Curriculum Vitae

Personal information

Name	Anna Jančík Procházková
Address	Kozlany 76, CZ 683 41 Bohdalice
Phone	+420 724 008 028
e-mail	xcprochazkovaa@fch.vutbr.cz

Education

2017 – presence	Doctoral Study Programme in the field of Chemistry, Technology and Properties of Materials at Brno University of Technology, Faculty of Chemistry Dissertation thesis: Synthesis and study of nano-structured perovskites for application in organic electronics
2015 – 2017	Master´s Degree Programme in the field Consumer Chemistry at Brno University of Technology, Faculty of Chemistry Master thesis: Fluorescence spectroscopy in the research of aminoclays
2011 – 2015	Bachelor´s Degree Programme in the field Consumer Chemistry at Brno University of Technology, Faculty of Chemistry Bachelor thesis: Interactions of aminoclays with natural polyelectrolytes

Internship

07/2018–12/2019	Group of o. Univ. Prof. Mag. Dr. DDr. h.c. Niyazi Serdar Sariciftci in Linz Institute for Organic Solar Cells (LIOS), Physical Chemistry, Johannes Kepler University Linz, Altenbergerstraße 69, 4040 Linz, Austria

Pedagogical activity

2017	Laboratory Classes in Organic Chemistry

International conferences

Poster presentation

2019: 6th International Winterschool on Bioelectronics, BioEl. Austria, Kirchberg in Tirol.

2019: 14th International Symposium on Functional pi-Electron Systems. Germany, Berlin.

Oral presentation

2019: 11th International Conference on Nanomaterials, Nanocon. Czech Republic, Brno.

Publications

MOURYCOVÁ, Jana, K. K. R. DATTA, Anna PROCHÁZKOVÁ, Michaela PLOTĚNÁ, Vojtěch ENEV, Jiří SMILEK, Jiří MÁSÍLKO and Miloslav PEKAŘ. Facile synthesis and rheological characterization of nanocomposite hyaluronan-organoclay hydrogels. *International Journal of Biological Macromolecules.* 2018, **111**, 680–684. DOI: 10.1016/j.ijbiomac.2018.01.068. ISSN 01418130.

JANCIK PROCHAZKOVA, Anna, Stepan DEMCHYSHYN, Cigdem YUMUSAK, Jiří MÁSILKO, Oliver BRÜGGEMANN, Martin WEITER, Martin KALTENBRUNNER, Niyazi Serdar SARICIFTCI, Jozef KRAJCOVIC, Yolanda SALINAS and Alexander KOVALENKO. Proteinogenic Amino Acid Assisted Preparation of Highly Luminescent Hybrid Perovskite Nanoparticles. *ACS Applied Nano Materials.* 2019, **2**(7), 4267–4274. DOI: 10.1021/acsanm.9b00725. ISSN 2574-0970.

JANCIK PROCHAZKOVA, Anna, Yolanda SALINAS, Cigdem YUMUSAK, Oliver BRÜGGEMANN, Martin WEITER, Niyazi Serdar SARICIFTCI, Jozef KRAJCOVIC and Alexander KOVALENKO. Cyclic Peptide Stabilized Lead Halide Perovskite Nanoparticles. *Scientific Reports.* 2019, **9**(1). DOI: 10.1038/s41598-019-49643-7. ISSN 2045-2322.

YUMUSAK, Cigdem, Anna JANCIK PROCHAZKOVA, Dogukan Hazar APAYDIN, Hathaichanok SEELAJAROEN, Niyazi Serdar SARICIFTCI, Martin WEITER, Jozef KRAJCOVIC, Yong QIN, Wei ZHANG, Jixun ZHAN and Alexander KOVALENKO. Indigoidine – Biosynthesized organic semiconductor. *Dyes and Pigments.* 2019, **171**. DOI: 10.1016/j.dyepig.2019.107768. ISSN 01437208.

JANCIK PROCHAZKOVA, Anna, Yolanda SALINAS, Cigdem YUMUSAK, Markus Clark SCHARBER, Oliver BRÜGGEMANN, Martin WEITER, Niyazi Serdar SARICIFTCI, Jozef KRAJCOVIC and Alexander KOVALENKO. Controlling Quantum Confinement in Luminescent Perovskite Nanoparticles for Optoelectronic Devices by the Addition of Water. *ACS Applied Nano Materials.* 2020, **3**(2), 1242–1249. DOI: 10.1021/acsanm.9b01857. ISSN 2574-0970.

JANCIK, Jan, Anna JANCIK PROCHAZKOVA, Markus Clark SCHARBER, Alexander KOVALENKO, Jiří MÁSILKO, Niyazi Serdar SARICIFTCI, Martin WEITER and Jozef KRAJCOVIC. Microwave-Assisted Preparation of Organo-Lead Halide Perovskite Single Crystals. *Crystal Growth & Design.* 2020, **20**(3), 1388–1393. DOI: 10.1021/acs.cgd.9b01670. ISSN 1528-7483.

JANCIK PROCHAZKOVA, Anna, Sabrina GAIDIES, Cigdem YUMUSAK, Oliver BRÜGGEMANN, Martin WEITER, Niyazi Serdar SARICIFTCI, Markus Clark SCHARBER, Klára ČÉPE, Radek ZBOŘIL, Jozef KRAJCOVIC, Yolanda SALINAS and Alexander KOVALENKO. Peptide nucleic acid stabilized perovskite nanoparticles for nucleic acid sensing. *Materials Today Chemistry*. 2020, **17**. DOI: 10.1016/j.mtchem.2020.100272. ISSN 24685194.

JANCIK PROCHAZKOVA, Anna, Felix MAYR, Katarina GUGUJONOVIC, Bekele HAILEGNAW, Jozef KRAJCOVIC, Yolanda SALINAS, Oliver BRÜGGEMANN, Niyazi Serdar SARICIFTCI and Markus C. SCHARBER. Anti-Stokes Photoluminescence Study on a Methylammonium Lead Bromide Nanoparticle Film. *Nanoscale*, accepted.

JANCIK PROCHAZKOVA, Anna*, Markus Clark SCHARBER, Cigdem YUMUSAK, Ján JANČÍK, Jiří MÁSILKO, Oliver BRÜGGEMANN, Martin WEITER, Niyazi Serdar SARICIFTCI, Jozef KRAJCOVIC, Yolanda SALINAS and Alexander KOVALENKO. Synthesis conditions influencing formation of MAPbBr$_3$ perovskite nanoparticles prepared by the ligand-assisted precipitation method. *Scientific Reports*. Under revision.

*corresponding author